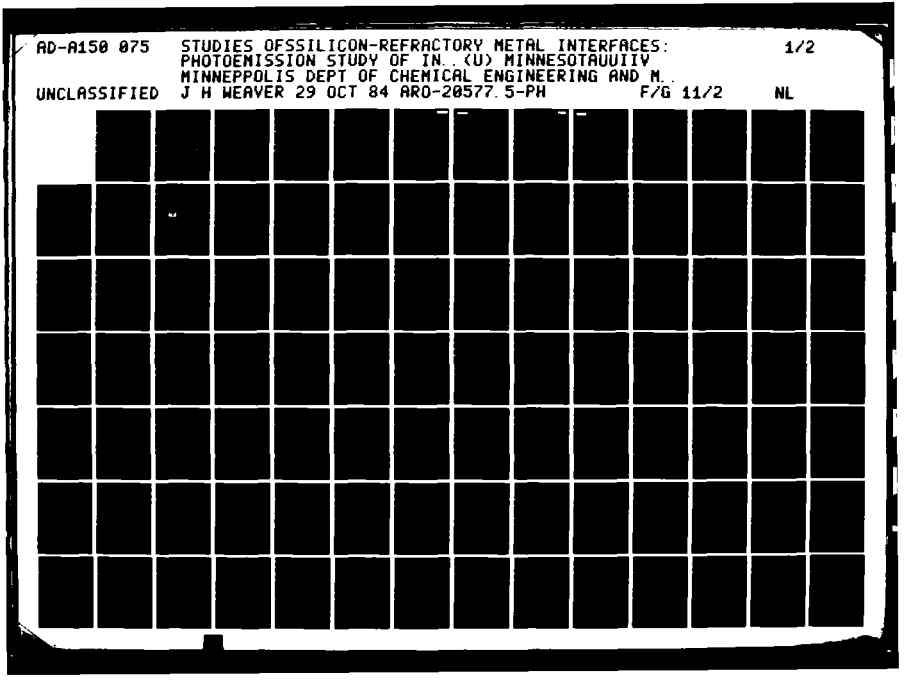
AD-A150 075 STUDIES OFSSILICON-REFRACTORY METAL INTERFACES: 1/2
PHOTOEMISSION STUDY OF IN..(U) MINNESOTAUUIIY
MINNEPPOLIS DEPT OF CHEMICAL ENGINEERING AND M..
UNCLASSIFIED J H WEAVER 29 OCT 84 ARO-20577.5-PH F/G 11/2 NL

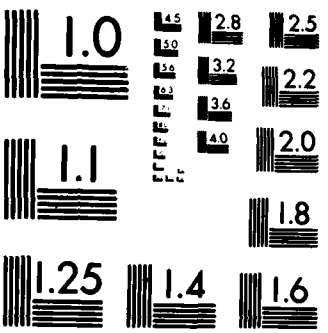

MICROCOPY RESOLUTION TEST CHART
NATIONAL BUREAU OF STANDARDS-1963-A

UNCLASSIFIED
SECURITY CLASSIFICATION OF THIS PAGE (When Data Entered)

MASTER COPY - FOR REPRODUCTION PURPOSES

REPORT DOCUMENTATION PAGE

READ INSTRUCTIONS BEFORE COMPLETING FORM

1. REPORT NUMBER: ARO 20577.5-PH
2. GOVT ACCESSION NO.: N/A
3. RECIPIENT'S CATALOG NUMBER: N/A

TITLE (and Subtitle): Studies of Silicon-Refractory Metal Interfaces: Photoemission Study of Interface Formation and Compound Nucleation

5. TYPE OF REPORT & PERIOD COVERED: Final Report 15 April 1983 - 30 Sept 1984
6. PERFORMING ORG. REPORT NUMBER:

AUTHOR(s): J.H. Weaver

8. CONTRACT OR GRANT NUMBER(s): ARO-DAAG29-83-K-0061

PERFORMING ORGANIZATION NAME AND ADDRESS: Dept. Chemical Engineering and Materials Science
151 Amundson Hall, University of Minnesota,
Minneapolis, MN 55455

10. PROGRAM ELEMENT, PROJECT, TASK AREA & WORK UNIT NUMBERS:

CONTROLLING OFFICE NAME AND ADDRESS: U. S. Army Research Office
Post Office Box 12211
Research Triangle Park, NC 27709

12. REPORT DATE: 10-29-84
13. NUMBER OF PAGES: 98 (3 of report)

14. MONITORING AGENCY NAME & ADDRESS (if different from Controlling Office):

15. SECURITY CLASS. (of this report): Unclassified
15a. DECLASSIFICATION/DOWNGRADING SCHEDULE:

16. DISTRIBUTION STATEMENT (of this Report)

Approved for public release; distribution unlimited.

17. DISTRIBUTION STATEMENT (of the abstract entered in Block 20, if different from Report)

NA

18. SUPPLEMENTARY NOTES

The view, opinions, and/or findings contained in this report are those of the author(s) and should not be construed as an official Department of the Army position, policy, or decision, unless so designated by other documentation.

19. KEY WORDS (Continue on reverse side if necessary and identify by block number)

Refractory metal silicides; interfaces; reactions at surfaces; silicon contacts.

20. ABSTRACT (Continue on reverse side if necessary and identify by block number)

Detailed investigations of representative metal/silicon interfaces were conducted using synchrotron radiation photoemission. Modeling of the resulting interfaces were complemented by studies of bulk silicides. Theoretical investigations of band formation were done collaboratively.

DD FORM 1 JAN 73 1473 EDITION OF 1 NOV 65 IS OBSOLETE

UNCLASSIFIED
SECURITY CLASSIFICATION OF THIS PAGE (When Data Entered)

Final Report ARO DAAG29-83-K-0061

ARO Proposal Number P-20577-PH

PERIOD COVERED: 15 April 1983 - 30 September 1984

TITLE: Studies of Silicon-Refractory Metal Interfaces: Photoemission Study of Interface Formation and Compound Nucleation

INSTITUTION: University of Minnesota

AUTHOR: John H. Weaver

BOOK CHAPTER IN PREPARATION:

- J.H. Weaver, "Synchrotron Radiation Photoemission Studies of Metal/Semiconductor Interfaces," Chapter 2 in Analysis and Characterization of Thin Films, ed. K.N. Tu and R. Rosenberg (Treatise on Materials Science and Technology) Vol. 28 (Academic Press) to be shared with ARO29-84-K-0169.

LIST OF PAPERS SUBMITTED AND PUBLISHED:

- A. Franciosi, J.H. Weaver, and D.G. O'Neill, "Interface Catalytic Effect: Cr at the Si(111)-Cu Interface," Phys. Rev. B - Rapid Commun. 28, 4889-4892 (1983).
- A. Franciosi, J.H. Weaver, D.G. O'Neill, F.A. Schmidt, O. Bisi, and C. Calandra, "Electronic Structure of Cr Silicides and Si-Cr Interface Reactions," Phys. Rev. B 28, 7000-7008 (1983).
- J.H. Weaver, A. Franciosi, and V.L. Moruzzi, "Bonding in Metal Disilicides $CaSi_2$ through $NiSi_2$: Experiment and Theory," Phys. Rev. B 29, 3293-3302 (1984).
- M. Grioni, J. Joyce, S.A. Chambers, D.G. O'Neill, M. del Giùdice, and J.H. Weaver, "Cluster-Induced Reactions at a Metal-Semiconductor Interface: Ce/Si(111)," Phys. Ref. Lett. (submitted).
- S.A. Chambers, T.R. Greenlee, G.A. Howell, and J.H. Weaver, "Quantitative Interdiffusion Studies of Noble Metal/Si(111)-7x7 Interfaces by Angle-Resolved Auger Electron Emission," J. Vac. Sci. Technol. (submitted).
- M. Grioni, J. Joyce, M. del Giudice, D.G. O'Neill, and J.H. Weaver, "Modeling a Heterogeneous Metal/Semiconductor Interface: Ce on Si(111)," Phys. Rev. B - Rapid Commun. (submitted).
- S.A. Chambers, T.R. Greenlee, G.A. Howell, and J.H. Weaver, "Characterization of Intermixing at Metal/Semiconductor Interfaces by Angle-Resolved Auger Electron Emission: Cu/Si(111)-7x7," Phys. Rev. B (submitted).

INVITED AND CONTRIBUTED PAPERS AND SEMINARS:

Invited seminars at Workshop on New Directions in Photoabsorption in Asilomar, MEIS Workshop on New Frontiers in Semiconductor Materials in Minneapolis, and Depth Committee, AIME/ASM, in Detroit.

Papers at International Conference on the Physics of Semiconductors, GM Research Laboratories, SRC Users Group Meeting, Ames Lab Physics Department Colloquium, NSF Site Visit - University of Wisconsin SRC, and Honeywell Corporate Technology Center.

Final Report ARO DAAG29-83-K-0061 (cont'd)

PERSONNEL: J.H. Weaver - Principal Investigator
A. Franciosi - Postdoctoral Associate through 30 August 1983
M. Grioni - Postdoctoral Associate 1 June 1983 - 30 September 1984
J. Joyce - PhD Student

BRIEF OUTLINE OF RESEARCH FINDINGS:

This report for DAAG29-83-K-0061 supplements K-0140 which covered the first twenty-one months of ARO support for our Studies of Silicon-Refractory Metal Interfaces. The emphasis here is on the final 15 months of that program. It was funded under two distinct grants because of the transfer of the PI from the University of Wisconsin to the University of Minnesota.

~~The~~ Our overall goal in this project was to examine the electronic and morphological interactions which occur at interfaces involving Si and metal overlayers. During the course of this project, we examined overlayers of Cr, Ti, Sm, Au, Ca, Ce, and Cu using photoelectron spectroscopy, Auger spectroscopy and LEED. A new technique involving angle-resolved Auger profiling was developed to determine the atomic density profile for interfaces, as discussed in the enclosed papers. Its utility was demonstrated through studies of Cu/Si, Au/Si, and Ce/Si. Exhaustive use of synchrotron radiation photoemission has lead to a detailed understanding of the electronic bonding of silicides and metal/silicon interfaces. Collaborative studies with theorists gave rise to modeling of interfaces and calculation of electronic energy states for ordered silicides. Originator

MAJOR BREAKTHROUGHS INCLUDE:

A systematic evaluation of bonding in silicides, showing how the metal-d/silicon-p bonds will change as a function of transition metal variation. This work built on the work by others for the Pd and Ni silicides and created a broader-based picture. Experimental studies of bulk silicides and theoretical and band structure calculations made this panoramic view possible.

Characterization of the onset of reaction on silicon surfaces, showing that the details vary significantly with the overlayer character but, at the same time, that all of the transition metals induce reactive disruption of the surface. For Cr/Si, we showed that the onset of reaction was delayed until a critical coverage was reached, corresponding to patch formation and subsequent disruption. For Sm/Si and Ca/Si, the reaction was triggered at the very lowest coverages. For Ce/Si, an even more complicated morphology was observed and modeled. At low coverage it was found that clusters formed but that for coverages approaching 0.6 monolayers the clusters became unstable and provided the energy necessary to disrupt the surface. Such an energy source has not been demonstrated for Si-based surfaces. The resulting interface was then highly heterogeneous. To model it, we refined a method of determining the coverage dependence of the three Si species which were observed to form, corresponding to substrate, reacted, and floating Si.

Extensive modeling of interface development has been undertaken, using high resolution photoemission. With this technique, we are now able to fingerprint the species which form and identify the chemical profile of the interface. This work is then supplemented by the angle-resolved Auger studies which give the atomic profile of the interface. Inportant information regarding in- and out-diffusion of metal and Si, the width of the interface, the dynamics of the interface, and the reactivity of the interface can then be obtained.

Final Report ARO DAAG29-83-K-0061 (cont'd)

MAJOR BREAKTHROUGHS (cont'd):

The work accomplished under the first three years of the ARO program set the stage for a second program which will seek to understand more complex systems, including reactions of metal overlayers on silicides, silicon overlayers on metal surfaces, and the effect of thin native oxides.

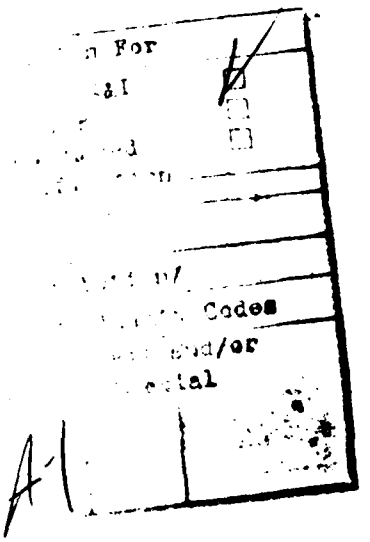

PHYSICAL REVIEW B VOLUME 28, NUMBER 8 15 OCTOBER 1983

Interface catalytic effect: Cr at the Si(111)-Au interface

A. Franciosi and J. H. Weaver
Department of Chemical Engineering and Materials Science, University of Minnesota, Minneapolis, Minnesota 55455

D. G. O'Neill
Synchrotron Radiation Center, University of Wisconsin—Madison, Stoughton, Wisconsin 53589

(Received 19 July 1983)

Synchrotron radiation photoemission studies of the effect of Cr interlayers on Si(111)-Au interface reaction show that Cr concentrations below 1×10^{15} atoms/cm^2 retard Si-Au intermixing, concentrations between 1 and 7.5×10^{15} atoms/cm^2 promote Si-Au intermixing, and concentrations in excess of 8×10^{15} atoms/cm^2 sharply reduce intermixing. These variations are shown to depend on the three formation stages of the Si-Cr junction. Cr itself is shown only to be indirectly involved in the Si-Au reaction and Si is to be the only moving species.

The driving forces responsible for atomic interdiffusion at Si-metal interfaces have been the subject of intense discussion.[1–9] To understand this atomic interdiffusion, we must identify the parameters that control interdiffusion kinetics and the junction profile, and we must determine the relationships that exist between these parameters and the chemical activity of the species involved in the interface formation process.[2–9]

In order to better understand interdiffusion, we performed an investigation of the effect of Cr interlayers on the atomic interdiffusion of Si and Au at the Si(111)-(2×1)-Au interface, with special emphasis on the chemical aspects of interdiffusion.

In this paper, we show that for Cr coverages from 2 to 9 Å the interlayer *promotes* the Si-Au intermixing, while the interdiffusion is *reduced* for Cr coverages above 9 Å (10 monolayers) or for coverages less than one monolayer. This strikingly nonmonotonic behavior rules out simple "diffusion barrier" effects and is related, instead, to the three stages of Si-Cr reaction. Each stage corresponds to a different morphology or microscopic arrangement of the Si atoms at the surface and, hence, a different energy content of the Si-Si bonds.

Our results show that the interlayer Cr atoms do not appear directly involved int the Si-Au reaction. Instead, since the Cr interlayer affects the formation of the Si-Au junction and its concentration modulates the Si-Au reaction, it seems natural to define the role of the Cr atoms as that of an "interface catalyst" for the Si-Au reaction.

The Si-Cr-Au system was chosen because the Si-Cr and the Si-Au interfaces are well characterized[10–13] and neither gives rise to island formation at room temperature. The relative surface concentration of the different species and the evolution of the chemical bonding was followed systematically through synchrotron photoemission from valence and core electronic states, both as a function of Au coverage and Cr interlayer thickness. The experiments were performed at the University of Wisconsin Synchrotron Radiation Center with a "Grasshopper" grazing-incidence monochromator for $40\leq h\nu\leq140$ eV. The photoelectrons were analyzed by a double-pass cylindrical mirror energy analyzer, and the overall resolution (monochromator + analyzer) was 0.3–0.5 eV. Cr and Au were evaporated *in situ* from W coils onto cleaved *n*-type Si crystals (P-doped, 10^{15} cm^{-3}) and the overlayer thickness was measured by a quartz-crystal monitor ($\theta_{Cr}=1$ Å $=1.1$ monolayers; $\theta_{Au}=1$ Å $=0.8$ monolayers; 1 monolayer $=7.6\times10^{14}$ atoms/cm^2). Cr depositions of 0.5–15 Å were made immediately before a series of Au depositions (maximum Au coverage of 50–70 Å for each Cr interlayer thickness). All experiments were performed at pressures of 5×10^{-11} Torr ($\leq6\times10^{-10}$ Torr during evaporation) and at room temperature.

In Fig. 1 we show representative photoelectron energy distribution curves (EDC's) for the valence band of the Si-Cr-Au interface at a fixed Au coverage of 20 Å as a function of Cr interlayer thickness.[14] The topmost spectrum corresponds to Si(111)-Au without Cr, and the bottom-most shows the valence bands for a 20-Å Au film on an inert substrate.[15] The differences between these two, which reveal the formation of the Si-Au interface, have been explained as modifications of Au 5*d*-derived density of states features caused by Si atoms in the Au matrix, mainly through the change of the *d*-*d* overlap.[12,14,16,17] Taking such differences[17] as a fingerprint of Si-Au reaction, the systematics in Fig. 1 show that a Si-Au reaction can occur in the presence of a Cr interlayer, but that the intermixing is sharply reduced when the interlayer thickness increases above 9 Å.

The presence of Si atoms in the Au matrix is clearly indicated by the topmost spectra of Fig. 1, but the valence-band spectra show no evidence of Cr at the surface. To determine whether Cr intermixes with the Au overlayer, we measured the integrated Cr derived 3*p* core emission as a function of Au coverage for two different Cr interlayer thicknesses, as shown at the top of Fig. 2. These results show an exponential attenuation of the Cr emission. Comparison with a simple exponential attenuation calculated with an escape depth of 5 Å (dashed line) indicates Si outdiffusion through the interlayer into the Au layer. This Si outdiffusion is quantitatively more important for an interlayer thickness of 2 Å than for an interlayer thickness of 8 Å. There is no evidence of Cr outdiffusion into the Au film.

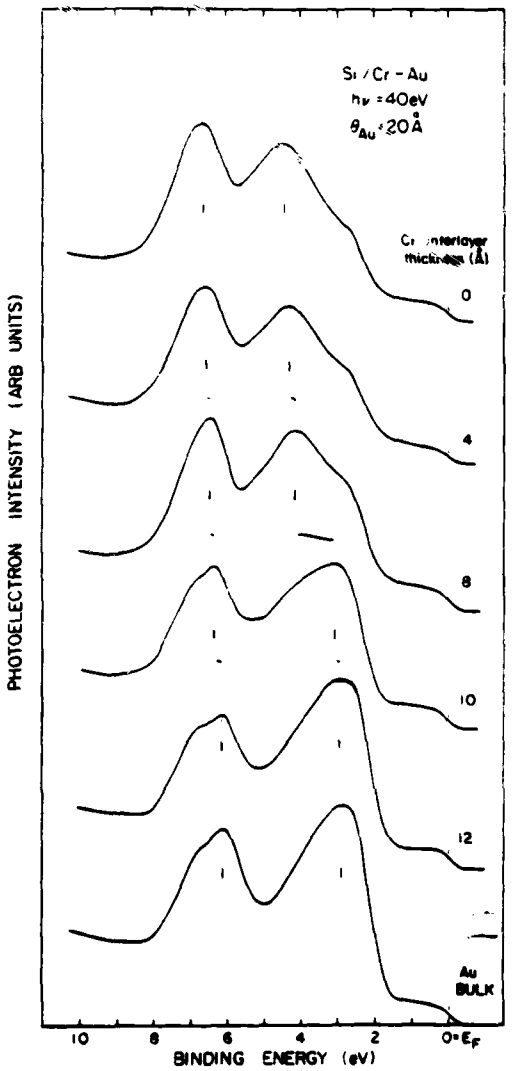

FIG. 1. Valence-band EDC's of the Si-Cr-Au system as a function of the Cr interlayer thickness at a fixed Au coverage of 20 Å. The variation of the energy separation of the Au 5*d* main features (vertical lines) emphasizes the Si-Au intermixing takes place in the presence of the interlayer for Cr coverage below 9 Å but is sharply reduced for higher interlayer thickness.

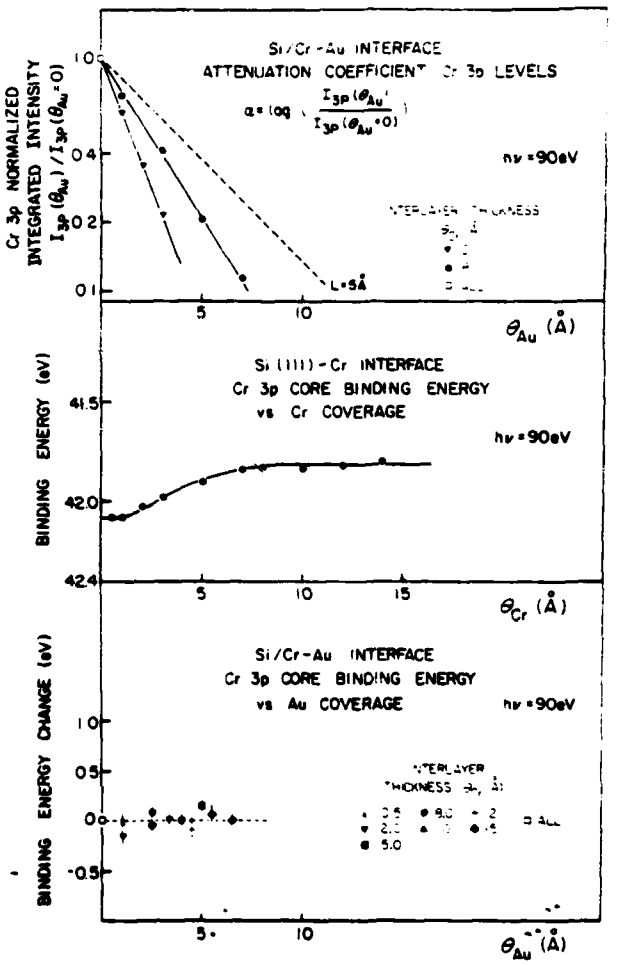

FIG. 2. Top: attenuation coefficient for the integrated emission intensity of the Cr 3*p* cores as a function of Au coverage on the Si-Cr surface. We show experimental data for Cr interlayer thicknesses of 2 and 8 Å. The dashed line represents the theoretical result for exponential attenuation of the 3*p* based on an electron escape depth $L = 5$ Å. Midsection: binding energy of the Cr 3*p* cores as a function of Cr coverage for Cr–Si(111)-(2×1). The Si-Cr reaction corresponds to a chemical shift of -0.3 eV for the Cr 3*p* cores. Bottom: variation of the 3*p* core binding energy for the Cr atoms in the interlayer as a function of Au coverage. Within experimental uncertainty the average chemical environment of the Cr atoms remains the same after the Si-Au interdiffusion.

In a series of previous papers we showed that the deposition of Cr into the Si(111) surface produces a Si-Cr mixed surface phase of variable composition.[11] When the Si-Cr-Au junction is formed, we now see that Si diffuses into the Au matrix and, in principle, this might imply Si depletion in the Si-Cr region. However, the results shown in Fig. 2 indicate that this is not the case. The Si-Cr reaction which occurs during deposition of Cr on Si(111) produces a chemical shift as large as 0.3 eV for the Cr 3*p* cores (midsection of Fig. 2), but there is no variation of this chemical shift when Au is deposited onto the surface (lowest section). Hence, within experimental uncertainty of ~ 0.1 eV, the average local chemical environment of Cr atoms in the Si-Cr phase remains the same after the Si-Au interdiffusion. This implies that as Si enters the Au overlayer a corresponding amount must enter the Si-Cr phase to maintain the local stoichiometry. The net results of this diffusion is transport of Si atoms through a stable Si-Cr interface phase.

In Fig. 3 we show very important results which demonstrate that a picture in which the Si-Cr phase acts as a diffusion barrier for atomic interdiffusion of Si and Au is inadequate. By measuring the attenuation of the Si 2*p* core emission as a function of Au overlayer for different Si-Cr interlayer thicknesses, we can show that the attenuation is not proportional to the thickness of the Cr "barrier." In Fig. 3 the emission intensity at a given Au coverage and interlayer thickness is normalized to the initial Si 2*p* emission from the Si-Cr phase. For comparison, results for the Si(111)-Au interface without Cr deposition are also shown (dot-dashed line from Ref. 14). The best representation of

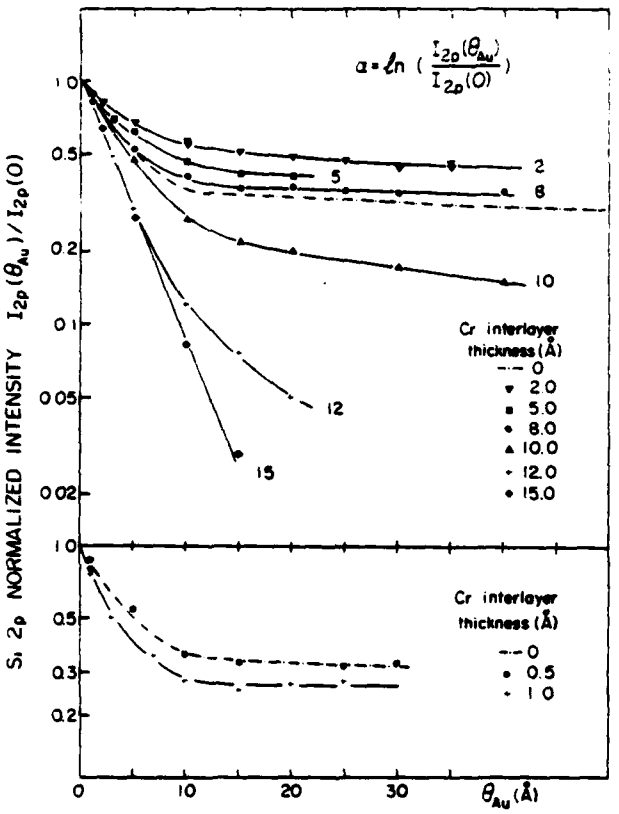

FIG. 3. Attenuation coefficient of the Si $2p$ core emission as a function of Au coverage on the Si-Cr phase. The data show the effect of the presence of the interlayer on Si-Au interdiffusion. The dot-dashed line gives the corresponding result for the Si(111)-Au interface (Ref. 14). For Cr coverage in the monolayer range (lower section), the interlayer slightly reduces Si outdiffusion. For Cr coverages between 2 and 9 Å, the interlayer promotes Si outdiffusion, while for all Cr coverages above 10 monolayers the interlayer sharply reduces the Si-Au reaction.

the *net* effect of the presence of the interlayer on the Si-Au reaction is done by a normalization which takes into account the initial emission from Si surface atoms since this varies with interlayer thickness. Three different ranges of interlayer thickness are clearly evident. First, for Cr coverage of 0–1 Å or monolayer (lower section of Fig. 3), the interlayer weakly affects Si-Au intermixing and reduces Si outdiffusion. Second, for Cr coverages between 1.4 and 9 Å, the interlayer *promotes* Si outdiffusion. Finally, for Cr coverages above 10 monolayers the interlayer *sharply reduces* Si outdiffusion. The maximum promotion effect is obtained at about 2 Å of interlayer thickness, and the trend reverses itself in the monolayer Cr coverage range. Clearly, these results cannot be interpreted with only a simple diffusion barrier model. Hence, there must be a correlation to changes in the local chemistry and energy balance.

In studies of Si(111)-Cr interface formation we suggested[13,14] that there are three formation stages for the Si-Cr interface. In the first ($\theta_{Cr} \lesssim 1$–1.5 monolayers), small core chemical shifts and the relatively rapid attenuation of the substrate emission suggest little or no interdiffusion and weak adatom-substrate interaction ("weak chemisorption"). For $1.5 \lesssim \theta_{Cr} \lesssim 9$–$10$ monolayers, the core levels shift, there is slower attenuation of substrate emission, and the valence states evolve, thus providing evidence of Si-Cr interdiffusion ("reactive interdiffusion"). For $\theta_{Cr} > 10$ monolayers, the Si-Cr reaction is completed and further metal deposition produces an unreacted Cr film on top of the reacted Si-Cr phase ("fully reacted").

The clear one-to-one correspondence between the different stages of Si-Cr interface reaction and the different regimes of catalytic effect of the Cr atoms in the interlayer is compelling and allows us several conclusions. The *promotion* catalytic effect of the interlayer on the Si-Au interdiffusion is related to an increase in reactivity of the Si surface atoms that occur during the reactive interdiffusion stage of the Si-Cr system. The maximum promotion effect occurs just above the onset of the reactive interdiffusion; the interlayer reduces Si outdiffusion below the onset of the Si-Cr reaction. The sharp transition suggests that during the weak chemisorption stage the presence of Cr atoms leaves the energy content of the Si-Si bonds relatively unchanged while the metal atoms "cover up" the ordered surface and act as a thin barrier against the Si-Au interaction. When Cr and Si begin to react, the average Si-Si binding energy is reduced and the broken surface bonds[18] represent sites where the chemically driven Si-Au intermixing may start. The chemically activated character of this interdiffusion process is emphasized by the substantial reduction of intermixing that occurs for interlayer thickness above 9 Å, showing that even very thin layers of *unreacted* Cr on top of the Si-Cr phase act as an effective diffusion barrier for the intermixing.

The gradual reduction in Si outdiffusion that takes place for increasing Cr coverage between 2 and 9 Å is related either to a progressive change of the reactivity of the Si atoms in the Si-Cr phase due to change in bonding character or to the growing importance, of a rate-limiting mass transport step in the intermixing process. Discrimination between the two mechanisms will require temperature-dependent studies (to vary the importance of mass transport in limiting the rate of reaction) or procedure whereby the actual concentration profile of Si atoms in the Si-Cr interlayer can be determined. The latter would allow a quantitative correlation of data such as ours with the effective surface concentration of Si atoms and therefore obtain the *specific activity* of the Cr catalyst as a function of interlayer thickness.

In summary, we have shown that interface reaction at the Si-Au junction can be modulated by Cr atoms at the interface, that these Cr atoms can promote or reduce Si outdiffusion from the bulk, and that the nonmonotonic catalytic trend is related to the existence of several nonequivalent microscopic structures for the Si-Cr binary system at the interface. These results point to the importance of investigations of the influence of the interface catalytic effect on the formation of the Schottky barrier because such studies could clarify the relative importance of metal-induced defects and the formation chemistry of the extended interface region in determining the Schottky barrier heights.

ACKNOWLEDGMENTS

This work was supported by the U.S. Army Research Office under Grant No. DAAG29-83-K-0061. We gratefully acknowledge the support of E. M. Rowe and co-workers at the Wisconsin Synchrotron Radiation Center (supported by NSF Grant No. DMR 78-21080).

[1]For an extensive review, see L. J. Brillson, Surf. Sci. Rep. 2, 123 (1982).

[2]G. Margaritondo, Solid-State Electron. 26, 499 (1983), and references therein.

[3]K. N. Tu, in *Thin Film Interdiffusion and Reactions*, edited by J. M. Poate, K. N. Tu, and J. W. Mayer (Wiley, Chichester, England, 1978).

[4]I. Abbati, L. Braicovich, and A. Franciosi, Phys. Lett. 80A, 69 (1980).

[5]K. Oura, S. Okada, and T. Hanawa, Appl. Phys. Lett. 35, 705 (1979); K. Oura, S. Okada, Y. Kishikawa, and T. Hanawa, *ibid.* 50, 138 (1982).

[6]J. L. Freeouf, J. Vac. Sci. Technol. 18, 910 (1981); P. E. Schmid, P. S. Ho, H. Foll, and G. W. Rubloff, Phys. Rev. Lett. 18, 937 (1981).

[7]L. J. Brillson, R. Z. Bachrach, R. S. Bauer, and J. McMenamin, Phys. Rev. Lett. 42, 397 (1979); L. J. Brillson, G. Margaritondo, and N. G. Stoffel, *ibid.* 44, 667 (1980).

[8]L. J. Brillson, R. S. Bauer, R. Z. Bachrach, and G. Hansson, Phys. Rev. B 23, 6204 (1981); C. F. Brucker and L. J. Brillson, J. Vac. Sci. Technol. 19, 617 (1981).

[9]J. M. Andrews and J. C. Phillips, Phys. Rev. Lett. 35, 56 (1975); G. Ottaviani, K. N. Tu, and J. W. Mayer, *ibid.* 44, 284 (1980).

[10]L. Braicovich, C. M. Garner, P. R. Skeath, C. Y. Su, P. W. Chye, I. Lindau, and W. E. Spicer, Phys. Rev. B 20, 5131 (1979).

[11]A. Franciosi, D. J. Peterman, J. H. Weaver, and V. L. Moruzzi, Phys. Rev. B 25, 4981 (1982).

[12]I. Abbati, L. Braicovich, A. Franciosi, I. Lindau, P. R. Skeath, C. Y. Su, and W. E. Spicer, J. Vac. Sci. Technol. 17, 930 (1980), and references therein.

[13]T. Narusawa, K. Kinoshita, W. M. Gibson, and A. Hiraki, J. Vac. Sci. Technol. 18, 272 (1981); P. Perfetti, S. Nannarone, F. Patella, C. Quaresima, A. Savoia, F. Cerrina, and M. Capozi, Solid State Commun. 35, 151 (1980).

[14]Further valence-band results can be found in A. Franciosi, D. G. O'Neill, and J. H. Weaver, J. Vac. Sci. Technol. B 1, 524 (1983).

[15]Gold film thicknesses of 10, 20, and 100 Å or more on oxidized tantalum gave results which were identical within experimental uncertainty and were representative of bulk Au.

[16]I. Abbati, L. Braicovich, and A. Franciosi, Solid State Commun. 33, 881 (1980); these modifications have been quantitatively discussed through DOS calculations for a model Au$_3$Si silicide in O. Bisi, C. Calandra, L. Braicovich, G. Rossi, I. Abbati, I. Lindau, and W. E. Spicer (unpublished).

[17]With increasing Si content in Au, the Au atoms become more "atomic," shifting the 5*d* valence states to higher binding energy, decreasing the splitting of the two main 5*d* features toward the atomic spin-orbit value (1.5 eV), and affecting the localized *d-d* antibonding states so that the sharp *d* edge of bulk Au 2 eV below E_F is displaced to higher binding energy and only a shoulder is seen in the spectra of reacted Au.

[18]K. Oura, S. Okada, and T. Hanawa, in *Proceedings of the Eighth International Vacuum Congress, Cannes, France, 1980*, edited by F. Adeles and M. Croset [Vide, les Couches Minces (Suppl.) 201, 181 (1980)].

PHYSICAL REVIEW B VOLUME 28, NUMBER 12 15 DECEMBER 1983

Electronic structure of Cr silicides and Si-Cr interface reactions

A. Franciosi and J. H. Weaver
Department of Chemical Engineering and Materials Science, University of Minnesota, Minneapolis, Minnesota 55455

D. G. O'Neill
Synchrotron Radiation Center, University of Wisconsin, Stoughton, Wisconsin 53589

F. A. Schmidt
Ames Laboratory—U.S. Department of Energy, Iowa State University, Ames, Iowa 50011

O. Bisi and C. Calandra
Istituto di Fisica, Università degli Studi di Modena, I-4110 Modena, Italy

(Received 12 August 1983)

We present synchrotron radiation photoemission studies of bulk $CrSi_2$ and silicide phases grown on Si by thermal processing of the Si-Cr interface. Experiment shows that Si-Cr interface formation at room temperature results in reacted phases that differ from both bulk $CrSi_2$ and *in situ*—grown Si-rich $CrSi_2$. Extended—Hückel-theory linear combination of atomic orbitals calculations of the density of states of Cr_3Si, CrSi, and $CrSi_2$ show that Si—Cr bond formation involves Si *p* and Cr *d* states with minimal charge transfer.

I. INTRODUCTION

The formation of refractory metal silicides by heat treatment of silicon-metal interfaces offers promise of widespread application in integrated circuit technology,[1] but the mechanisms that drive interface formation and silicide nucleation are not well understood.[2,3] In part, this is because of limited microscopic information about the electronic and structural properties of interfaces as they evolve during thermal processing.[4–7] Further, there is inadequate understanding of silicides themselves[8–12] and the parameters which influence their bulk properties, including stoichiometry, disorder, segregation, and chemical bonding. In this paper, we focus on the Cr-Si interface and try to resolve some of these uncertainties by examining bulk $CrSi_2$, by following the evolution of interface reaction products as a function of temperature, and by comparing with density of states calculations.

In an earlier investigation of the Si(111)2×1-Cr interface we showed that room-temperature reaction produces intermixed Si-Cr phases for metal coverages of less than 10 monolayers.[11,12] Electronic structure calculations for Cr silicides in simplified lattice structure allowed us to identify trends related to bond formation and stoichiometry variations.[12] The present study extends that work. Important new insight in the silicide electronic structure is obtained through semiempirical calculations for Cr_3Si, CrSi, and $CrSi_2$ in their actual crystal structure, including the amount of Si-Cr *p-d* hybridization, the energy position and width of the nonbonding 3*d* features, and the role of ionicity in the bond. Experimental results for bulk $CrSi_2$ are then understood in terms of substantial *p-d* hybridization and the reduction of the 3*d*-3*d* interaction relative to pure Cr. Comparison with the interface data indicates both similarities and important differences. Temperature-dependent studies show the evolution of $CrSi_2$ and, ultimately, Si segregation at the surface.

II. EXPERIMENTAL

The bulk $CrSi_2$ samples were prepared from ultrapure Iochrome Cr (99.99% purity with less than 100 ppm total impurities) and Dow Corning Si (resistivity of 1000 Ω cm). The starting materials were first arc melted then directionally melted by rf heating using a horizontal cold crucible technique to promote homogeneity and grain growth. Analysis of the resulting $CrSi_2$ ingot showed 48.02 wt. % chromium with lattice constants of $a=4.4277\pm0.0001$ Å and $c=6.3691\pm0.0004$ Å (hexagonal $C40$ lattice) compared to the target value of 48.07 wt. % and lattice constants of 4.436 and 6.369 Å for Cr-rich $CrSi_2$ and 4.428 and 6.363 Å for Si-rich $CrSi_2$. (For further crystallographic information see Table I.) Analysis of the microstructure indicated small amounts of Si, consistent with chemical analysis and measured lattice constants. Clean $CrSi_2$ surfaces suitable for photoemission studies were prepared by cleaving posts of dimension $\sim4\times4\times10$ mm^3 *in situ* immediately before measurements were undertaken.

The Si-Cr interfaces were also prepared *in situ* by Cr deposition on atomically clean Si(111) surfaces. Si wafers were cleaned for this purpose by standard heat treatments[13] and mild sputtering. Interfaces were prepared with identical results on both Si(111)7×7 and Si(111)1×1 surfaces as distinguished through photoemission.[14] The interface behavior at room temperature was the same as reported previously for interfaces on UHV-cleaved Si single crystals in the metal-coverage range explored here ($\Theta>1-2$ monolayers).[11,12] Total pressure during Cr sublimation from a Ta boat was always better than 2×10^{-10}

TABLE I. List of structural parameter for Cr silicides.

	Cr_2Si	CrSi	$CrSi_2$
Crystal structure	cubic $A15$	cubic $B20$	hexagonal $C40$
Space group	$Pm3m$	$P2_13$	$P6_222$
Lattice parameters (Å)	$a=4.5578$	$a=4.607$	$a=4.428$; $c=6.363$
Unit-cell volume (Å^3)	94.68	97.78	108.05
Number of molecules/unit cell	2	4	3
Number of shells within 7 Å			
Si-Si	3	9	20
Si-Cr	5	21	12
Cr-Cr	9	9	8
First-neighbor distance (Å)			
Si-Si[a]	3.947	2.846	2.476
Si-Cr	2.548	2.314	2.476
Cr-Cr[b]	2.279	2.825	3.066

[a]2.351 Å in Si.
[b]2.494 Å in Cr.

Torr with recovery to the operating pressure of $\sim 3\times 10^{-11}$ Torr within ~ 1 min after deposition. The metal coverage of the Si substrate, Θ, was monitored with a quartz thickness monitor and is given in terms of the Si(111) surface atomic density ($\Theta=1$ monolayer for 7.6×10^{14} atoms/cm^2). Thermal processing of the interface was performed by electron bombardment on the back of the Si wafer. The sample temperature was monitored with an infrared pyrometer. Fixed annealing temperatures were used ($400 < T < 1100$ °C), and the annealing time was increased in 10-min cycles until the steady state was reached, as seen from the experimental spectra.

Photoemission measurements were performed using synchrotron radiation from the 240-MeV electron storage ring Tantalus at the University of Wisconsin-Madison and a toroidal grating monochromator. Photoelectron energy distribution curves (EDC's) were recorded with a typical overall resolution (electrons plus photons) of 0.4 eV for the valence-band studies. The Si $2p$ and Cr $3p$ cores were studied at $h\nu=120$ eV (~ 0.5-eV resolution) and 78 eV (~ 1-eV resolution), respectively. Details of the experimental system have been given in Ref. 15.

III. THEORETICAL TECHNIQUES

The energy-band calculations for Cr_3Si, CrSi, and $CrSi_2$ were based on the linear combination of atomic orbitals (LCAO) method in the extended–Hückel-theory approximation.[16] This semiempirical approach greatly simplifies the computation and allows calculations of the electronic energy levels of complex systems such as the bulk silicides of interest here.[17] The same calculational scheme was previously used for the near-noble-metal silicides, yielding results which were in good agreement with experiment.[8,9,18] A detailed description of the method can be found in Ref. 9.

In these calculations, the atomic valence orbitals ϕ_α are expressed as products of the appropriate spherical harmonics times a radial wave function of the form

$$R_\alpha(r)=c_1\chi_\alpha(\xi_1)+c_2\chi_\alpha(\xi_2)\ ,$$

where $\chi_\alpha(\xi)$ are Slater-type orbitals with orbital exponent ξ.[9] The Slater orbital exponents have been adjusted to reproduce the electronic bands of pure Si (Ref. 19) and Cr (Ref. 20). The resulting value of the parameters ξ_1 and ξ_2 are shown in Table II, together with the constants c_1 and c_2.[21]

The Coulomb integrals $\alpha_i \simeq \langle \phi_i \mid H \mid \phi_i \rangle$ are set equal to the negative of the valence-orbital ionization potential I_i for the δ_i orbital,[22] and the resonance integrals $\beta_{ij}=\langle \phi_i \mid H \mid \phi_j \rangle$ are approximated by[9]

$$\beta_{ij}=-k(I_iI_j)^{1/2}S_{ij}\ ,$$

where S_{ij} are overlap integrals and $k=2.5$, as suggested by Breese and Perkins[23] for metallic systems. The I_i can be interpreted as charge-dependent potentials and an iterative procedure can be built up allowing I_i to vary as

$$I_i(q)=C_i+B_iq\ ,$$

where q is the excess charge per atom. This charge was calculated through a Mulliken population analysis,[24] and the iterative procedure was stopped when the charge variation between two successive iterations was less than 0.005 electrons per atom. The numerical values used for the parameter C_i and B_i (Ref. 25) for the valence orbitals ϕ_i are also shown in Table II.

IV. EXPERIMENTAL RESULTS

Photoelectron energy distribution curves (EDC's) for the valence bands of bulk $CrSi_2$ cleaved *in situ* are shown in Fig. 1 for photon energies between 16 and 120 eV. The EDC's have been approximately normalized to the main emission features and are given in arbitrary units. The Si $2p$ and Cr $3p$ levels are shown in the lower part of the figure for photon energies which give comparable surface

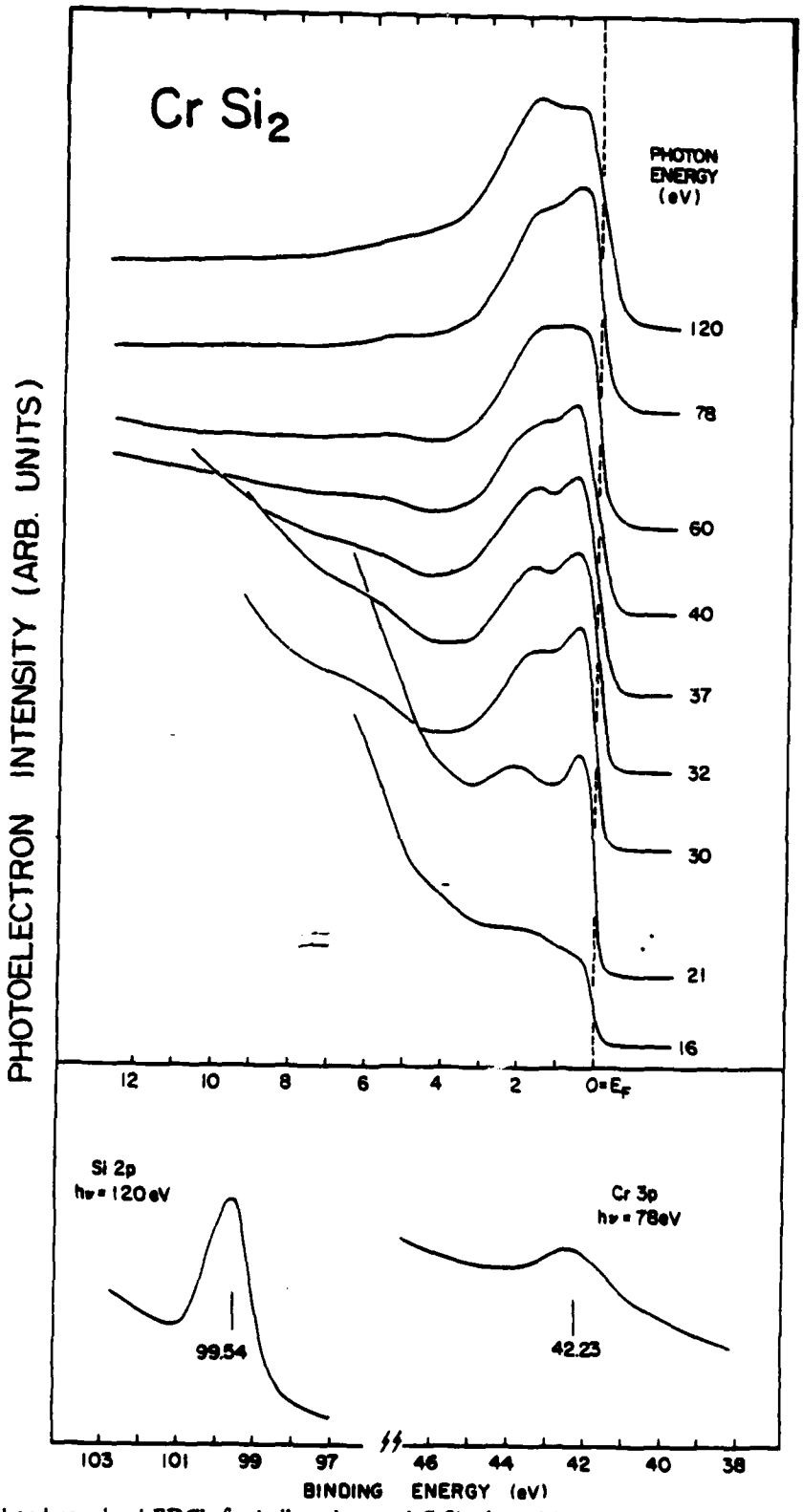

FIG. 1. Valence-band and core-level EDC's for bulk, polycrystal $CrSi_2$ cleaved *in situ*. The measured binding energy of the Si 2*p* (bottom left) and Cr 3*p* (bottom right) cores is indicated in the figure and the corresponding experimental uncertainty is 0.10 and 0.14 eV, respectively.

sensitivities for the Si and Cr core levels (120 and 78 eV). The relative intensity of the two main valence-band spectral features varies with photon energy, particularly at low photon energy where final-state effects are important, but both features show very little dispersion for $h\nu > 25$ eV, and we associate them with structures in the density of states (DOS). The valence-band emission of $CrSi_2$ at $h\nu = 50$ eV, where the metal *d* photoionization cross sec-

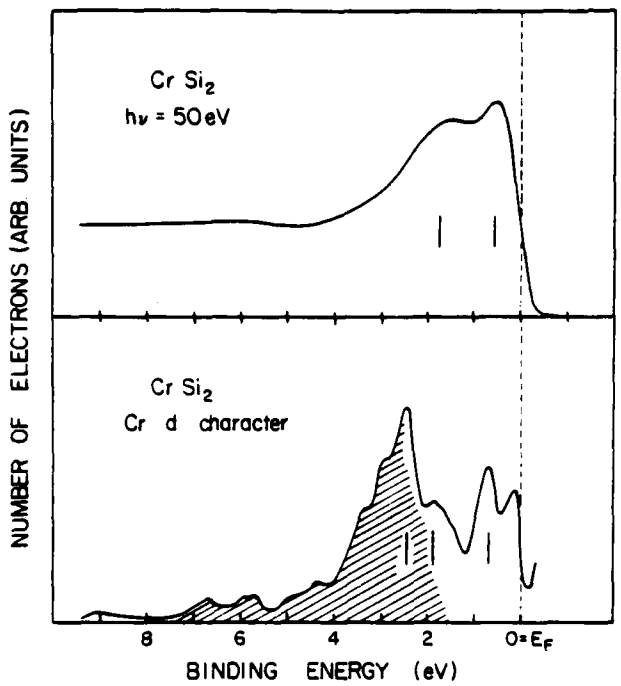

FIG. 2. Comparison of valence-band emission of $CrSi_2$ at $h\nu = 50$ eV with the l-projected partial DOS showing the Cr-derived $3d$ character. The shaded area corresponds to the $3d$ states that have hybridized with the Si p states (in bonding combinations). Photoemission emphasizes the nonbonding d features in these $3d$-metal disilicides. The main spectral features 0.6 eV below E_F reflects such states, while important contributions to the broad shoulder centered at 1.7 eV should come from both bonding and nonbonding states.

tion dominates, is compared with the theoretical Cr-derived $3d$ character in Fig. 2. The shaded region corresponds to d states which are hybridized with Si p states. (See the following section.)

The results for the Si(111)-Cr interface are summarized in Figs. 3 and 4. In Fig. 3, the valence band, Si $2p$ and Cr $3p$ core emission from the interface at Cr coverage $\Theta = 10$ monolayers is compared with the valence band and core emission of bulk $CrSi_2$. Cr deposition on Si(111)7×7 results in the formation of an extended intermixed Si-Cr phase for $1.5 < \Theta < 10$ which is identical to what has been discussed for the Si(111)2×1-Cr interface. For $\Theta > 10$, a film of unreacted Cr forms over the reacted interface. The effects of annealing 50-Å Cr films evaporated on the Si wafer are shown in Fig. 4. The topmost curve represents the bulk Cr-like emission, and the dotted line superimposed on this spectrum represents bulk $CrSi_2$ from Fig. 1. EDC's displaced downward show the effect of 10-min annealing cycles at successively higher temperature in the range 400—1100 °C. Only at 400 ± 50 °C were two heating cycles needed to reach steady state.

V. THEORETICAL RESULTS

Figure 5 shows the total DOS for Cr_3Si, CrSi, $CrSi_2$ and pure Cr, as calculated with the parameters of Table II. The corresponding DOS projections in Cr-derived d and s-p states are compared with Si-derived s-p states in Fig. 6. These DOS's have been calculated using a mesh of 210 $\vec{k}$ points in the irreducible Brillouin zone for $CrSi_2$ and 84 $\vec{k}$ points for Cr_3Si and CrSi. A broadening of 0.1 eV has

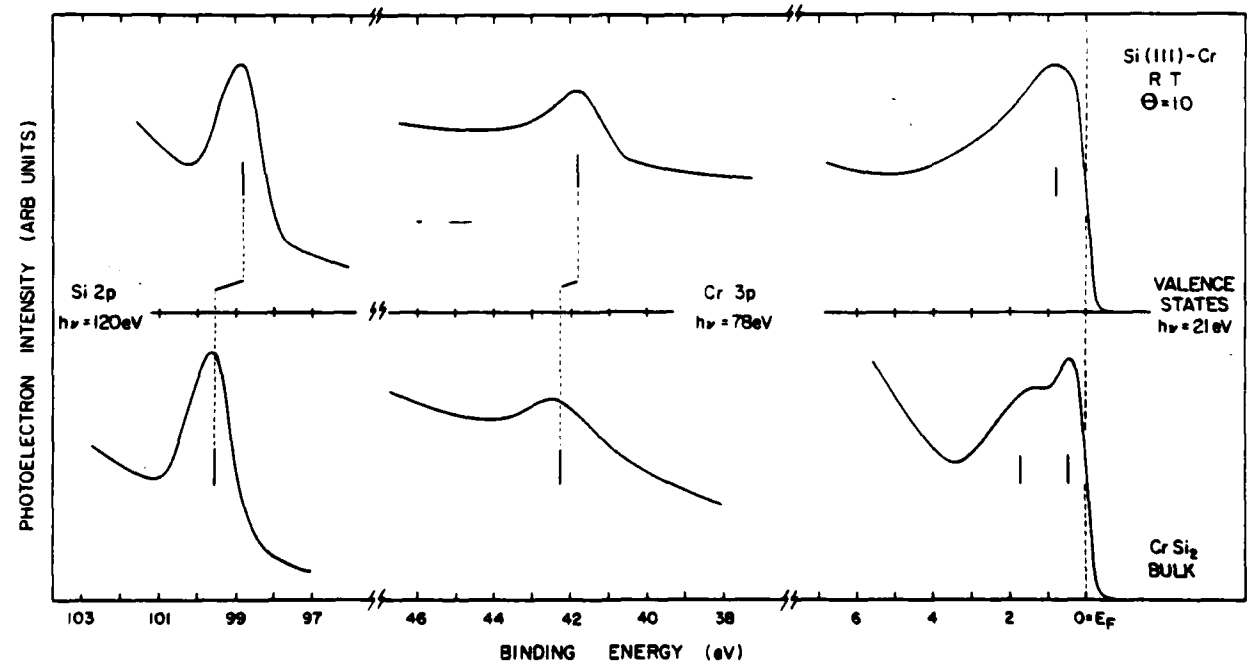

FIG. 3. Comparison of valence band and core emission for $CrSi_2$ to the Si(111)-Cr interface at room temperature and Cr coverage $\Theta = 10$ ML. The photon energies have been chosen to obtain similar surface sensitivity for core and valence-band features. The interface reaction products (top) show a clearly different electronic structure with respect to $CrSi_2$, including core-binding energy differences of -0.76 and -0.42 eV, respectively, for the Si $2p$ and Cr $3p$ levels.

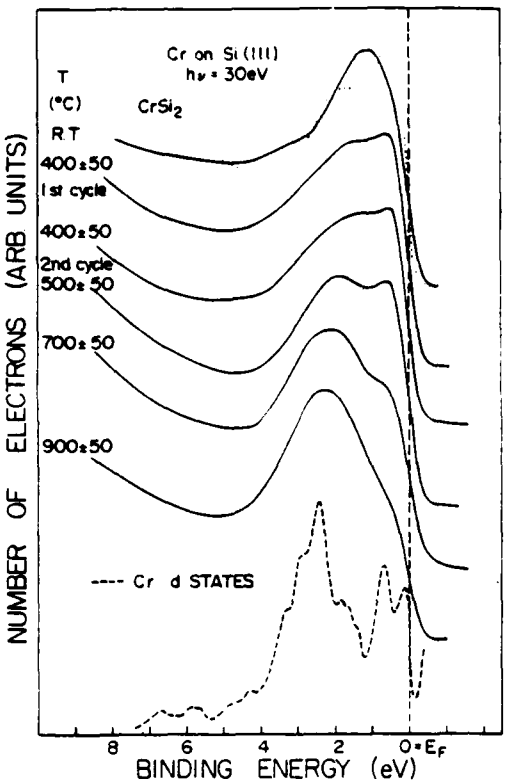

FIG. 4. Valence-band emission at $h\nu = 30$ eV of the Si-Cr junction as a function of 10-min annealing cycles at increasing temperature. The topmost solid curve corresponds to a 50-Å Cr film deposited on Si(111) at room temperature. Superimposed on it is an EDC for bulk $CrSi_2$ (dotted line). The bottom-most curve (dashed line) shows for comparison the theoretical Cr-derived 3*d* character. At ~400°C, a disilicide-like doublet emerges while Cr 3*p* and Si 2*p* core features show binding energies consistent, within experimental uncertainty, with the values observed for bulk $CrSi_2$. Annealing at higher temperatures enhances emission from the Si-metal *p*-*d* hybrid states 2–3 eV below E_F (see Fig. 2) and the Si 2*p* and Cr 3*p* core-binding energies remain $CrSi_2$-like. The relative core intensity shows a Si-rich stoichiometry at the surface.

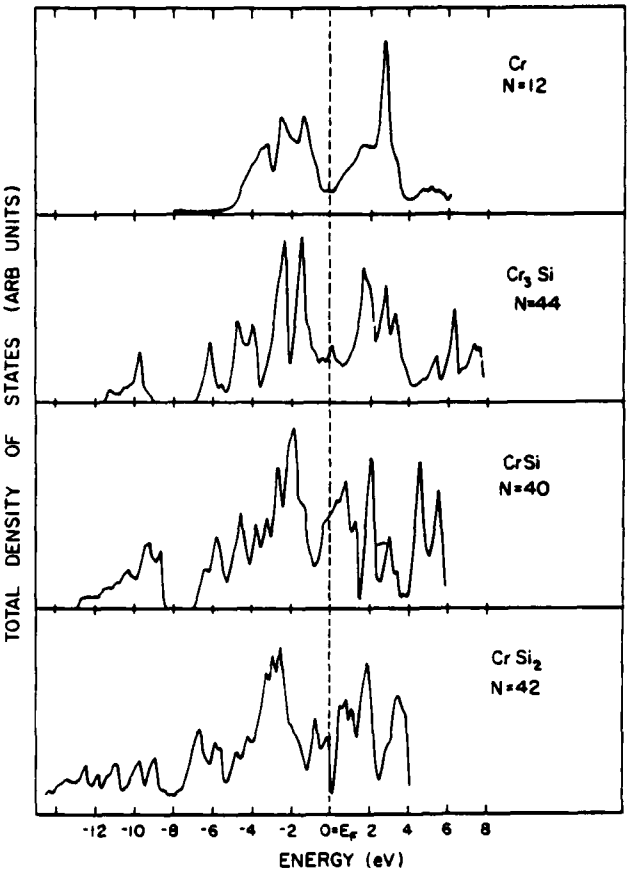

FIG. 5. Total densities of states for Cr and Cr silicides with arbitrary normalization. The corresponding number of states/(eV unit cell) can be obtained through the total number N of valence electrons per unit cell.

been used to obtain the DOS in Figs. 5 and 6. The excess charge per atom,[9] as calculated from the iterative procedure outlined in Sec. III, is the charge transfer per atom due to the Si–Cr chemical bond and is given in Table III.

The total DOS for Cr is very similar to that of Laurent *et al.*[26] Strong 3*d*-3*d* hybridization splits the *d* bands into two groups of states, with the bonding combination generally below E_F and the antibonding states mostly above E_F. The Fermi level itself falls in a region of low state density.[27] Three main DOS features at about −1.3, −2.5, and −3.5 eV correspond to states of different symmetry[28] and spatial extent.[29] Photoemission clearly emphasizes the structure nearest E_F while the deeper two appear unresolved at ~3 eV.[30]

TABLE II. Input parameters used in the calculations of the electronic structure of Cr silicides. ξ from fitting of the energy bands of elemental Si (Ref. 19) and Cr (Ref. 20), C_1 and C_2 from atomic data tables (Ref. 21), C_l and B_l from Ref. 25.

Valence orbital	Si		Cr		
ϕ_l	3*s*	3*p*	4*s*	4*p*	3*d*
c_1	1.0	1.0	0.4458	1.0	0.4071
ξ_1 (a.u.$^{-1}$)	2.25	1.65	2.70	2.0	4.369
c_2	0	0	0.6433	0	0.7324
ξ_2 (a.u.$^{-1}$)			1.49		1.768
C_l (eV)	14.82	7.75	6.60	3.52	7.18
B_l (eV)	12.39	10.13	7.14	5.90	11.90

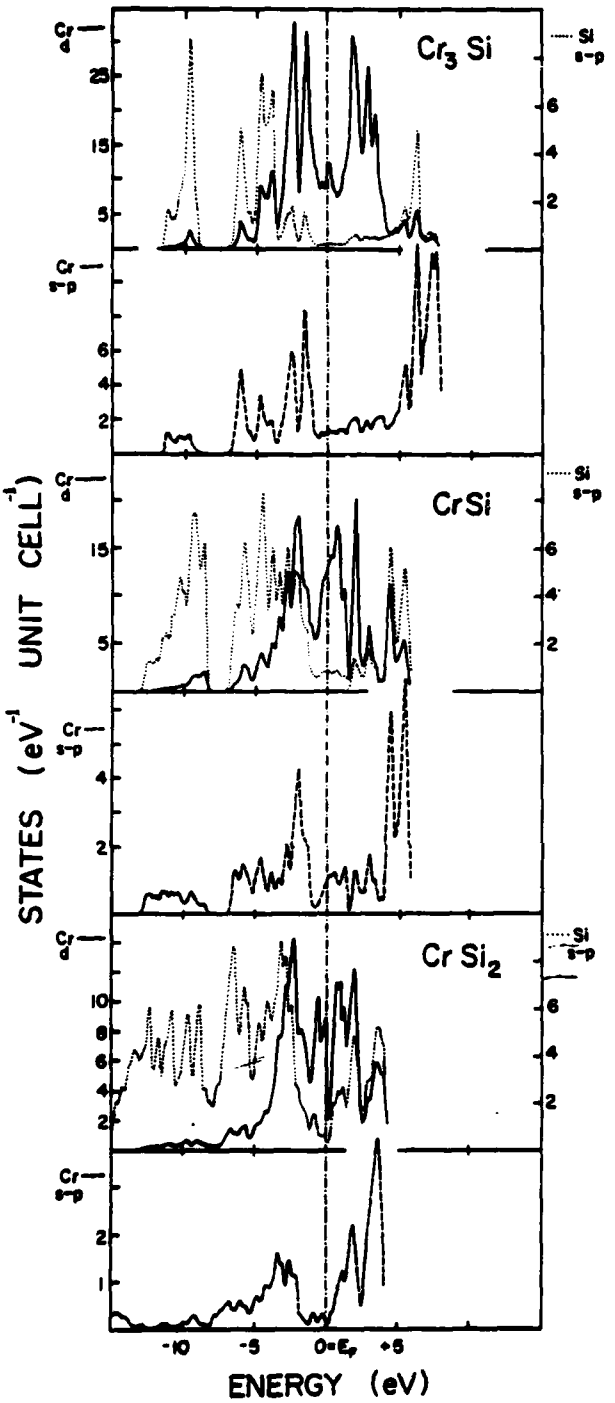

FIG. 6. Partial DOS for Cr silicides showing the l-projection of the Cr-derived d (solid line) and s-p (dashed line) character versus the Si-derived s-p character (dotted line). The chemical bonding depends on the coupling of Cr d and Si p states. $CrSi_2$ is the only Cr silicide to have dominant nonbonding DOS feature within 1 eV of E_F. The Si s states are not directly involved in the bonding and fall more than 8 eV below E_F.

VI. DISCUSSION

The chemical bond for the Cr and nearly-noble-metal silicides is very similar[8-10,12,31] with coupling of Cr 3d and Si p states and a reduction of the Si s-p hybridization. For Cr silicides, many of the occupied 3d states bond with Si, and the resulting silicide DOS is determined by two competing trends. First, the Cr-Si hybridization produces bonding features below and antibonding features above E_F, and the 3d-band width is broadened. Second, the Cr 3d-3d interaction is reduced, the electronic configuration becomes more atomic,[8,32] and the 3d-band width is reduced. The importance of the first mechanism in determining the valence-band structure is greater than that for the nearly-noble-metal silicides, because there are few occupied d states not involved in the bonding with Si (nonbonding d states). For the Ni silicides, on the other hand, the narrower nonbonding 3d states dominate the EDC's and changes in the Ni-Ni interaction determine most DOS changes in the Ni_2Si-NiSi-$NiSi_2$ series.[8]

Previous DOS calculations for Cr silicides in their real crystal structures exist only for the $A15$ structure Cr_3Si where the total and l-projected density of states as obtained by Arbman and Jarlborg[33] are in good agreement with those presented here.[34] In Cr_3Si, the Cr-Cr interaction dominates in determining the electronic structure, and the total DOS in Fig. 5 is reminiscent of the 3d-3d bonding-antibonding separation in bulk Cr. Indeed, the Cr-derived states between -4 and $+4$ eV do not mix with Si states. The Si—Cr p—d bonding combinations are evident between -4 and -6.5 eV. The corresponding antibonding states fall more than 4 eV above E_F. As in other metal-rich silicides,[8] the Si sp^3 hybridization is replaced by Si-Cr p-d coupling and the s states form an isolated band around -10 eV.

For CrSi (cubic, $B20$-type structure), the Si-Cr p-d bonding states appear between -1 and -6 eV, and nonbonding d character is present at the Fermi level. The p-d antibonding states are ~ 4 eV above E_F, and a gap separates the s states from the rest of the DOS, even if the value of the energy separation is decreased with respect to Cr_3Si because of the larger Si-Si interaction. In $CrSi_2$ (hexagonal, $C40$ type) this gap no longer exists, and states more than -7 eV below E_F account for most of the Si-derived s character. The p-d bonding states appear between -1 and -5 eV, and the empty antibonding orbitals now start only ~ 1 eV above E_F.

The results of Fig. 5 for $CrSi_2$ show that E_F falls in a region of low, but nonzero, state density. Figure 7 shows the DOS near E_F, and the energy bands near E_F are repro-

TABLE III. Excess charge Δq for atom as calculated from the iterative procedure outlined in Sec. III. The procedure was stopped when the charge variation between two successive iterations was less than 0.005 electron/atom. The charge transfer is always less than 0.5% of the valence charge/atom for Cr and less than 1% for Si.

Silicide	Δq Cr (electrons/atom)	Δq Si (electrons/atom)
Cr_3Si	-0.013	$+0.038$
CrSi	-0.029	$+0.029$
$CrSi_2$	$+0.015$	-0.007

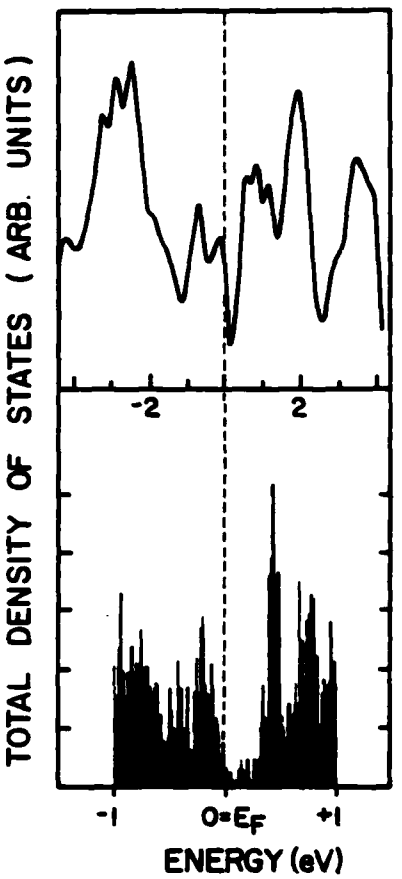

FIG. 7. Detail of the total DOS for $CrSi_2$ near E_F. Top: DOS obtained with a broadening of 0.1 eV. Bottom: High-resolution histogram plot showing the small but finite DOS at E_F.

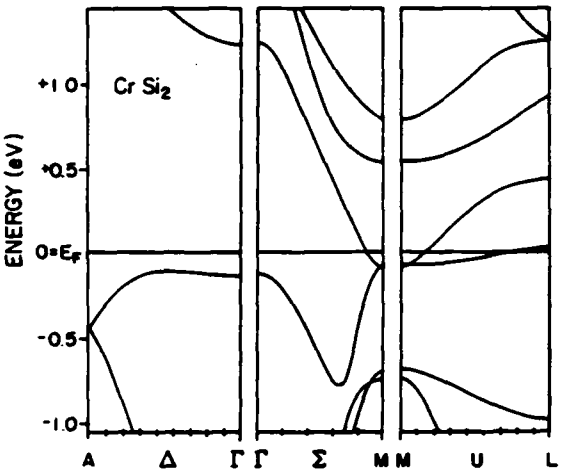

FIG. 8. Energy-band diagram for $CrSi_2$ showing selected energy levels near E_F along high-symmetry lines in the $C40$ structure Brillouin zone. Two bands are shown to cross E_F near the M and L symmetry points. The resulting carrier density is estimated at 8.1×10^{19} carrier/cm^3 and is typical of a semimetal.

duced in Fig. 8. The crossing of the bands near M rules out a forbidden gap and semiconducting behavior for $CrSi_2$. The carrier density in $CrSi_2$ can be estimated by counting the fraction of states involved in the band crossing out of the 2058 $\vec{k}$ points in the Brillouin zone. The resulting estimate of 8.1×10^{19} carrier/cm^3 is typical of a semimetal. (In our investigations, E_F was determined experimentally through measurements of Au and Cr films evaporated *in situ*. The spectra of Fig. 1 are in agreement with the metallic character of $CrSi_2$, showing a low-energy cutoff centered at E_F with a width determined by the experimental resolution.[35] The low calculated carrier density may explain why $CrSi_2$ has been reported to be a metal by some authors and a small-gap semiconductor by others.[36])

Our calculations show little charge transfer for these three silicides, always less than 1% of the valence charge/atom for Cr to Si in Cr_3Si and CrSi and completely negligible in $CrSi_2$ (see Table II). This suggests that ionicity is a minor contributor to the bond. Our calculated charge transfer for Cr_3Si appears in contrast to the large charge transfer from Si to metal suggested by Staudemann[37] and Mattheiss and Hamann.[38] However, as discussed by Pickett *et al.*,[39] numerical values depend on the method used to separate the space around the Si or metal atoms. This problem does not exist for our LCAO decomposition and, furthermore, our calculated charge transfer is consistent in magnitude and sign with the electronegativity difference (Pauling electronegativity is 1.6 for Cr and 1.8 for Si).

Previous calculations for the Cr_3Si, CrSi, and $CrSi_3$ in the Cu_3Au and CuAu structures showed qualitatively the same chemical bonding as the present calculations, i.e., Si-Cr p-d coupling, removal of Si sp^3 hybridization, and small charge transfer.[12] The present results show a general lowering of the $3d$-derived occupied DOS for CrSi and $CrSi_3$. We suggest that such differences arise from the use of the real silicide geometry in the present calculations.

The disilicide of Cr is of special interest since it is the only Cr silicide known to grow on Si upon reaction[2] at 450°C. In previous work, however, we demonstrated[8] that room-temperature deposition of Cr onto cleaved Si resulted in intermixing for Cr coverages up to 10 monolayers (ML). This reacted layer constitutes the "real" interface between Si and Cr and is gradually covered with unreacted metal upon further Cr deposition. The implication is, of course, that this reacted layer determines the junction profile and transport properties of any macroscopic Si-Cr junction. Therefore, after examining in Fig. 2 the electronic structure of $CrSi_2$ on the basis of our theoretical calculations, we compare in Fig. 3 the properties of $CrSi_2$ with those of the interface reaction product for $\Theta=10$ ML. The valence states of $CrSi_2$ show a main peak at 0.6 eV and a broad shoulder at about 1.7 eV (extending between 1.3 and 3 eV). Our calculations predict a main nonbonding $3d$ feature 0.65 eV below E_F, while important contributions to the broad shoulder extending between 1.3 and 3 eV come from the $3d$ bonding states at 2.4 eV in the calculations and from the nonbonding $3d$ states around 1.8 eV. The identification is in agreement with the sys-

tematic trend in the DOS of the 3*d* metal disilicides (Ref. 40) and confirms that ultraviolet photoemission emphasizes the nonbonding 3*d* features with respect to the *d* states directly involved in the bond with Si.

For Cr deposition onto Si(111) (Fig. 3), the Cr-derived 3*d* states quickly dominate the valence-band emission and give rise to a broad maximum that shifts with coverage toward E_F until the fully reacted layer is formed ($\Theta = 10$ ML). Comparison of the valence bands of the interface reaction products and bulk $CrSi_2$ shows that the double 3*d* structure (0.6 and 1.7 eV) characteristic of the disilicide is not present for the interface and only a broad 3*d* peak appears at 0.75 eV in the interface spectrum (full width at half maximum of 2.6 eV compared to 2.1 eV for $CrSi_2$).

The binding energies of the Si 2*p* and Cr 3*p* cores are important in gauging interface reaction. The Cr 3*p* and Si 2*p* cores both shift toward lower-binding energy for coverages $1 < \Theta < 10$ and for $\Theta \geq 10$ stabilize at 41.8 ± 0.1 and 98.80 ± 0.1 eV below E_F.[41] Analogous results for $CrSi_2$ show a binding energy of 99.54 ± 0.1 eV for the Si 2*p* and 42.23 ± 0.14 eV for the Cr 3*p*, identical within experimental uncertainty to the 3*p* core binding energy in bulk Cr.[42] Therefore, the interface-reaction product exhibits Si 2*p* and Cr 3*p* core shifts of 0.74 and 0.42 eV to lower binding energy relative to $CrSi_2$, indicating that the electronic configuration differs substantially from $CrSi_2$.

Examination of the theoretical Cr-Si results of Fig. 7 shows that only $CrSi_2$ exhibits dominant 3*d* nonbonding DOS features within 1 eV of E_F. Since the photoemission results for all 3*d* metal silicides[40] are in good agreement with 3*d*-projected densities of states where the nonbonding *d* character is emphasized, we conclude that *none* of the bulk Cr silicides examined theoretically exhibits electronic structure sufficiently close to the interface-reaction product to allow unambiguous identification. Clearly, what is needed is direct insight into the structural character of the interface so that theoretical modeling can be more specific.

To examine whether the interface layer would evolve to $CrSi_2$ upon thermal treatment, we annealed 50-Å Cr films on Si(111) and monitored the valence-band and core-level features. In particular, annealing temperatures in the 400—1100 °C range were emphasized because Rutherford backscattering and x-ray-diffraction investigations[2,43] have shown $CrSi_2$ to be the only growth phase to form at the interface. The topmost curve of Fig. 4 represents a thick Cr film on Si(111). Annealing at 400 ± 50 °C gives strong Si 2*p* emission 99.45 ± 0.14 eV below E_F and shifts the Cr 3*p* cores from the Cr metal position of 42.22 eV to 42.14 ± 14 eV, converging on the values of 99.54 ± 0.10 and 42.23 ± 0.14 eV observed for bulk $CrSi_2$. Correspondingly, the valence-band emission becomes $CrSi_2$-like, though the spectral features are broader. Annealing above 500 °C results in the emergence of enhanced emission 2—3 eV below E_F. Above ~700 °C, this new feature dominates, and the 3*d* nonbonding structure near E_F is only a weak shoulder.

These modifications of the valence states result from the formation of a Si-rich silicide at the surface. Enhanced emission 2—3 eV below E_F reveals an increased number of Si-Cr *p*-*d* hybrid orbitals relative to the nonbonding *d* states. Further, the ratio of the integrated emission from Si 2*p* and Cr 3*p* cores is 1.8 times higher for the 600 ± 50 °C annealed interface silicide than for cleaved $CrSi_2$, indicating a marked enrichment in the Si concentration. Finally, throughout the high-temperature annealing cycles, during which the valence states are modified, the Si 2*p* and Cr 3*p* cores maintain the bulk $CrSi_2$ binding energy (experimental scatter of ~0.1 eV). Low-energy electron diffractive and Auger studies of $CrSi_2$ nucleation on Si(111) by Oura *et al.* suggested that annealing above 600°C—900°C produces several atomic layers of silicon over a crystalline silicide layer. Our results confirm the increase in the Si surface concentration but show that the Si-Cr bonding remains fundamentally $CrSi_2$-like, with no evidence of formation of several layers of *elemental* silicon at the surface. This is also consistent with analogous studies of Pd_2Si.[44]

The results of Fig. 6 are important in discussions of room temperature Si-Cr interface reaction. We have shown that a $CrSi_2$-like phase nucleates at relatively low temperature (400 ± 50 °C) and that this phase, while lacking long-range order,[45] exhibits characteristic $CrSi_2$-like valence and core features. Therefore, both experimental and theoretical results indicate that the room-temperature interface-reaction product is not simply a disordered $CrSi_2$ phase.

Finally, we observe that the Si-rich $CrSi_2$ phase shows characteristic enhancement of the valence-band emission 2—3 eV below E_F while exhibiting a bulk $CrSi_2$-like binding energy for the Si 2*p* and Cr 3*p* cores. Therefore, unlike the case of the Si(111)-Pd interface where room-temperature reactions seem to yield a locally Si-rich Pd_2Si phase, we find evidence that room-temperature Si(111)-Cr interface reaction does not yield a nonstoichiometric version of $CrSi_2$, the first silicide-nucleation phase.

The understanding of Si-metal interface reaction requires the characterization of the interface-reaction products as a function of the various reaction parameters, including temperature and metal coverage. We have sought to show how a systematic experimental and theoretical investigation of the electronic properties of interface and bulk Si-metal compounds can increase our understanding of both interface morphology and of the parameters, such as long-range order and stoichiometry variation, that affect the silicide-electronic structure.

ACKNOWLEDGMENTS

This work was supported by the U. S. Army Research Office under Contract No. DAAG29-83-K-0061. The Synchrotron Radiation Center, University of Wisconsin is supported by the National Science Foundation under Grant No. DMR-80-20164, and we acknowledge the warm hospitality and cheerful support of that laboratory. We gratefully acknowledge the expert sample preparation and characterization work by O. D. McMasters of Ames Laboratory. The work at the University of Modena was supported by the Centro di Calcopo Universita di Modena. One of us (F.A.S.) acknowledges support of the U.S. Department of Energy Contract No. W-7405-ENG-82.

[1]S. P. Muraka, J. Vac. Sci. Technol. 17, 775 (1980); G. Ottaviani, *ibid.* 18, 924 (1981).

[2]K. N. Tu, in *Thin Film Interdiffusion and Reactions*, edited by J. M. Poate, K. N. Tu, and J. W. Mayer (Wiley, Chichester, England, 1978).

[3]K. N. Tu, Appl. Phys. Lett. 23, 493 (1973).

[4]J. E. Rowe, S. B. Christman, and G. Margaritondo, Phys. Rev. Lett. 35, 1471 (1975); G. Margaritondo, J. E. Rowe, and S. B. Christman, Phys. Rev. B 14, 5396 (1976).

[5]L. Braicovich, I. Abbati, J. N. Miller, I. Lindau, S. Schwarz, P. R. Skeath, C. Y. Su, and W. E. Spicer, J. Vac. Sci. Technol. 17, 1005 (1980); I. Abbati, L. Braicovich, and B. De Michelis, Solid State Commun. 36, 145 (1980).

[6]J. L. Freeouf, G. W. Rubloff, P. S. Ho, and T. S. Kuan, Phys. Rev. Lett. 43, 1836 (1979); P. S. Ho, P. E. Schmid, and H. Foll, *ibid.* 46, 782 (1981).

[7]P. J. Grunthaner, F. J. Grunthaner, A. Madhukar, and J. W. Mayer, J. Vac. Sci. Technol. 19, 649 (1981); N. W. Cheung, P. J. Grunthaner, F. J. Grunthaner, J. W. Mayer, and B. M. Ullrich, *ibid.* 18, 917 (1981).

[8]J. H. Weaver, V. L. Moruzzi, and F. A. Schmidt, Phys. Rev. B 23, 2916 (1981); A. Franciosi, J. H. Weaver, and F. A. Schmidt, *ibid.* 26, 546 (1982).

[9]O. Bisi and C. Calandra, J. Phys. C 14, 5479 (1981); O. Bisi and L. W. Chiao, Phys. Rev. B 25, 4943 (1982).

[10]Y. Chabal, J. E. Rowe, J. M. Poate, A. Franciosi, and J. H. Weaver, Phys. Rev. B. 26, 2748 (1982); A. Franciosi, J. H. Weaver, Y. Chabal, J. E. Rowe, and J. M. Poate, J. Vac. Sci. Technol. 21, 624 (1982).

[11]A. Franciosi, D. J. Peterman, and J. H. Weaver, J. Vac. Sci. Technol. 19, 657 (1981).

[12]A. Franciosi, D. J. Peterman, J. H. Weaver, and V. L. Moruzzi, Phys. Rev. B 25, 4981 (1982).

[13]See, for example, D. E. Eastman, J. Vac. Sci. Technol. 17, 492 (1980), and references therein.

[14]D. E. Eastman, F. J. Himpsel, and J. F. van der Veen, Solid State Commun. 35, 345 (1980).

[15]G. Margaritondo, J. H. Weaver, and N. G. Stoffel, J. Phys. E 12, 662 (1979).

[16]R. Hoffman, J. Chem. Phys. 39, 1397 (1963).

[17]A summary of the structural properties of $CrSi_2$, CrSi, and Cr_3Si is given in Table I. As for many other silicides, the large number of atoms per unit cell and the complex crystal structure make first-principles calculations difficult and fairly expensive. Semiempirical approaches or calculations based on simplified lattice structures are often used to gain insight into the character of the metal—silicon bond.

[18]P. S. Ho, G. W. Rubloff, J. E. Lewis, V. L. Moruzzi, and A. R. Williams, Phys. Rev. B 22, 4784 (1980).

[19]J. R. Chelikowski and M. L. Coehn, Phys. Rev. B 14, 556 (1976).

[20]R. P. Gupta and S. K. Sinha, Phys. Rev. B 3, 2401 (1971).

[21]Values taken from tables of atomic wave functions: E. Clementi and C. Roetti, At. Data Nucl. Data Tables 14, 177 (1974).

[22]H. Basch, A. Viste, and H. B. Gray, J. Chem. Phys. 44, 10 (1966).

[23]A. Breeze and P. G. Perkins, J. Phys. F 5, 255 (1975).

[24]R. S. Mulliken, J. Chem. Phys. 23, 1833 (1955).

[25]The parameters were taken from atomic spectra data of H. Basch, A. Viste, and H. B. Gray, J. Chem. Phys. 44, 10 (1966); R. C. Baetzold, *ibid.* 55, 4355 (1971).

[26]D. Y. Laurent, J. Callaway, J. L. Fry, and N. E. Breuer, Phys. Rev. B 23, 4977 (1981).

[27]The bonding-antibonding splitting differs from the crystal-field splitting that removes the degeneracy of states with t_{2g} (xy,yz,xz) and e_g $(x^2-y^2,3z^2-r^2)$ symmetry in a cubic environment. In fact, the average contribution to the 3*d* DOS below E_F is of the same order of magnitude for t_{2g} (22.6%) and e_g (16%) states.

[28]The LCAO analysis shows that the structure at -1.3 eV is approximately 82% t_{2g} character while those at -2.5 and -3.5 eV have approximately 60% t_{2g} and 40% e_g character.

[29]The states that lie deeper in energy exhibit larger radial extension. See K. M. Ho, B. N. Harmon, S. H. Liu, and S. K. Sinha, Phys. Rev. B 14, 1283 (1976).

[30]Results for Cr films evaporated on inert substrates are in good agreement with data for bulk Cr samples. See. J. Barth, F. Gerken, K. L. I. Kobayashi, J. H. Weaver, and B. Sonntag, J. Phys. C 13, 1369 (1980).

[31]P. S. Ho, G. W. Rubloff, J. E. Lewis, V. L. Moruzzi, and A. R. Williams, Phys. Rev. B 22, 4784 (1980).

[32]A. R. Williams and N. D. Lang, Phys. Rev. Lett. 40, 954 (1978).

[33]G. Arbman and T. Jarlborg, Solid State Commun. 26, 857 (1978); T. Jarlborg, J. Phys. F 9, 283 (1979).

[34]Some differences do exist with respect to Ref. 33 for the 3*d*-derived DOS *above* E_F. This is not surprising since our LCAO calculations are better suited to reproduce the ground state of the system.

[35]Valence-band photoemission, however, may not discriminate between a metal and a semiconductor with band bending in the near-surface region.

[36]J. P. Suchet, *Crystal Chemistry and Semiconduction in Transition Metal Binary Compounds* (Academic, New York, 1971), p. 101.

[37]J. L. Staudenmann, Solid State Commun. 23, 121 (1977).

[38]L. Mattheiss and D. Hamann, Solid State Commun. 38, 689 (1981).

[39]W. E. Pickett, K. M. Ho, and J. L. Cohen, Phys. Rev. B 19, 1734 (1979); 19, 1751 (1979).

[40]J. H. Weaver, A. Franciosi, and V. L. Moruzzi (unpublished) discuss bonding for the silicides of Ca through Cu. A brief preliminary report appeared as A. Franciosi and J. H. Weaver, Physica 117&118B, 846 (1983).

[41]We did not attempt a deconvolution of the spin-orbit components of the Si 2*p* and Cr 3*p* doublets. The quoted binding energies correspond to the peak intensities with respect to a linearly extrapolated secondary background.

[42]For a ~300-Å-thick Cr film evaporated on oxidized Ta substrate we obtained E_B $(3p)=42.22\pm0.10$ eV, in good agreement with the most recent x-ray photoelectron spectroscopy results of 42.3 eV from A. Lebugle, W. Axelsson, R. Nyholm, and N. Mårtensson (unpublished).

[43]R. W. Bower and J. W. Mayer, Appl. Phys. Lett. 20, 359 (1972); J. W. Mayer and K. N. Tu, J. Vac. Sci. Technol. 11, 86 (1974).

[44]See A. Franciosi and J. H. Weaver, Phys. Rev. B 27, 3554 (1983), and detailed references therein.

[45]K. Oura, S. Okada, and T. Hanawa, in Proceedings of the 8th International Vacuum Congress, Cannes (France), 1980, edited by F. Abeles and M. Croset [Suppl. à la Revue Le Vide. Les Couches Minces 201, 181 (1981)].

PHYSICAL REVIEW B VOLUME 29, NUMBER 6 15 MARCH 1984

Bonding in metal disilicides $CaSi_2$ through $NiSi_2$: Experiment and theory

J. H. Weaver and A. Franciosi
Department of Chemical Engineering and Materials Science, University of Minnesota, Minneapolis, Minnesota 55455

V. L. Moruzzi
IBM Thomas J. Watson Research Center, Yorktown Heights, New York 10598

(Received 20 October 1983)

Synchrotron radiation photoemission experiments with the disilicides of Ti, V, Nb, Cr, Fe, Co, and Ni are combined with self-consistent augmented-spherical-wave calculations of the density of states for metal silicides from Ca-Si to Cu-Si. These results demonstrate the importance of silicon p—metal d bond formation extending to ~ 6 eV below E_F for all transition metals. Experiment and theory are combined to show the movement of the nonbonding d states from above E_F for Ca-Si to well below E_F for Cu-Si. At the same time, the antibonding Si p and Si s states are shown to be relatively insensitive to the particular metal atom in the silicide series.

INTRODUCTION

The transition-metal silicides have properties which make them scientifically interesting and, at the same time, extremely important for the microelectronics industry. Many of them are chemically stable and resistant to corrosion or degradation, some form at relatively low temperature and have high electrical conductance,[1,2] others show promise as interface diffusion barriers,[3] and an increasing number of silicides are finding application in very-large-scale integrated (VLSI) circuit technology. Substantial efforts are now underway to understand the electronic properties of silicides and silicide-silicon junctions.[4–7]

We have undertaken a series of experimental and theoretical studies to delineate the role of the Si s, the Si p, and the metal d states in bonding and band-structure properties of a variety of transition-metal silicides.[8–12] This is part of a broader study which seeks insight not only about the bulk silicides but also about the electronic and structural evolution of metal-silicon interfaces.[12–15] In this paper, we present angle-integrated synchrotron radiation photoemission results for the bulk disilicides $TiSi_2$, VSi_2, $NbSi_2$, $CrSi_2$, $FeSi_2$, $CoSi_2$, and $NiSi_2$. Self-consistent augmented-spherical-wave (ASW) calculations performed for model metal-silicon compounds in the high-symmetry CuAu and Cu_3Au structures allow us to model the density of states for disilicides for comparison with experiment. These results reveal the dependence of the band structure on d-band occupancy and they demonstrate the common characteristics of transition-metal silicides, including the nonbonding d states near E_F, the p-d hybridized states extending to ~ 6 eV below E_F, and the Si s states 10—14 eV below E_F. For $CoSi_2$ and $NiSi_2$, which exhibit the CaF_2 structure, results from several different calculations are compared with experiment.

It should be pointed out that some of the silicides discussed herein have been examined by other authors, and Gelatt, Williams, and Moruzzi[8] have reported detailed theoretical studies of bonding between 4d transition metals and the non-transition-metal elements Li through F. Many of the observations regarding the p-d bond are therefore common to this excellent previous work. The point of this paper is to present a systematic study of bonding valid for all of the metal silicides, including the alkaline-earth and near-noble-metal silicides.

EXPERIMENTAL AND THEORETICAL TECHNIQUES

Buttons of the disilicides of Ti, V, Nb, Cr, Fe, Co, and Ni were initially prepared by arc melting high-purity constituents in a nonconsumable arc furnace on a water-cooled copper hearth. The success and ease of this process varied from silicide to silicide but the resulting 50-g samples were generally solid and homogeneous and further processing was limited to annealing to promote grain growth.[16] In particular, this arc-melting procedure was very satisfactory for $TiSi_2$, VSi_2, $NbSi_2$, $CrSi_2$, and $CoSi_2$ because they formed congruently from the melt. The disilicide $NiSi_2$ forms peritectically and the reaction was completed by annealing at 940 °C for six days. $FeSi_2$ is reported to form congruently at 1220 °C, but this alloy was also heat treated for homogenization at 940 °C for 13 days. For $CrSi_2$, the initial arc melting was followed by float-zone melting to ensure uniform composition.

Samples of these silicides were prepared for synchrotron radiation photoemission studies by fracturing precut posts *in situ* in the spectrometer at operating pressures of $\sim 5\times 10^{-11}$ Torr. Radiation from the Tantalus 240-MeV electron storage ring was used for studies in the range $10 \leq h\nu \leq 140$ eV (Grasshopper or toroidal grating monochromators). Photoelectron energy analysis was done with a commercial double-pass electron energy analyzer. The overall resolution of the experimental features varied from ~ 0.35 eV, depending on the photon energy. The results presented here are representative of stoichiometric-metal disilicides because the samples were fractured *in situ*. Effects due to segregation at the surface of silicides thermally grown on silicon or surface enrichment of one component due to preferential sputtering are thus avoided. At

the same time, such effects are interesting because of their importance in interface phenomena, and comparison with our spectra is informative.[11,12]

The experimental energy distribution curves (EDC's) shown in this paper have been scaled to give an approximately constant height for the dominant feature. At the same time, absolute $h\nu$ dependences of the photoionization cross sections were determined through normalization of the emission intensity to the photon flux.

The phase diagram of silicides generally show a variety of stable phases. In the experimental phase of this study, we emphasize the disilicides, because the disilicide is the most common interface reaction product and because we sought systematics in bonding within a particular stoichiometry range. The structural complexity of silicides has, no doubt, hindered the development of detailed theoretical pictures of their electronic structures.[17] Few calculations have been attempted which are, at the same time, descriptive of the correct stoichiometry and crystal structure and are also self-consistent. The calculations presented here are based on the cubic CuAu and Cu_3Au structures. They show systematics in bonding as a function of stoichiometry and, more important for this paper, changes in the Si-derived and metal-derived states as the metal itself is varied across the 3*d* transition series. Site and angular momentum decomposed state densities derived from model calculations of this kind have been shown to adequately describe the general trends of chemical bonding between transition metals and non-transition metals. For example, the behavior of the *p-d* states as a function of stoichiometry and the estimates of charge transfer as derived from such calculations and from calculations using realistic silicide structures were found to be in remarkable agreement for Ni and Pd silicides.[18,19]

The energy-band calculations were based on the augmented-spherical-wave (ASW) procedure for the solution of the one-electron equations.[20] Exchange and correlation effects were treated in the local-density approximation. Self-consistency was pursued until the calculated electronic charges were unchanged to within 0.001 electrons within the Wigner-Seitz sphere. The calculations were parameter-free, the only *a priori* inputs being atomic number and crystal structure, and they correspond to theoretical equilibrium since the atomic spacing was systematically varied until the total energy was minimized.

GENERAL TRENDS IN SILICIDE BONDING

In Fig. 1, we show calculated densities of states (DOS's) for the 3*d* transition-metal monosilicides based on the

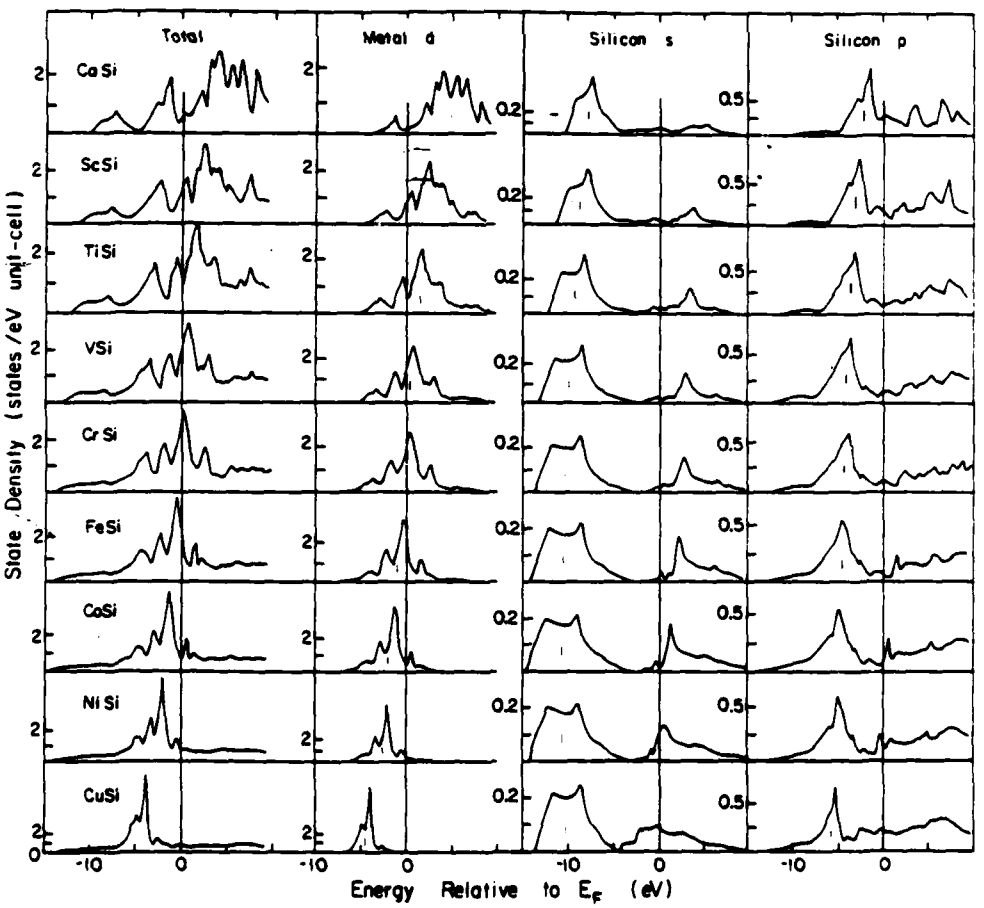

FIG. 1. Calculated total and partial state densities for monosilicides of Ca (top) through Cu (bottom) in the CuAu crystal structure. The scales are given alongside each curve. Tic marks guide the eye in observing systematics with increasing atomic number, including the movement of the *d* bands through the Si *p* bands.

CuAu structure. In Fig. 2, we show analogous results for the trisilicides ($CuAu_3$ structure). The total DOS is shown on the left of each figure, the *l*-projected metal *d* character is shown next, and these are followed by the projected silicon *s* and *p* character.

The results of Figs. 1 and 2 show how the *d* bands dominate the DOS and move through E_F with increasing Z, as indicated by tic marks at the center of the bands. This motion is relatively slow when the *d*-band density of states is high at E_F (near the middle of the transition series) but is faster at the extremes (near Ca-Si or Cu-Si). The metal *d*-derived states vary substantially within the series, appearing first as a broad band of mostly empty states for Ca-Si and ending with the narrow, fully occupied *d* band for Cu-Si. It is important to note that these results always show *d* character well below E_F—even for Ca which has s^2d^0 electronic configuration in the atom. This *d* character results from the lowering in energy of metal-derived 3*d* states that hybridize with Si-derived 3*p* states. The resulting *p-d* bonding combinations determine the stability of the silicide, while the corresponding antibonding combinations appear mostly above E_F.

The Si *p*—derived states are clustered into two energy regions straddling the Fermi level, with the occupied or bonding region being better defined than the empty states. As the atomic number of the metal atom is increased from Ca-Si to Cu-Si, the center of the occupied cluster moves to greater binding energy but the empty feature stays relatively fixed ~ 5 eV above E_F. This is indicated by the tic marks in the figures and is best seen for the trisilicides. The movement of the bonding states follows the shift of the metal *d* states to greater binding energy with increasing Z and is connected with the hybridization of silicon *p* orbitals with metal 3*d* states. The corresponding *p-d* antibonding combination above E_F appears nearly invariant in energy in the silicide series.

The *s*-derived states, which extend to ~ 15 eV below E_F, overlap relatively little with the *p* states of Si or the metal *d* states. The dominant structure represents an admixture of dominantly Si *s* and a slight amount of metal *s* character. For the monosilicides, this *s* band moves from -8 eV for CaSi to -10 eV for CuSi (see tic marks). For the trisilicides, it is almost stationary at -10 eV, except for $CaSi_3$ and $ScSi_3$. The empty *s* states, on the other hand, become prominent only after Sc-Si or Ti-Si, and the resulting structure ultimately shifts to near E_F.

The movement of the *d* bands through the Si *p* manifold in the silicide series substantially alters the overall density of states but has relatively little impact on the nature of the silicon *p*-metal *d* bonds. The calculations indi-

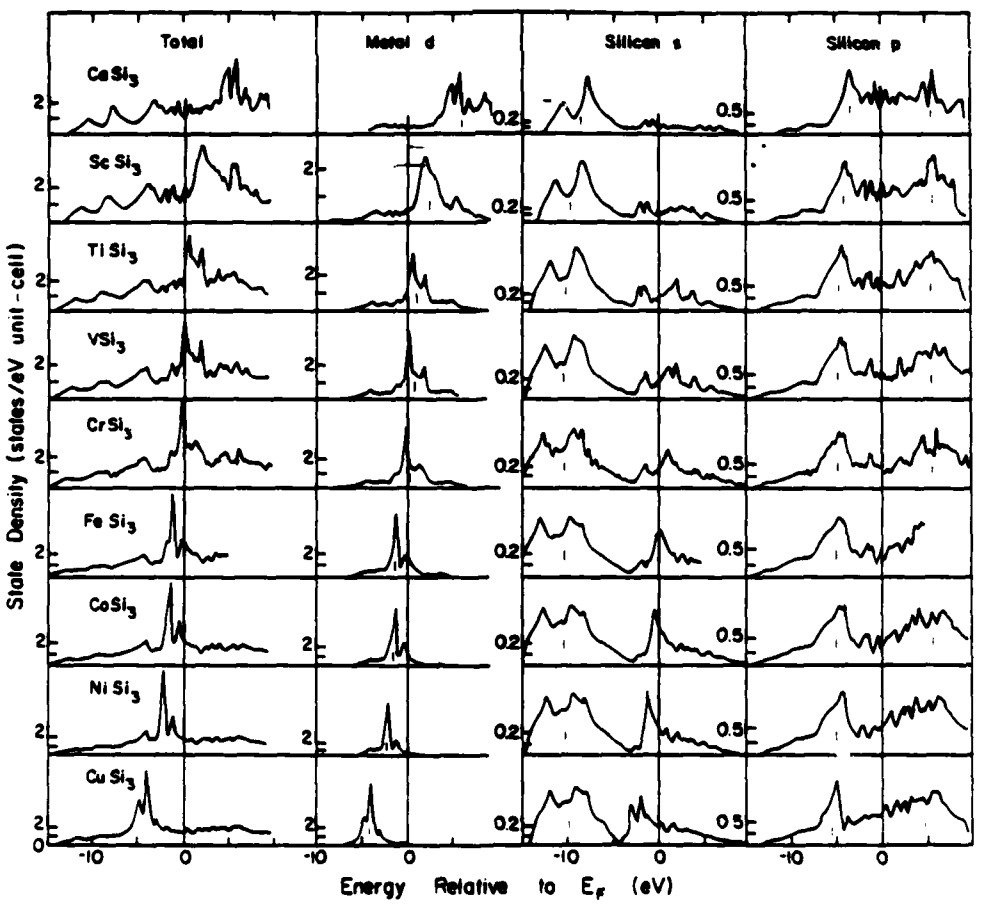

FIG. 2. Calculated total and partial state densities for the trisilicides of Ca (top) through Cu (bottom) analogous to those of Fig. 1 but with the $CuAu_3$ crystal structure.

cate that dominant silicon p—metal d coupling is present in all silicides, while the strength of such coupling varies with the relative position of the p and d states. In the trisilicide series, for example, p-d bonding combinations appear in the energy range 0.5—3.8 eV for $CaSi_3$ and involve virtually all the calculated d charge per metal atom. Moving along the 3d series, the shift and sharpening of the d bands yields p-d bonding states at 1.5—6 eV in $CrSi_3$ and 2.5—6.5 eV in $CoSi_3$, involving only about 50% of the calculated d charge per Cr atom in $CrSi_3$ and about 30% in $CoSi_3$. Correspondingly, the metal d states that are not directly coupled with Si p states form a cluster of nonbonding d states nearer E_F.

We emphasize that the systematics developed through Figs. 1 and 2 are based on isostructural calculations with hybridization of certain states allowed by group theory and forbidden to others. Calculations for different crystal structures will modify the details of the density of states. Nevertheless, we suggest that the bonding will always involve p-d hybridization and that these hybrid states will appear below the base of the nonhybridized states, in qualitative agreement with our results. This has been confirmed by recent calculations for VSi_2 (Ref. 21), $CrSi_2$, (Refs. 12 and 14), and $NiSi_2$ (Ref. 19) in their correct crystal structures.

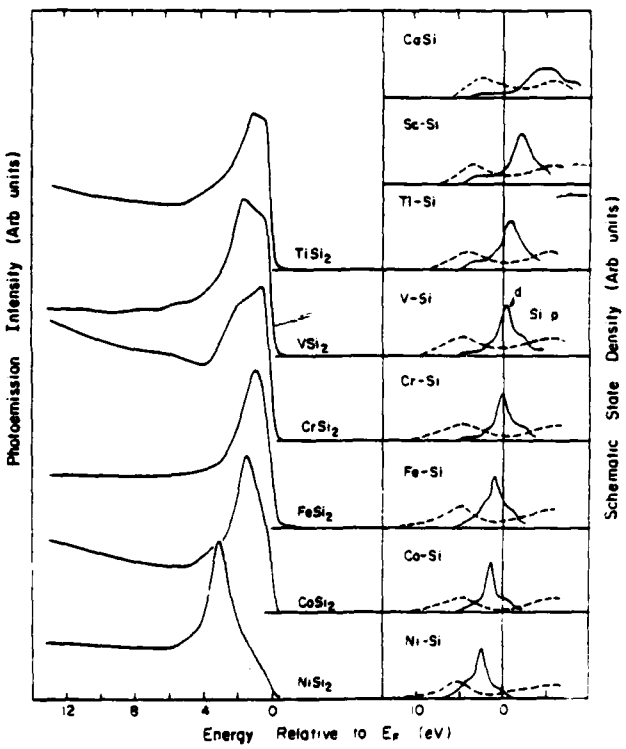

FIG. 3. Summary of experimental results (left) and interpolated state densities for the metal d (solid lines) and silicon p (dashed lines) states (right) for disilicides. Experiment verifies the existence of metal-silicon p-d bonding states extending to ~6 eV below E_F, as inferred from the calculations, and points to the common character of bonding in all transition-metal silicides. The dominant d emission near E_F corresponds to nonbonding states. Note that the results on the right are not scaled to true state densities.

COMPARISON OF EXPERIMENT AND THEORY

We see from the systematics of Figs. 1 and 2 that there are bonding d states below E_F for all these silicides. With increasing Z, the nonbonding d states sharpen, move through E_F, and, ultimately, even the antibonding states fall near E_F. To facilitate comparison of these predictions with our experimental results, we constructed qualitative DOS's for the disilicides based on results for the monosilicides and the trisilicides. To do this, we first broadened the monosilicides and trisilicides DOS features to retain only major features. These broadened DOS's were then compared and a *schematic* DOS was drawn which had the important points common to both but was, of course, insensitive to details. For example, the d character for CaSi was shown to extend ~4 eV below E_F with a broad cluster of states centered ~4.5 eV above E_F (width ~6 eV).

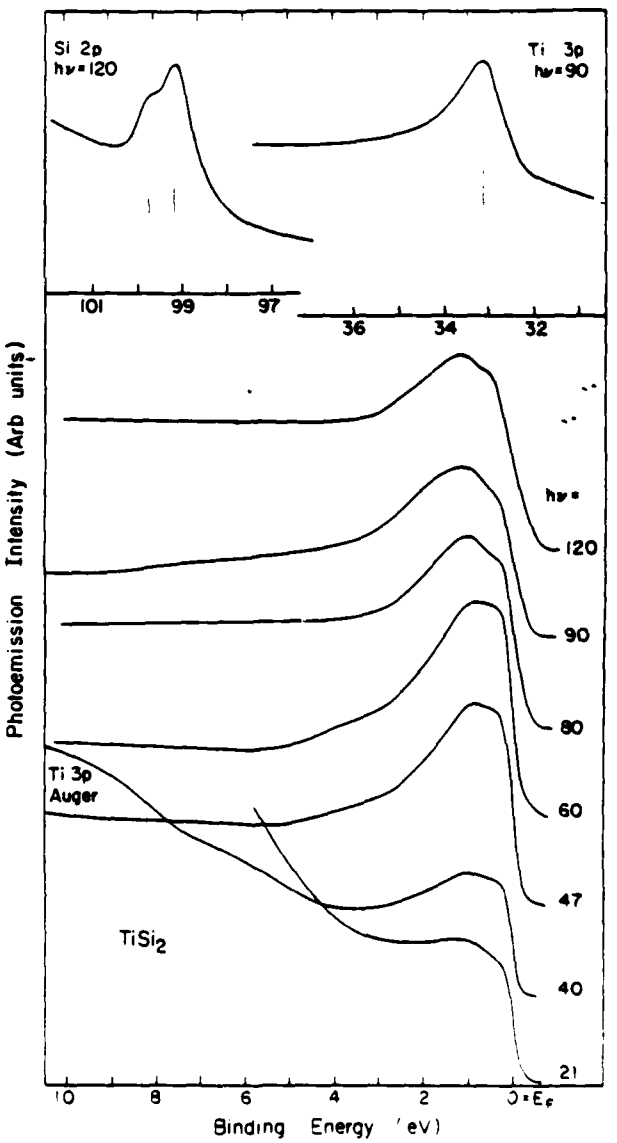

FIG. 4. Energy distribution curves (EDC's) for $TiSi_2$ for $21 \leq h\nu \leq 120$ eV. Emission from the Si 2p and Ti 3p cores is shown at the top.

For $CaSi_3$, the d character extended ~ 5 eV below E_F and the empty d states were centered ~ 6 eV above E_F (width 5.5–6 eV). Interpolation to $CaSi_2$ would indicate d character extending ~ 4.5 eV below E_F and empty states centered ~ 5 eV above E_F (width ~ 6 eV). Analogous procedures were used for the silicon p density of states. Hence, on the right of Fig. 3 we show the schematic DOS's for $CaSi_2$ and for the other systems under examination, using dashed curves for the Si p DOS's and solid curves for the metal d DOS's. Note that these DOS's are sketched with arbitrary units and that the d character dominates, as seen for the quantitative results of Figs. 1 and 2.

The interpolated p and d DOS's of Fig. 3 show that the d bands gather and disperse through E_F with increasing d occupancy, culminating in nearly filled d bands for $NiSi_2$. These interpolations predict clustered silicon p character ~ 5 eV below E_F. Hence, they preserve the most important aspect of the metal-silicon bond, namely, the p-d character well below E_F. They also establish the movement of the nonbonding d's through E_F with increasing Z. (These interpolated bands for $NiSi_2$ predict a DOS d peak ~ 2.5 eV below E_F, compared to ~ 2.8 eV from the calculations of Bisi and Calandra,[19] ~ 3.5 eV from Tersoff and Hamann,[22] or 3.3 eV from Bylander, Kleinman, Rednick, and Grise,[23] as will be seen in Fig. 10.)

In Figs. 4–10, we show EDC's for valence band and core emission for $TiSi_2$ (Fig. 4), VSi_2 (Fig. 5),[8] $NbSi_2$ (Fig. 6), $CrSi_2$ (Fig. 7),[12] $FeSi_2$ (Fig. 8), $CoSi_2$ (Fig. 9), and $NiSi_2$ (Fig. 10).[9] For visual clarity, the valence spectra have been offset and normalized to approximately the same height. The EDC's for the metal $3p$ ($4p$ for Nb) and Si $2p$ core levels are shown in the topmost or lowest sections of the figures. Since most valence-band features in Figs. 4–10 do not exhibit major dependence on $h\nu$ in the range

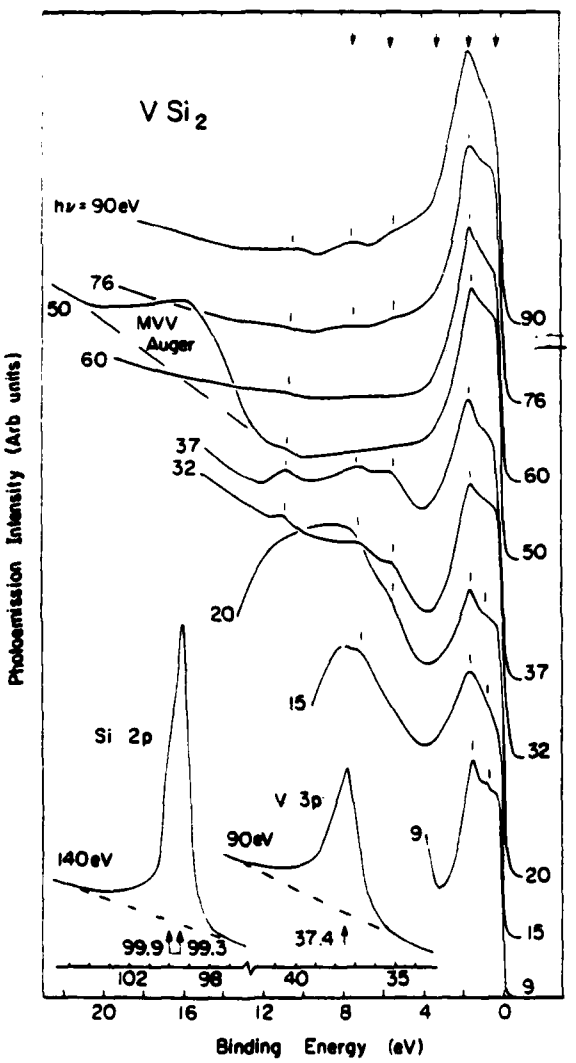

FIG. 5. EDC's for VSi_2 for $9 \leq h\nu \leq 90$ eV showing the $h\nu$ modulation of the initial states of nonbonding-d (near E_F), p-d hybrid (near 4 eV), p (near 6 eV), and s (near 10 eV) character.

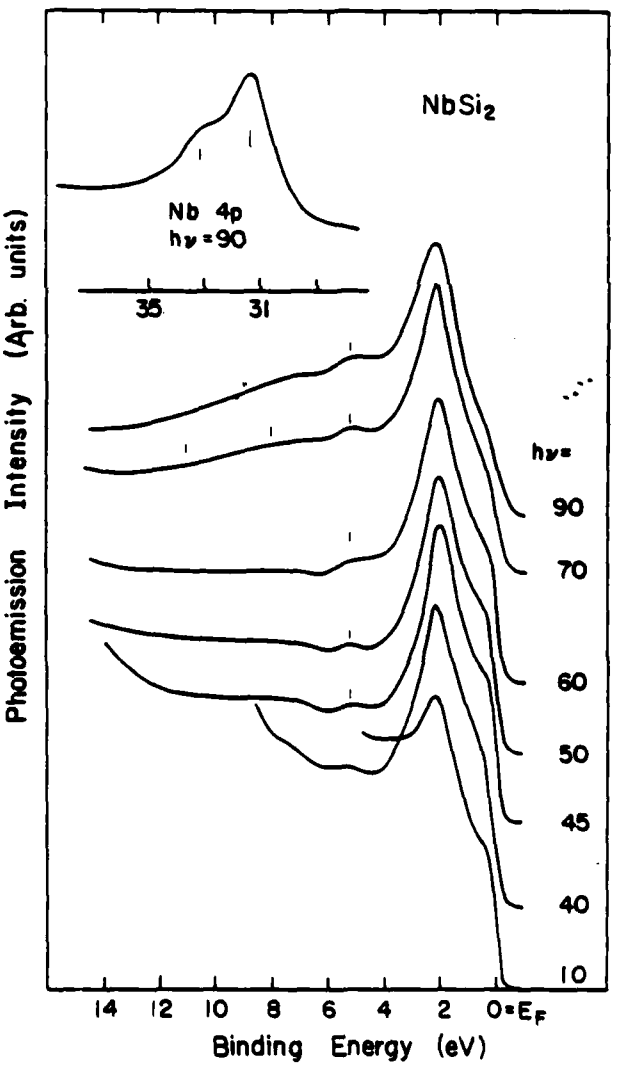

FIG. 6. EDC's for $NbSi_2$ in the photon energy range $10 \leq h\nu \leq 90$ eV for comparison to the $3d$ transition-metal disilicides. Emission from the Nb $4p$ cores is shown at the top. The valence-band spectra show s-, p-, p-d– and d-derived structures analogous to those for VSi_2.

$10 \leq h\nu \leq 120$ eV, we associated them with structure in the density of electronic states.

The spectra in Fig. 4 for $TiSi_2$ are dominated by intense emission within 3 eV of E_F (peak at 1–1.2 eV) and show a shoulder near 4 eV for $45 \leq h\nu \leq 65$ eV. At higher binding energies, emission above the secondary background is evident but it is without discernible structure. (Auger LVV emission appears near 9 eV in the 40-eV EDC.) For Ti-Si most of the d charge per atom is directly involved in the bonding with silicon and we associate the main spectral features to metal-derived $3d$ states. The schematic DOS in Fig. 3 suggests that the character of these valence states will become increasingly bonding for higher binding energies with a parallel increase of the Si-derived character of the valence states. The states that account for the DOS features 4 eV below E_F exhibit strong p-d hybrid character.

The valence-band spectra for VSi_2 in Fig. 5 show structure at 1.6, 5.5, 7.2, and 10.4 eV. The relative intensity of the EDC features is modulated by the different photoionization cross sections of initial states of s, p, or d character. On the basis of the results of Figs. 1 and 2 and of Ref. 21, we associate the feature at 1.6 eV with metal-derived $3d$ states, the feature at 5.5 eV with hybrid p-d orbitals, and the structures at 7.2 and 10.4 eV with relatively pure Si-derived p and s character, respectively. These identifications can be confirmed by a quantitative comparison of the cross section for the various initial states. Resonant photoemission at the $3p \rightarrow 3d$ excitation energy, in particular, has already been used for Pd_2Si (Ref. 10) to confirm the character of the different valence states. In the following section, we will apply this technique to VSi_2 as a test case for our systematic analysis of the disilicide valence states.

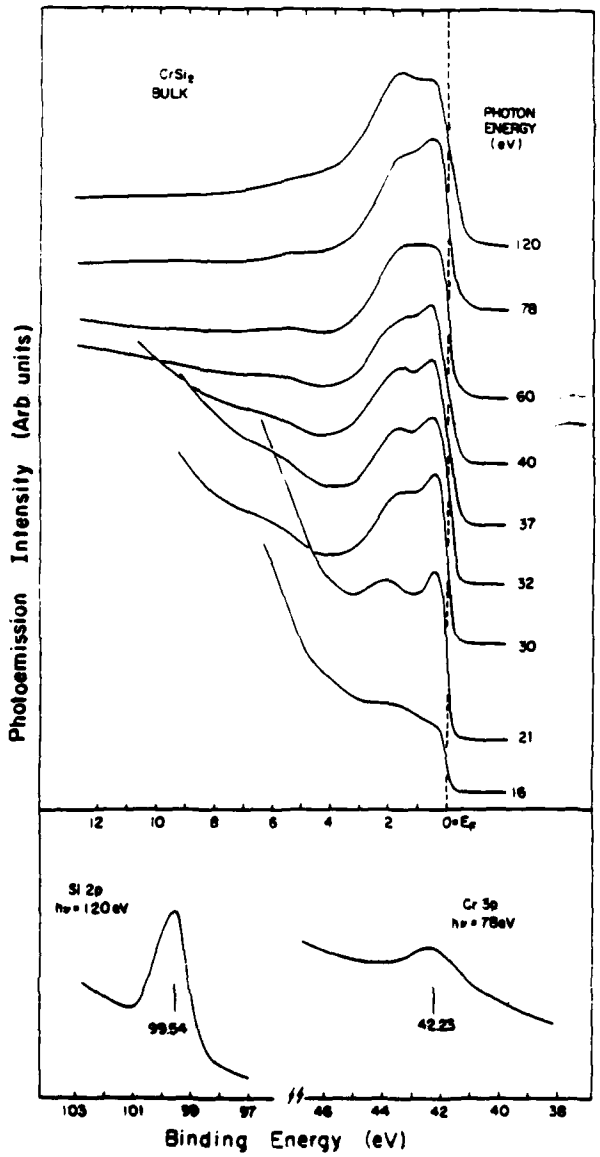

FIG. 7. EDC's for valence bands of $CrSi_2$ for $16 \leq h\nu \leq 120$ eV. Emission from the Si $2p$ and Cr $3p$ cores is shown in the lowest part of the figure (from Ref. 12).

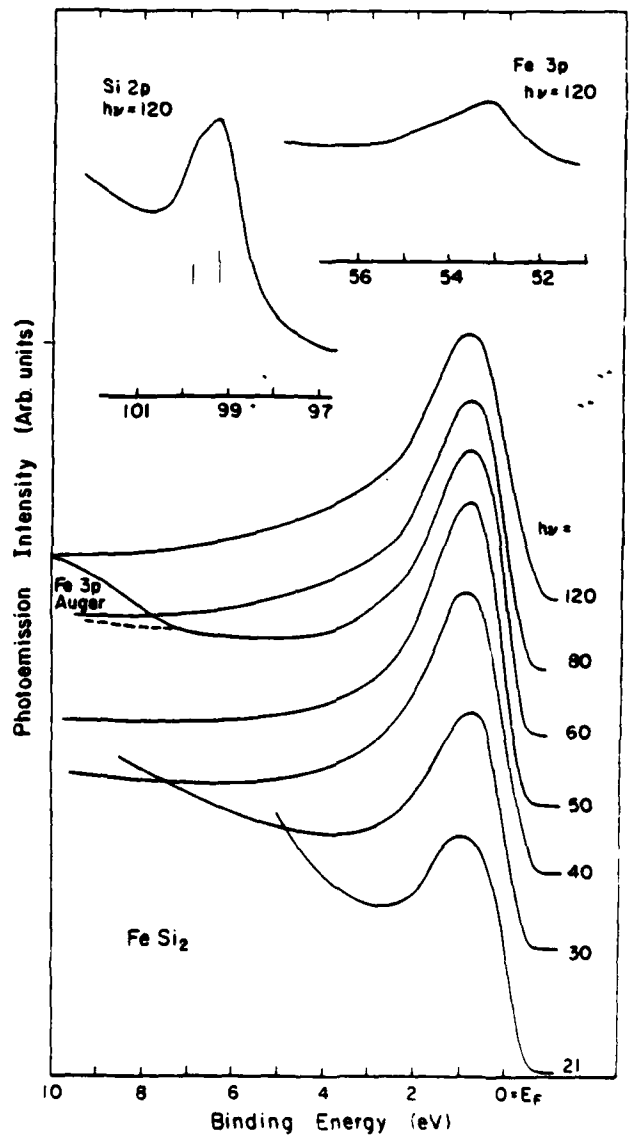

FIG. 8. EDC's for the valence bands of $FeSi_2$ for $21 \leq h\nu \leq 120$ eV. Emission from the Si $2p$ and Fe $3p$ cores is shown at the top.

In Fig. 6, we show EDC's for $NbSi_2$ for $10 \leq h\nu \leq 90$ eV. These, and results for $MoSi_2$,[8] provide a comparison for the $3d$ and $4d$ isoelectronic transition-metal disilicides. From them, we see that there are analogous spectral features for $NbSi_2$ and VSi_2 with slightly shifted binding energies (5.2, 8, and 11 eV for $NbSi_2$). The deepest can be related to the Si s-derived states and the two at 5.2 and 8 eV represent primarily p-derived features with substantial mixture of d character in the region of $\sim$4—6 eV. Further, these results show that the d-derived structure within $\sim$4 eV of E_F is wider for $NbSi_2$ than for VSi_2 because of the inherently wider d bands. This d-derived structure closely resembles that of $MoSi_2$ and the $5d$ transition-metal silicide $TaSi_2$.[8]

Valence-band and core data for $CrSi_2$ appear in Fig. 7 (from Ref. 12). The corresponding calculations in Figs. 1—3 indicate that the d bands for $CrSi_2$ are approximately half filled and that they draw away from E_F as they become nearly filled. Indeed, for $NiSi_2$ the d bands are predicted to be $\sim$3—6 eV below E_F. The effect of the d-band filling can be seen by examining the $CrSi_2$, $FeSi_2$, $CoSi_2$, and $NiSi_2$ silicide series (Figs. 3 and 7—10). The EDC's for $CrSi_2$ indicate strong emission near E_F (0.6 eV), structure near -2 eV, and a shoulder at -6 eV. The EDC's for $FeSi_2$ show less structure (peak at about 0.75 eV and broad, structureless emission extending to about -10 eV). EDC's for $CoSi_2$, on the other hand, show the dominant d-derived feature to have drawn away from E_F, as predicted by the interpolated DOS results of Fig. 3 (peak at 1.4—1.5 eV and shoulder at $\sim$3.8 eV below E_F). Results for $NiSi_2$, shown in Fig. 10 for $h\nu = 40$ and 50 eV, are very similar to those for $CoSi_2$ except that the location of E_F is higher within the valence bands, the d bands are almost completely filled, and the separation of the nonbonding and bonding states is reduced.

These various results can be understood on the basis of the systematics of the schematic DOS of Fig. 3, taking into account the empirical observation that photoemission spectra for $10 \leq h\nu \leq 120$ eV emphasize nonbonding $3d$ states over the hybrid p-d orbitals. This can be seen, for example, by comparing the $NiSi_2$ calculations of Fig. 10 with experimental results or comparing our synchrotron radiation results[9] with XPS (x-ray photoelectron spectroscopy) results by Grunthaner, Madjukar, and Mayer for Ni_2Si.[7] In our EDC's the DOS structures 3—3.5 eV below E_F for $NiSi_2$ (2 eV for $CoSi_2$) dominate the spectra but the 5-eV feature (4 eV for $CoSi_2$) is much weaker than in the XPS results and in the calculations. Bearing this in mind, the experimental emission feature at 0.6 eV for $CrSi_2$ can be associated with nonbonding metal $3d$ states, while emission at 2.0 eV and below should come from bonding p-d orbitals. The shoulder at 6 eV corresponds to DOS features of substantial Si $-p$ character. Similarly, for $FeSi_2$, where a large fraction of the metal $3d$ charge is not coupled with Si-derived states, the main emission features within $\sim$2 eV of E_F reflect nonbonding metal d states, while the broad shoulder $\sim$5 eV below E_F exhibits mixed p-d character.

$CoSi_2$ is near the end of the $3d$ row where the nonbond-

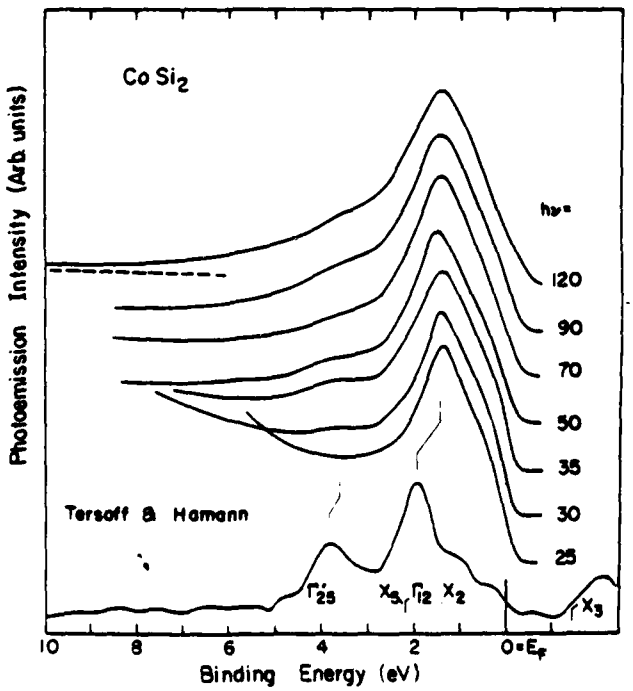

FIG. 9. EDC's for the valence bands of $CoSi_2$ in the photon energy range $25 \leq h\nu \leq 120$ eV compared to the total density of states calculated by Tersoff and Hamann (Ref. 22).

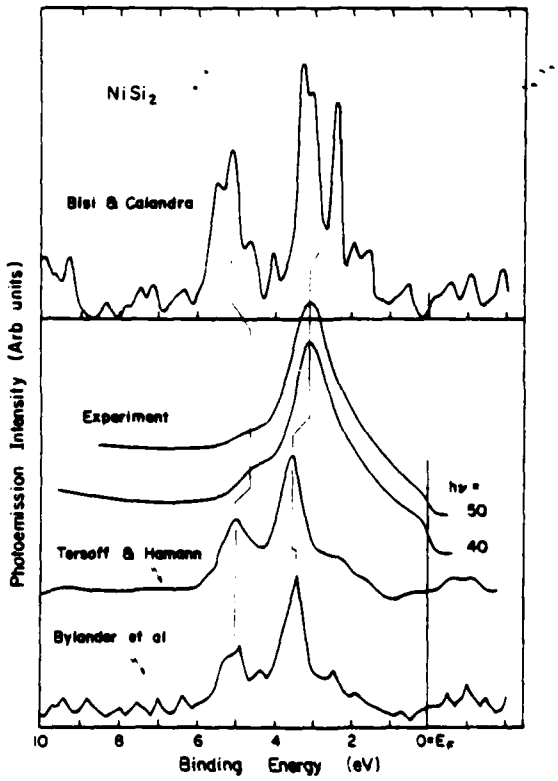

FIG. 10. EDC's for the valence bands of $NiSi_2$ for $h\nu = 40$ and 50 eV (from Ref. 9). For comparison we show that total density of states calculated by Bisi and Calandra (Ref. 19) (top), Tersoff and Hamann (Ref. 22), and Bylander, Kleinman, Mednick, and Grise (Ref. 23) (bottom).

ing d states form a sharp, dominant emission feature at 1.45 eV and the bonding d states appear as a relatively weak structure at about 2-eV higher binding energy. In Fig. 9 we show the experimental results for $CoSi_2$ and compare them to the calculated density of states of Tersoff and Hamann.[22] Inspection shows quite good agreement but indicates that the calculations overestimate the binding energy of the experimental feature by 0.3–0.5 eV.

$NiSi_2$ is probably the most studied silicide both from the experimental and theoretical points of view. Angle-integrated and angle-resolved photoemission investigations of its electronic structure have recently been reported by ourselves,[9] Chang and Erskine, and Chabal, Hamann, Rowe, and Schlüter.[24] In Fig. 10 we summarize the angle-integrated results[9] and compare them to the densities of states calculated by Tersoff and Hamann,[22] Bisi and Calandra,[19] and Bylander, Kleinman, Mednick, and Grise.[23] As shown, there is good overall quantitative agreement with experiment and the different sets of calculations yield very similar densities of electronic states, although the details of the bonding vary from author to author (charge transfer and ionic contribution to the bond, electronic configuration at equilibrium for the metal and Si atoms).

RESONANT PHOTOEMISSION

Identification of the character of the valence states can be supported by quantitative analysis of the cross sections of the various initial states. To do this, we show in Fig. 5 a series of EDC's for VSi_2 and the results of analysis of the peak heights as a function of photon energy in Fig. 11. VSi_2 was chosen because several structures could be resolved in the valence bands, including features at 1.6 eV (a derived), 5.5 eV (p-d), 7.2 eV (p), and 10.4 eV (s derived). Emission from the Si-derived s and p states is low for $h\nu \simeq 50$–60 eV but then increases at higher energy. The d bands, on the other hand, are always prominent, but this is partially an artifact of normalization of the spectra of Fig. 5.

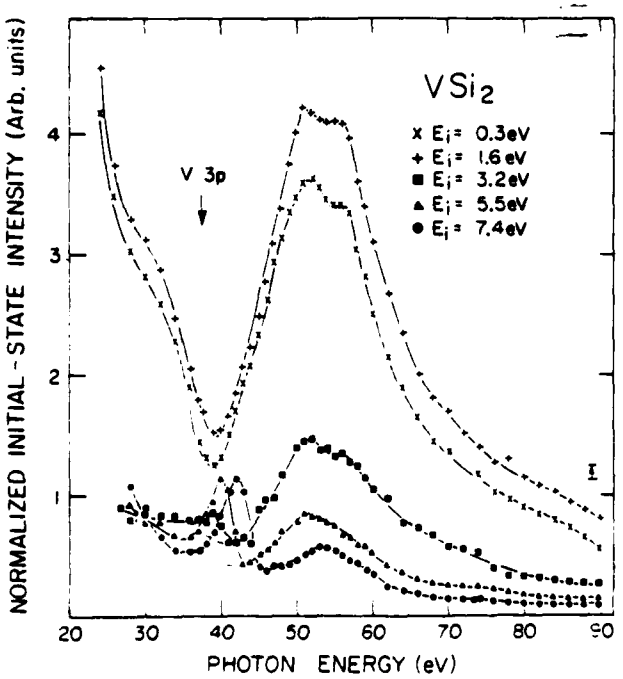

FIG. 11. Photoionization cross sections for VSi_2 corresponding to initial states marked by arrows in Fig. 5. As a result of $3p$-$3d$ resonance, the spectra show a threefold enhancement of the nonbonding d states. For the p-d hybrid states, the magnitude of the enhancement depends on the degree of hybridization and decreases for increasing Si p contribution.

Partial photoionization cross sections were determined from the spectra of Fig. 5 and others for $9 \leq h\nu \leq 90$ eV measured at increments of 1 or 2 eV. These are shown in Fig. 11 for initial states at 0.3, 1.6, 3.2, 5.5, and 7.4 eV (see arrows in Fig. 5). Clear enhancement of these states (and the entire band) for $h\nu \geq 38$ eV is associated with the excitation of the V $3p$ core ($E_B = 37.4$ eV). For $E_i = 0.3$ and 1.6 eV, the emission decreases for $20 \leq h\nu \leq 40$ eV but is then enhanced approximately threefold between ~ 38 and ~ 50 eV. For states in the p-d bonding region, the enhancement is weaker but the shape is approximately the same for $h\nu > 38$ eV. States with increased Si-derived character exhibit considerably less enhancement. (The structure that appears around $h\nu = 40$ eV is due to overlapping Auger emission.)

Resonant valence-band enhancement has been observed in other silicide systems[10] and is analogous to d-f enhancement studied in lanthanides and actinides.[25] This resonance reflects the quantum-mechanical equivalence of different paths leading from the ground state to the final state where an emitted electron is in the continuum. The two paths are direct valence-band emission $3p^6(4sd)^n + h\nu \rightarrow 3p^6(4sd)^{n-1} + e$ and a core-level-involving process $3p^6(4sd)^n + h\nu \rightarrow 3p^5(4sd)^{n+1} \rightarrow 3p^6(4sd)^{n-1} + e$. The strength of the enhancement is a measure of the overlap of the p-core hole and the d-valence state. Hence, as the d states become hybridized the overlap is reduced and the enhancement diminishes. The importance of this phenomenon to us here is that it can be used to highlight d emission in the photon energy range near the p-core-level excitation energy. The results for VSi_2 (as for Pd_2Si in Ref. 10) clearly show the different character of Si- and metal-derived states and they support the identification of the spectral feature as $3d$ derived, with mainly nonbonding character at E_F and increasing p-d hybrid character for increasing binding energy in the energy range 2–6 eV.

Cross-section analyses for $MoSi_2$ similar to those for VSi_2 show similar, but smaller, enhancement for $4p$-$4d$ interaction as for $3p$-$3d$. Analogous studies for ScH_2, YH_2, LaH_2, and ThH_2 (Ref. 26) indicate reduced enhancement for increasing principal quantum number n in np-nd resonance. This is due, in part, to the increasing delocalization of the d wave function.

CONCLUSIONS

In this paper we have given experimental and theoretical insight into bonding systematics for the metal disilicides over the full range of the $3d$ transition metals. The systematics indicate the following:

(1) The states which we see as dominant in synchrotron radiation photoemission are generally nonbonding $3d$ states since they overlap very little with Si-derived states. The results for the disilicides of Ti through Co all show important d character within 3 eV of E_F (lower for Ni). Hence, the electrical properties of silicides will be determined by d states.

(2) Silicon p—metal d mixing is important for all silicides and lowers metal d states to well below E_F. Our experimental observation of bonding mixtures of p-d states supports the model that p-d bonding states will generally account for the silicide stability. Detailed calculations of the future must consider the specifics of the p-d hybridization—this must vary with stoichiometry, crystal structure, and possibly nonequivalent sites (see, for example, the calculation of Switendick[27] for Fe_3Si).

(3) The detection of the Si s-derived states has, so far, been limited to the disilicides of V, Nb, Mo, Ta, and Ce. (Parks, Reihl, Martensson, and Steglich[28] have observed the onset of the Si s band near 12 eV for $CePd_2Si_2$ and $CeAu_2Si_2$.) For the other disilicides, we observe only an unstructured tailing off of valence-band emission near 10—12 eV. The invariance of this feature indicates that the Si s character is relatively unimportant in bonding.

We anticipate that these results can be generally interpolated to the monosilicides [e.g., MnSi and NiSi (Ref. 9)] and the metal-rich silicides [Fe_3Si, Ni_2Si (Ref. 9), Pd_2Si (Ref. 10)]. They will most likely find substantial validity for the germanides as well.

ACKNOWLEDGMENTS

It is a pleasure to acknowledge the staff of the Synchrotron Radiation Center of the University of Wisconsin, where the photoemission experiments were conducted, and the Materials Preparation Center of the Ames Laboratory, where the samples were prepared. Discussion with Dr. Tersoff, Dr. Kleinman, and Dr. Bisi are gratefully acknowledged. This work was supported by U. S. Army Research Office Contract No. ARO-DAAG-29-83-K-0061.

[1]K. N. Tu, in *Thin Films—Interdiffusion and Reactions*, edited by J. M. Poate, K. N. Tu, and J. W. Mayer (Wiley, New York, 1980).

[2]S. P. Murarka, J. Vac. Sci. Technol. 17, 775 (1980); G. Ottaviani, *ibid.* 18, 924 (1981).

[3]A. Franciosi, J. H. Weaver, and D. G. O'Neill, Phys. Rev. B 28, 4889 (1983).

[4]For an extensive review, see L. J. Brillson, Surf. Sci. Rep. 2, 123 (1982), and G. Margaritondo, Solid State Electron. 26, 499 (1983).

[5]L. Braicovich, I. Abbati, J. N. Miller, I. Lindau, S. Schwarz, P. R. Skeath, C. Y. Su, and W. E. Spicer, J. Vac. Sci. Technol. 17, 1005 (1980); I. Abbati, L. Braicovich, and B. De Michelis, Solid State Commun. 36, 145 (1980).

[6]J. L. Freeouf, G. W. Rubloff, P. S. Ho, and T. S. Kuan, Phys. Rev. Lett. 43, 1836 (1979); P. S. Ho, P. E. Schmid, and H. Foll, *ibid.* 46, 782 (1981).

[7]P. J. Grunthaner, F. J. Grunthaner, A. Madhukar, and J. W. Mayer, J. Vac. Sci. Technol. 19, 649 (1981); N. W. Cheung, P. J. Grunthaner, F. J. Grunthaner, J. W. Mayer, and B. M. Ullrich, *ibid.* 18, 917 (1981).

[8]J. H. Weaver, V. L. Moruzzi, and F. A. Schmidt, Phys. Rev. B 23, 2916 (1981) for VSi_2, $TaSi_2$, and $MoSi_2$. C. D. Gelatt, A. R. Williams, and V. L. Moruzzi [*ibid.* 27, 2005 (1983)] discussed bonding of $4d$ transition metals to the non-transition-metal elements Li through F and revealed how bonding changes when the s and p bands fall above, below, or near the d-band resonance.

[9]A. Franciosi, J. H. Weaver, and F. A. Schmidt, Phys. Rev. B 26, 546 (1982) for Ni_2Si, NiSi, and $NiSi_2$.

[10]A. Franciosi and J. H. Weaver, Phys. Rev. B 27, 3554 (1983) for Pd_2Si.

[11]A. Franciosi and J. H. Weaver [Physica (Utrecht) 117B-118B, 846 (1983), and Surf. Sci. 132, 324 (1983)] summarize results for a number of bulk and interface silicides.

[12]A. Franciosi, J. H. Weaver, D. G. O'Neill, F. A. Schmidt, O. Bisi, and C. Calandra [Phys. Rev. B 28, 7000 (1983)] present results for bulk and interface $CrSi_2$.

[13]A. Franciosi, D. J. Peterman, J. H. Weaver, and V. L. Moruzzi, Phys. Rev. B 25, 4981 (1982) for the Si(111)-Cr interface.

[14]A. Franciosi, J. H. Weaver, D. G. O'Neill, Y. Chabal, J. E. Rowe, J. M. Poate, O. Bisi, and C. Calandra, J. Vac. Sci. Technol. 21, 624 (1982) for the Si-Cr and Si-Ni interfaces.

[15]A. Franciosi, J. H. Weaver, P. Perfetti, A. D. Katnani, and G. Margaritondo, Solid State Commun. 47, 427 (1983) for the Si-Sm interface; A. Franciosi, J. H. Weaver, and D. T. Peterson (unpublished) for Si(111)-Ca.

[16]Visual examination of the microstructure showed $\lesssim 5\%$ intragranular second phase to be present for $FeSi_2$ and $CrSi_2$; this was confirmed by chemical analysis and x-ray analysis which indicated slightly silicon-rich average compositions.

[17]The crystal structure of these silicides include the $CrSi_2$ $C40$ structure ($CrSi_2$, VSi_2, $NbSi_2$), the hexagonal $TiSi_2$ $C54$ structure ($TiSi_2$), the hexagonal $MoSi_2$ $C11b$ structure ($MoSi_2$), the $FeSi_2$ structure ($FeSi_2$), and the CaF_2 $C1$ structure ($CoSi_2$, $NiSi_2$). These $MoSi_2$, $CrSi_2$, and $TiSi_2$ structures are all built up from close-packed layers and they differ only in their stacking sequences with stacking arrangement such that atoms have only two close neighbors in adjacent layers (10 nearest neighbors).

[18]P. S. Ho, G. W. Rubloff, J. E. Lewis, V. L. Moruzzi, and A. R. Williams, Phys. Rev. B 22, 4784 (1980).

[19]O. Bisi and C. Calandra, J. Phys. C 14, 5479 (1981).

[20]The ASW method as developed by A. R. Williams, J. Kubler, and C. D. Gelatt [Phys. Rev. B 19, 6094 (1979)] is the spherical wave analog of Slater's augmented-plane-wave (APW) method and is closely related to Andersen's linear combination of muffin-tin orbitals (LMTO) method; see, for example,

O. K. Andersen, *ibid.* 12, 3060 (1975).
[21]O. Bisi and L. W. Chiao, Phys. Rev. B 25, 4943 (1982).
[22]J. Tersoff and D. R. Hamann, Phys. Rev. B 28, 1168 (1983).
[23]D. M. Bylander, L. Kleinman, K. Mednick, and W. R. Grise, Phys. Rev. B 26, 6379 (1982).
[24]Yu-Jeng Chang and J. L. Erskine, Phys. Rev. B 26, 4766 (1982); Y. J. Chabal, D. R. Hamann, J. E. Rowe, and M. Schlüter, Phys. Rev. B 25, 7598 (1982).
[25]See, for example, D. J. Peterman, J. H. Weaver, M. Croft, and D. T. Peterson, Phys. Rev. B 27, 808 (1983), and detailed references therein on resonant photoemission.
[26]J. H. Weaver (unpublished).
[27]A. C. Switendick, Solid State Commun. 19, 511 (1976).
[28]R. D. Parks, B. Reihl, N. Martensson, and F. Steglich, Phys. Rev. B 27, 6052 (1983).

Cluster-Induced Reactions at a Metal-Semiconductor Interface: Ce/Si(111)

M.Grioni, J.Joyce[@], S.A. Chambers[*], D.G. O'Neill[@],

M. del Giudice, and J.H.Weaver

Department of Chemical Engineering and Materials Science

University of Minnesota, Minneapolis, MN 55455

Abstract

Synchrotron radiation photoemission, angle-resolved Auger, and LEED studies show Ce cluster formation on Si(111). These nonmetallic clusters grow for coverages 0.1 to 0.6 ml, interact weakly with the substrate, and induce 200 meV band bending changes. At ~0.6 ml, they stimulate surface disruption, producing a metallic interfacial silicide. The association of d- or f-band metal clusters with surface reaction substantially extends the cluster-induced-reaction model proposed for Al/GaAs.

PACS: 73.40.+y
73.40.-c
73.40.Ns
79.60.Gs

Microscopic examinations of evolving metal/semiconductor interfaces have revealed several systems that react only when the metal coverage, Θ, exceeds a critical coverage, Θ_c.[1-10] Modeling of these interfaces requires an understanding of the triggering phenomenon. Despite considerable efforts, however, the mechanism remains elusive.

Zunger[11] has suggested that cluster formation can induce defects at the Al/GaAs(110) interface. His total energy calculations stressed adatom-adatom interaction through clustering, a point of view which differs from those which stress metal/substrate bonding.[12,15] In light of the significance of this cluster mechanism, we sought a metal/semiconductor system in which the onset of chemical reaction could be linked to the ripening of clusters.

In this paper, we describe the room temperature evolution of Ce clusters on Si(111)-2x1 and 7x7 surfaces. High resolution synchrotron radiation photoemission, angle-resolved Auger spectroscopy (ARAS),[16] and LEED measurements show changes in both electronic structure and morphology. Indeed, this combination of techniques should make it possible to assess cluster formation for other interfaces and should reveal the relative importance of adatom/substrate and adatom/adatom bonding.

The photoemission experiments were performed at the Wisconsin Synchrotron Radiation Center using "Grasshopper" and toroidal grating monochromators for $12 < h\nu < 135$ eV. Photoelectrons were analyzed by a double pass CMA with overall energy resolution of between 200 meV ($h\nu$ = 40 eV) and 500 meV (135 eV). The ARAS studies used a single pass CMA with limited electron acceptance and a precision manipulator to vary the take-off angle from normal emission to grazing incidence. This detector was also used to obtain I-V LEED profiles along high symmetry lines.

Clean Si(111)-2x1 and 7x7 surfaces were produced by cleavage or standard Ar^+ sputtering and annealing. High purity cerium was evaporated at pressures better than $1x10^{-10}$ Torr; the thickness was monitored by an oscillating quartz crystal and the evaporation rate was ~1Å/min. Operating pressures in both spectrometers were $3\text{-}5x10^{-11}$ Torr.

To demonstrate the existence of a critical coverage corresponding to the onset of reaction, we show in Fig. 1 Si 2p core level spectra taken at $h\nu$=135 eV (escape depth ~4Å).[17] For clean Si(111)-2x1, the 2p doublet is broadened by the surface-shifted component.[17] Between zero and ~0.6 ml, there is a rigid shift of 200 meV due to variations in band bending (as confirmed by bulk sensitive spectra at $h\nu$=106 eV), but the unvarying lineshape indicates minimal Ce-substrate interaction. Analysis of the Si-2p lineshape for θ>0.6 ml reveals a reacted Si species shifted 0.7 eV to lower binding energy. This component grows and is most pronounced near 3 ml and the substrate component attenuates rapidly (discussed elsewhere using integrated intensities of the different components[18]). From coverage studies with 0.06 ml increments between 0 and 1 ml, we conclude that θ_c≈0.6 ml.

LEED studies showed conversion from 2x1 or 7x7 patterns to 1x1 by ~0.4 ml but showed no metal-induced superstructure. The Si-1x1 pattern persisted through θ_c, although with increasing background. For 0.8 ml, where photoemission showed intermixing, LEED showed sufficient uncovered/unreacted Si for coherent diffraction (1x1 pattern). This indicates that the reaction could not be proceeding uniformly on the surface, and points to cluster-induced reaction. Even at 1.2 ml a 1x1 pattern, which was scarcely visible to the eye, could be detected by taking I-V measurements in high-symmetry azimuthal planes perpendicular to the

surface. By 2 ml, the (10), (11), and (20) LEED beams were completely gone, indicating the total destruction of long range order.

Valence band studies at $h\nu$=35 and 60 eV were undertaken to examine the electronic states at low coverage. Changes induced by d-derived states were readily seen at 35 eV; comparison of results for $h\nu$=35 and 60 eV showed the emergence of Ce 4f emission.[19,20] As shown in Fig. 2, the Ce-derived emission at -3.3 and -1.2 eV for $0.1<\theta<0.6$ ml rapidly overwhelms Si-emission and, with increasing coverage, the feature at -1.2 eV grows in relative intensity. Simultaneously, the FWHM measured at $h\nu$=35 eV diminishes from ~4.4 eV for θ=0.2 ml to 3.9 eV for θ=0.4 ml. Consistent with the core level results, we find that at θ=0.6 ml the valence band center shifts abruptly toward E_F by ~0.7 eV and broadens sufficiently to lose its prominent doublet character. The appearance of the Fermi-level cutoff indicates metallic character for the reacted phase.

The valence band results indicate cluster formation and growth for coverages 0-0.6 ml. Adatom-induced states are clearly visible but are shifted away from E_F, analogously to what has been observed in all photoemission studies of weakly interacting clusters on inert substrates.[21] The observed cluster bandwidth, which is substantially greater than that of bulk Ce,[19] suggests a large number of inequivalent atoms, as observed for metal clusters. The absence of a Fermi level for θ=0.6 ml indicates that the molecular cluster has not reached the metallic droplet limit.

Studies of Ce 4f emission probe the environment around the Ce atom as effectively as Si 2p emission reveals the Si environment. Modification of the Ce environment above θ_c can be seen through difference spectra obtained by subtracting valence band EDCs at 35 and 60 eV (Fig. 2). This procedure emphasizes the 4f character, as shown for α-Ce, γ-Ce,[19] and the Ce

pnictides.[20] Even for Ce coverages of 0.1 ml, a clearly-defined spectral feature can be associated with the Ce 4f at -3.3 eV. The changing 4f fingerprint can therefore be used to assess chemical reaction (4f final states screening will be discussed elsewhere).

Figure 2 shows that the 4f feature sharpens but does not shift with coverage below θ_c. At θ=0.8 ml its appearance is modified by a shoulder at 0.7 eV lower binding energy, and by 1.2 ml the 4f feature has fully shifted to the lower binding energy position. Comparison with results obtained from a bulk sample of $CeSi_2$ shows a silicide formation.

At the top of Fig. 3 we show Ce(N_4VV) and Si($L_{2,3}VV$) integrated Auger peak intensities measured at normal emission as a function of coverage. With increasing coverage, the Ce signal steadily increases while the Si signal is attenuated significantly from 0 to 0.4 ml. Between 0.4 and 0.8 ml, corresponding to the transition through θ_c, the Si attenuation is reduced. This behavior, which deviates from that expected for either ordered overlayers or an intermixed phase, can be explained by initial Ce coverage of a fraction of the substrate, followed by an intermediate region 0.4-0.8 ml, where two processes compete. Initially, cluster formation attenuates the substrate, but this is offset by Si intermixing once reaction starts. The reacted regions then spread laterally, consuming more of the surface and attenuating the Si emission.

Polar-angle profiles of the Ce and Si Auger intensities measured in the ($\bar{1}10$) azimuthal plane are shown in the lower two sections of Fig. 3. Structure in these polar profiles would reflect electrons scattering from near neighbor atoms and subsequent interference. For Ce, the results are featureless, consistent with disordered clusters. In contrast, the polar profile for clean Si shows diffraction modulation characteristic of the 7x7

surface, and this modulation remains in detail at 0.8 ml. Since atomic scattering factors for Ce are roughly three times those for Si for 100 eV electrons,[22] a uniform Ce layer should obscure fine structure related to substrate emission. The persistence of substrate structure indicates that a substantial fraction of the Si electrons are unscattered, i.e. much of the surface is free of Ce. (Results for intermixed Au/Si show Si Auger diffraction fine structure to be damped substantially more.) On the other hand, the Si attenuation reflects inelastic scattering of electrons which propagated through the Ce clusters. The damping of the fine structure at 1.2 ml indicates the increasing size of the reacted regions, consistent with cluster induced reaction. By coverages of 4 ml, the Si polar profile is completely featureless.

We have shown here that clusters form by ~0.1 ml coverage, but produce Ce/Si intermixing only for $\Theta > 0.6$ ml. Hence, the mechanism proposed by Zunger for Al/GaAs is not limited to simple metals on compound semiconductors, but may be important for a broad class of materials. We hope that this work will stimulate theoretical efforts to describe the early stages of interface formation, including clusters where appropriate, and establish the theoretical basis for the metal-overlayer-triggered reaction.

This work was supported by ARO DAAG29-83-K-0061 and a Northwest Area Foundation Grant of the Research Corporation (S.A. Chambers). Discussions with G. Margaritondo, F. Grunthaner, and A. Franciosi are gratefully acknowledged.

REFERENCES

@ Materials Science Program, University of Wisconsin, Madison, WI 53706

* Department of Chemistry, Bethel College, St. Paul, MN 55112

1. For an extensive review of metal/semiconductor interfaces see L.J. Brillson, Surf. Sci. Rep. 2, 123 (1982); and G. Margaritondo, Solid State Electron. 26, 499 (1983).
2. A. Franciosi, D.G. Peterman, J.H. Weaver and V.L. Moruzzi, Phys. Rev. B 25, 4981 (1982).
3. J.H. Weaver, M. Grioni, and J. Joyce, submitted Phys. Rev. 8/84.
4. A. Franciosi, P. Perfetti, A.D. Katnani, J.H. Weaver and G. Margaritondo, Phys. Rev. B 29, 5611 (1984).
5. R.R. Daniels, A.D. Katnani, Te-Xiu Zhao, G. Margaritondo and A. Zunger, Phys. Rev. Lett. 49, 895 (1982).
6. R. Ludeke and G. Landgren, J. Vac. Sci. Technol. 19, 667 (1981).
7. P. Skeath, I. Lindau, C.Y. Su and W.E. Spicer, Phys. Rev. B28, 7051 (1983)
8. J. Carelli and A. Kahn, Surf. Sci. 116, 380 (1982)
9. A. Mc Kinley, G.J. Hughes and R.H. Williams, J. Phys. C15, 7049 (1982).
10. G. Rossi, J. Nogami, I. Lindau, L. Braicovich, I. Abbati, U. del Pennino and S. Nannarone, J. Vac. Sci. Technol. A1, 781 (1983).
11. A. Zunger, Phys. Rev. B24, 4372 (1981).
12. D.J. Chadi and R.Z. Bachrach, J. Vac. Sci. Technol. 16, 1159 (1979).
13. E.J. Mele and J.D. Joannopoulos, Phys. Rev. Lett. 42, 1094 (1979).
14. J. van Laar, H. Huijser, and T.L. van Rooy, J. Vac. Sci. Technol. 16, 1164 (1979).

15. S.E. Louie, J.R. Chelikowsky, and M.L. Cohen, Phys. Rev. B 15, 2154 (1977).

16. S.A. Chambers and L.W.Swanson, Surf. Sci. 131, 385 (1983).

17. F.J. Himpsel, P. Heimann, T.-C. Chiang and D.E. Eastman, Phys. Rev. Lett. 45, 1112 (1980).

18. M. Grioni, J. Joyce, M. del Giudice, D.G. O'Neill, and J.H. Weaver (to be published.

19. D. Wieliczka, J.H. Weaver, D.W. Lynch and C.G. Olson, Phys. Rev. B26, 7056 (1982).

20. A. Franciosi, J.H. Weaver, N. Martensson and M. Croft, Phys. Rev. B 24, 3651 (1981).

21. P.H. Citrin and G.K. Wertheim, Phys. Rev. B27, 3176 (1983); and detailed references therein.

22. M. Fink and A.C. Yates, Atomic Data 1, 385 (1970).

FIGURE CAPTIONS

Fig. 1 Si 2p core total emission and deconvolution. The broken vertical line denotes 200 meV change in band bending. Representative statistics are given by dots for the clean surface at bottom.

Fig. 2 Energy distribution curves for $h\nu$=35 and 60 eV (left) and the difference curves (right) to highlight the Ce 4f character. Below 0.6 ml, the 4f indicates cluster formation. Above 0.6 ml, the 4f features shifts 0.7 eV and reflects local coordination with Si, as shown by comparison with $CeSi_2$ (bottom).

Fig. 3 Attenuation curves for Ce(N_4VV) and Si($L_{2,3}VV$) Auger intensity from normal emission spectra (top. Polar profiles are shown for the Ce(N_4VV) and Si($L_{2,3}VV$) Auger intensities for different coverages (middle and bottom). 90° is normal emission. All spectra taken in the (110) azimuthal plane perpendicular to the surface.

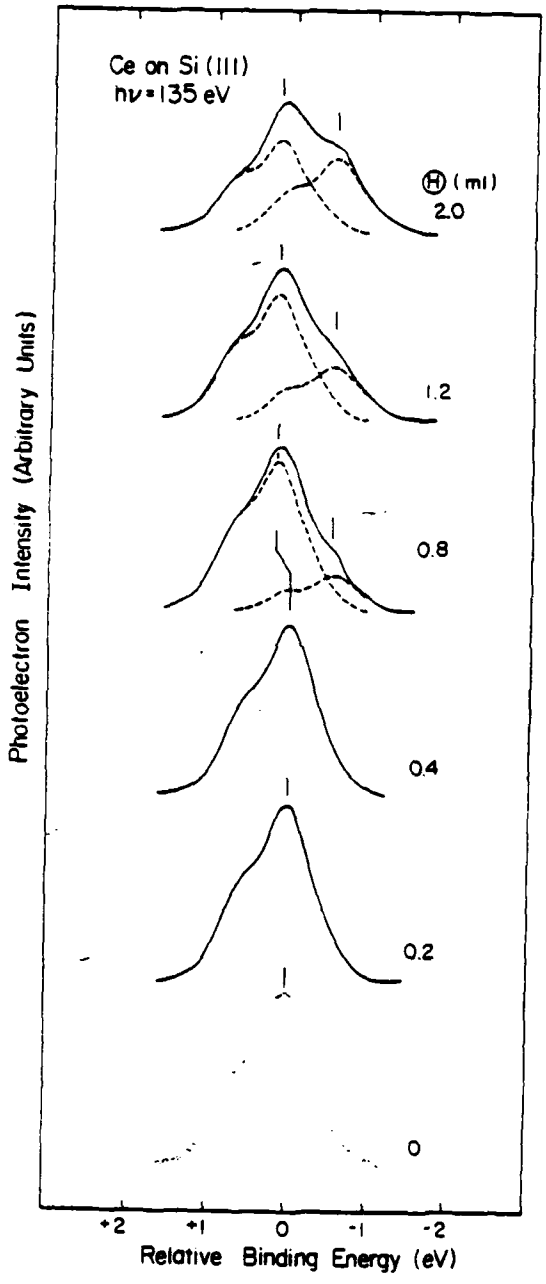
Ce on Si (111)
hν=135 eV
Θ (ml)
2.0
1.2
0.8
0.4
0.2
0
Photoelectron Intensity (Arbitrary Units)
+2
+1
0
-1
-2
Relative Binding Energy (eV)

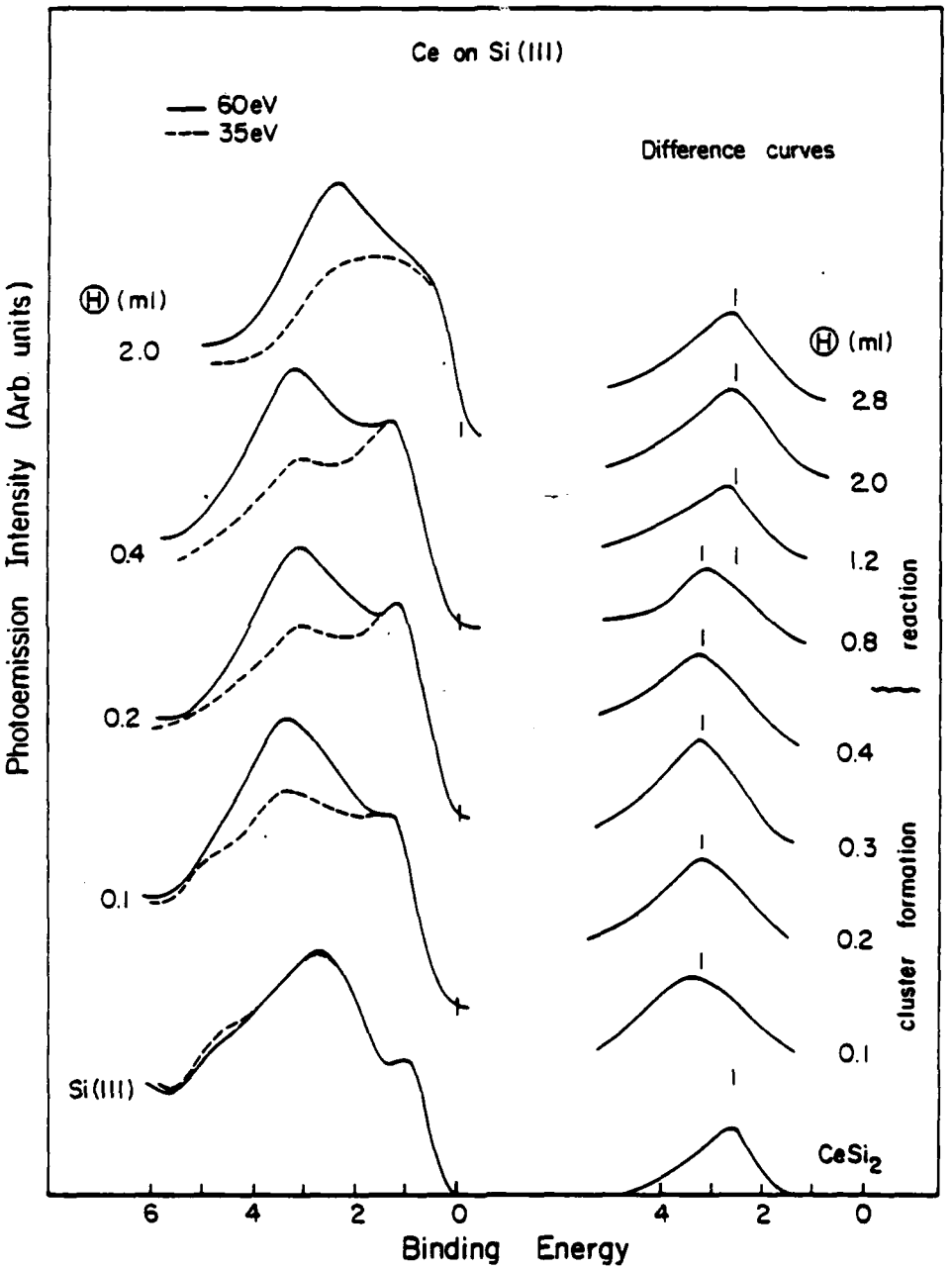
Ce on Si (III)
60eV
35eV
Difference curves
Photoemission Intensity (Arb units)
Θ (ml)
2.0
0.4
0.2
0.1
Si(III)
Θ (ml)
2.8
2.0
1.2
0.8
0.4
0.3
0.2
0.1
CeSi2
reaction
cluster formation
6
4
2
0
4
2
0
Binding Energy

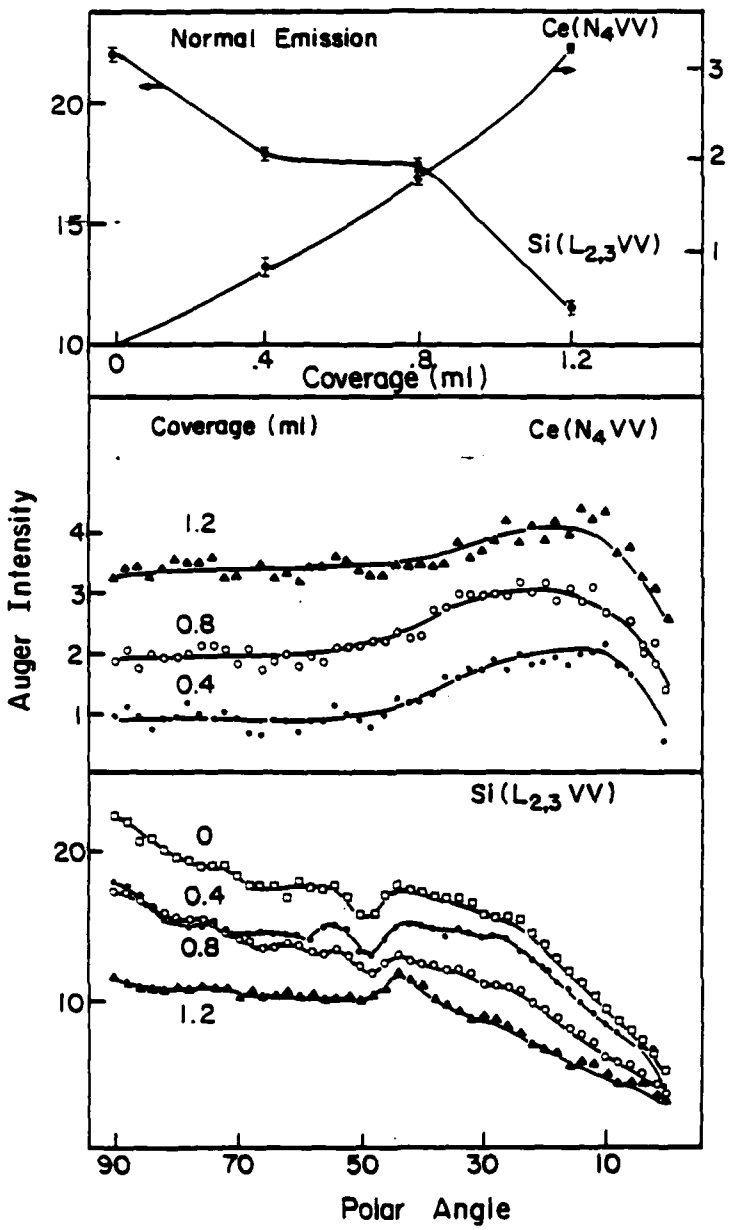
Normal Emission
Ce(N4VV)
Si(L2,3VV)
Coverage (ml)
Coverage (ml)
Ce(N4VV)
Auger Intensity
Si(L2,3 VV)
Polar Angle

QUANTITATIVE INTERDIFFUSION STUDIES OF NOBLE METAL/Si(111)-7x7 INTERFACES BY ANGLE-RESOLVED AUGER ELECTRON EMISSION

S.A. Chambers, T.R. Greenlee, and G.A. Howell

Departments of Chemistry and Physics
Bethel College, St. Paul, MN 55112

and

J.H. Weaver

Department of Chemical Engineering and Materials Science
University of Minnesota, Minneapolis, MN 55455

ABSTRACT

Polar-angle resolved Auger electron emission and related modeling have been used to determine quantitative details of composition and diffusion phenomena in the Cu/Si(111) and Au/Si(111) interface systems. The extent of Si outdiffusion increases with coverage in a gradual fashion for Au, with characteristic diffusion lengths (CDL) ranging from 18% of the overlayer thickness at a 2Å coverage to 39% at 20Å. In contrast, Si CDL values in Cu increase abruptly from 20% of the overlayer thickness at 2Å to ~35% at coverages from 5 to 20Å. Au diffuses deeply into the Si substrate, whereas Cu indiffuses only slightly (CDL = 1-2Å). These model predictions are consistent with the more substantial lattice disruption brought about by Au, leading to no long-range order in the overlayer, and the persistent diffusion of Si to the surface of 150Å thick Au overlayers.

PACS: 64.75.+g
66.30.Ny
73.40.-c
79.60.Gs

Evaporation of metal overlayers on single-crystal semiconductor surfaces at room temperature often results in substantial interdiffusion, a phenomenon not frequently observed in metal/metal or gas/metal chemisorption systems. Quantitative characterization of such interfaces places a new challenge before expermentalists. Although ion sputter depth profiling may be useful for semi-quantitative characterization of thick overlayers, its utility in studying thin overlayers ($\lesssim$20A) is limited. It seems that a non-destructive method of depth profiling that is sensitive to ultra-thin metal overlayers would be of considerable value. In this article we describe the first application of polar-angle resolved Auger electron emission to the quantitative characterization of metal-Si interfaces. We have chosen the noble metals Cu and Au because both are qualitatively known to intermix with Si.[1-4]

We make use of the fact that varying the polar angle Θ relative to the surface leads to selective enhancement of surface or bulk signals.[5] At a given polar angle Θ, the Auger intensity from a component characterized by an atom number density function $\rho(y)$ within the overlayer is given by,[6]

$$I(\Theta) = \left(\frac{I_0 \sigma A \Omega D}{\sin^2\alpha}\right)(1-R)\left(\frac{\sin\Theta'}{\sin\Theta}\right)\int_0^\infty \rho(y)\exp(-y/\Lambda\sin\Theta')dy. \qquad (1)$$

I_0 and A are the incident electron beam flux and cross-sectional area, respectively, σ is the Auger cross section, Ω is the solid angle of acceptance, D is the detector efficiency, α is the angle of incidence with respect to the surface, R is the electron reflection coefficient for Auger electrons passing through the surface potential barrier, Θ' and Θ are the propagation angles inside and outside the material, and Λ is the electron mean free path. The perpendicular depth y is measured relative to the

surface. In order to utilize Eq. 1 to determine $\rho(y)$ for components in an interface, the group of factors outside the integral (collectively referred to hereafter as $F(\theta)$) must be evaluated separately for pure substrate and overlayer materials. This task is readily accomplished by measuring $I(\theta)$ for atomically smooth surfaces of pure metal and semiconductor, and solving Eq. 1 for $F(\theta)$, recognizing that $\rho(y)$ is simply the bulk density of the material. Equation 1 can then be evaluated for both metal and semiconductor in a particular interface using $F(\theta)$ and physically reasonable choices for $\rho(y)$. Theory can then be fit to experiment to determine the optimal choice for $\rho(y)$.

We have employed an Auger electron spectrometer with angle-resolving capability described elsewhere.[7] Single crystal wafers of Si(111) were cleaned in situ by cycles of Ar ion bombardment and annealing to 800°C. The resulting surfaces showed a sharp reconstructed 7x7 LEED pattern and were free of contaminants, as judged by Auger spectra collected at θ=10° relative to the surface.

High purity Cu and Au were separately evaporated onto a Si substrate using a quartz crystal oscillator to monitor coverage. Pressures never exceeded 2×10^{-10} Torr at any stage of evaporation or measurement (base pressure = 4×10^{-11} Torr). Polar scans were constructed from spectra taken every 2° from θ=90° (normal emission) to θ=0°. LEED shows that at coverages above ~10Å, the Cu/Si(111) surface is ordered with a (111) orientation rotated 30° with respect to the substrate. Therefore, polar scans in two symmetry inequivalent azimuthal planes perpendicular to the surface were taken and averaged to remove intensity fluctuations due to diffraction effects. Since Au overlayers are disordered, polar scans in only a single azimuthal plane were collected.

In Figs. 1 and 2, we show Auger spectra as a function of coverage for the Cu and Au interfaces. In the bottom spectrum in each figure, sufficient metal has been deposited to bury essentially all the Si, even though at 150Å a small amount of Si diffuses to the surface of the Au overlayer. Polar profiles taken at these coverages are used to determine $F(\theta)$ for pure Cu and Au, although a slight correction is necessary for the latter to account for the small amount of Si still present on the surface. From similar spectra taken at normal emission, we have constructed attenuation curves in the form of $\ell n[I_{Si}(d)/I_{Si}(o)]$ vs. d, where d is the overlayer thickness in Å. A sharp interface would render this function linear, with slope equal to $-1/\Lambda$. In both cases, the plots exhibit positive deviations from linearity, indicating Si outdiffusion. The initial slope provides a good estimate of Λ. We obtain 2.8±.5Å and 5.0±.4Å for Cu and Au, respectively. These values are used in the evaluation of Eq. 1. Both metals induce either a splitting or a broadening of the $Si(L_{2,3}VV)$ line above a coverage of 2Å, indicating disruption of the Si lattice and modification of the Si valence states as interaction with the metal and outdiffusion proceed.[8] Qualitatively, the persistence of the $Si(L_{2,3}VV)$ line at coverages as high as 20Å indicates significant outdiffusion.

For both interface systems, the optimal choice of Si density function is given by

$$\rho(y) = \begin{cases} p_o \exp[-a(d-y)] \text{ for } y<d & (2a) \\ p_o \text{ for } y>d & (2b) \end{cases}$$

where p_o is the bulk density for Si(.05018 atoms/$Å^3$), d is the overlayer thickness, and a is a free parameter chosen to maximize agreement between theory and experiment. Table 1 shows optimal values of a and the predicted

Si density on the surface for coverages ranging from 2 to 20Å. Also, Fig. 3 shows the experimental and theoretical polar profiles based on the parameters in Table 1. The Cu-Si intermixed phase is ordered and the Si profiles at high coverages show strong diffraction modulation, in spite of averaging over two azimuthal planes. The disorder of the Au-Si intermixed phase is reflected by the lack of structure in Si profiles.

It is useful to define a characteristic diffusion length (CDL) as the diffusion depth of either Si in the overlayer, or metal in the substrate, by which the density has dropped to 1/e of its value at the interface boundary. As shown in Table I, the CDL increases gradually from 18% of the overlayer thickness at a Au coverage of 2Å to 39% at 20Å, whereas in Cu the CDL abruptly increases from 20% of the overlayer thickness at 2Å to ~35% at 5, 10 and 20Å.

For both metals, the best choice of density function is given

$$\rho(y) = \begin{cases} \rho_s + a_1 y & \text{for } y<d \text{ and all coverages} \quad (3a) \\ (\rho_s + a_1 d)\exp[-a_2(y-d)] & \text{for } y>d \text{ and } d<10\text{Å} \quad (3b) \\ \text{not measurable for } y>d \text{ and } d=20\text{Å} & \quad (3c) \end{cases}$$

Here, ρ_s is the metal density at the surface and is allowed to vary freely. When necessary, a_1 and a_2 were constrained to be <0 and >0, respectively. In this way, these functions represent a metal density which decreases linearly from surface to interface and decays exponentially in the substrate. The maximum probing depth is ~3λ (~11Å for both metal CVV Auger electrons). Using a technique described elsewhere,[6] values of 3.6 and 3.4Å were determined for the Cu($M_{2,3}VV$) and Au($N_{6,7}VV$) electrons, respectively. The resulting values of ρ_s, a_1 and a_2 are shown in Table 1. Interestingly, a_1 converged to zero for 5 and 10Å Cu coverages and would have been positive unless constrained. Similarly for 2, 4 and 8Å Au coverages, a_2 converged to

zero and would have been negative otherwise. Despite the constraints, the fits are quite good and, at higher coverages, the metal density at the surface is calculated to approach that of pure metal for both systems. Figure 4 shows the experimental and theoretical polar profiles for both metal overlayer systems. As in the Si polar profiles for the well-ordered Cu/Si(111) system, the Cu polar profiles show considerable diffraction fine structure at higher coverages, despite azimuthal averaging.

The results are best visualized by plotting the calculated densities as a function of distance from the interface boundary, as shown in Figs. 5 and 6. The picture which emerges is that Au reacts more vigorously, initiates more intermixing with longer metal CDL values, and exhibits a gradual onset of reaction. Cu, on the other hand, appears to trigger Si outdiffusion at coverages in excess of 2Å, as witnessed by an order of magnitude increase in surface Si density in going from 2Å to 5Å thicknesses, but does not penetrate as deeply; CDL values are limited to 1 to 2Å. These results are consistent with the extensive Si lattice disruption brought about by Au but not by Cu, leading to a disordered overlayer for the former. Moreover, the persistence of surface Si even at Au thicknesses of 150Å is in stark contrast with the complete disappearance of the Cu($M_{2,3}VV$) signal by a coverage of 60Å.

Through the use of polar-angle resolved Auger electron emission and appropriate modeling, we have extracted quantitative information about composition and diffusion phenomena in the Au/Si(111) and Cu/Si(111) interface systems. Such quantitative information is extremely important in modeling quantitative interface behavior and nicely complements photoemission spectroscopy, which provides insight into the chemical character of the intermixed phase.

ACKNOWLEDGEMENTS

S.A. Chambers, T.R. Greenlee, and G.A. Howell gratefully acknowledge support from a Northwest Area Foundation Grant of Research Corporation. J.H. Weaver was supported by the Army Research Office under grant numbers ARO-DAAG29-83-K-0061 and DAAG29-84-K-0169.

REFERENCES

1. F. Ringeisen, J. Derrien, E. Daugy, J.M. Layet, P. Mathiez, and F. Salvan, J. Vac. Sci. Technol. B1, 546 (1983).
2. G. Rossi, T. Kendelewicz, I. Lindau, and W.E. Spicer, J. Vac. Sci. Technol. A1, 987 (1983).
3. L. Braicovich, C.M. Garner, P.R. Skeath, C.Y. Su, P.W. Chye, I. Lindau, and W.E. Spicer, Phys. Rev. B 20, 5131 (1979).
4. L.J. Brillson, A.D. Katnani, M. Kelly, and G. Margaritondo, J. Vac. Sci. Technol. A2, 551 (1984).
5. C.S. Fadley and S.A.L. Bergstrom, Phys. Lett. 35A, 375 (1971).
6. S.A. Chambers, T.R. Greenlee, G.A. Howell, and J.H. Weaver, submitted to Phys. Rev. B.
7. S.A. Chambers and L.W. Swanson, Surf. Sci. 131, 385 (1983).
8. R. Matz, R.J. Purtell, Y. Yokota, G.W. Rubloff, and P.S. Ho, J. Vac. Sci. Technol. A2, 253 (1984).

TABLE 1

Model calculations of composition and diffusion phenomena based on experimental polar profiles

Cu/Si(111)

d(Å)	a	Si surface density* (atoms/Å^3)	Si CDL (Å)	a_1	a_2	Cu surface density** (atoms/Å^3)	Cu CDL (Å)
2	2.51	3.3×10^{-4}	.40	-2.9×10^{-2}	.667	1.0×10^{-1}	1.5
5	.602	2.5×10^{-3}	1.7	0	.452	6.9×10^{-2}	2.2
10	.282	3.0×10^{-3}	3.5	0	.923	8.2×10^{-2}	1.1
20	.143	2.9×10^{-3}	6.7	3.8×10^{-3}	-	7.9×10^{-2}	-

Au/Si(111)

d(Å)	a	Si surface density* (atoms/Å^3)	Si CDL (Å)	a_1	a_2	Au surface density+ (atoms/Å^3)	Au CDL (Å)≠
2	2.78	1.9×10^{-4}	.36	-5.8×10^{-3}	0	2.9×10^{-2}	∞
4	1.14	5.3×10^{-4}	.88	-2.7×10^{-3}	0	3.6×10^{-2}	∞
8	.345	3.2×10^{-3}	2.9	-1.9×10^{-3}	0	4.4×10^{-2}	∞
20	.128	3.9×10^{-3}	7.8	-2.8×10^{-3}	-	5.7×10^{-2}	-

*Bulk Si density = 5.0×10^{-2} atoms/Å^3

**Bulk Cu density = 8.5×10^{-2} atoms/Å^3

+Bulk Au density = 5.9×10^{-2} atoms/Å^3

≠"Infinite" means to the limit of depth sensitivity (3Λ or ~10Å)

FIGURE CAPTIONS

Fig. 1 Auger spectra for the Cu/Si(111)-7x7 interface as a function of coverage. The incident electron beam energy and current were 4 keV and 0.1 to 0.5 μA, respectively. Spectra were collected at a polar angle of 48° relative to the surface, and Θ=0° lies in the $(\bar{1}10)$ azimuthal plane perpendicular to the surface. 1Å of Cu equals 1.1 ml on the Si(111) surface.

Fig. 2 Auger spectra for the Au/Si(111)-7x7 interface and a 3 keV primary electron energy. 1Å of Au equals 0.75 ml on the Si(111) surface.

Fig. 3 Experimental and theoretical polar intensity profiles for the Si($L_{2,3}$VV) line in the two interface systems. The top panels show the smoothed clean-surface polar profiles used in determining $F(\Theta)$.

Fig. 4 Experimental and theoretical polar intensity profiles for the two metal CVV lines. The intensities in the top right-hand panel have been increased proportionately to stimulate a completely Si-free Au surface.

Fig. 5 Cu and Si atom number densities as a function of distance from the interface boundary, as determined by fitting intensities calculated using Eq. 1 to those from experiment. Dashed lines indicate extrapolations beyond the maximum probing depth of 3Λ.

Fig. 6 Au and Si atom number densities as a function of distance from the interface boundary, as determined by fitting intensities calculated using Eq. 1 to those from experiment. Dashed lines indicate extrapolations beyond the maximum probing depth of 3Λ.

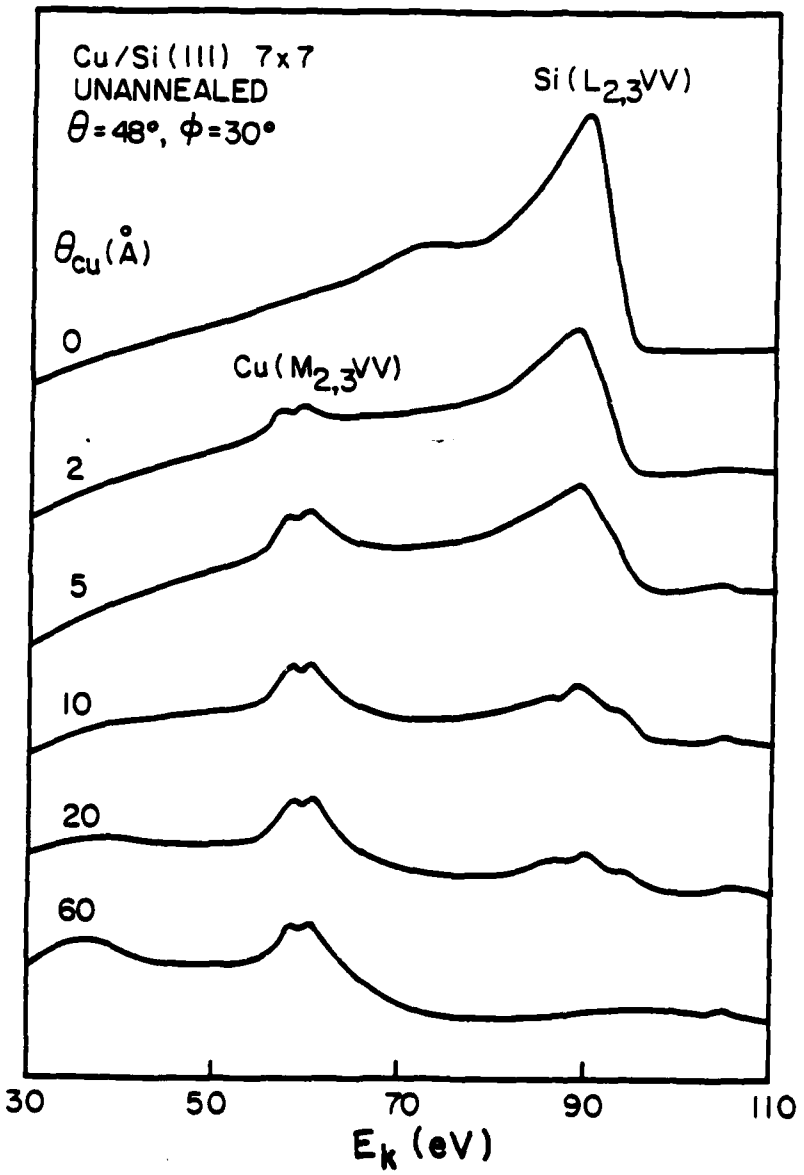
Cu/Si(111) 7x7
UNANNEALED
θ=48°, φ=30°
Si(L2,3VV)
θCu(Å)
0
Cu(M2,3VV)
2
5
10
20
60
30
50
70
90
110
Ek (eV)

Fig. 1

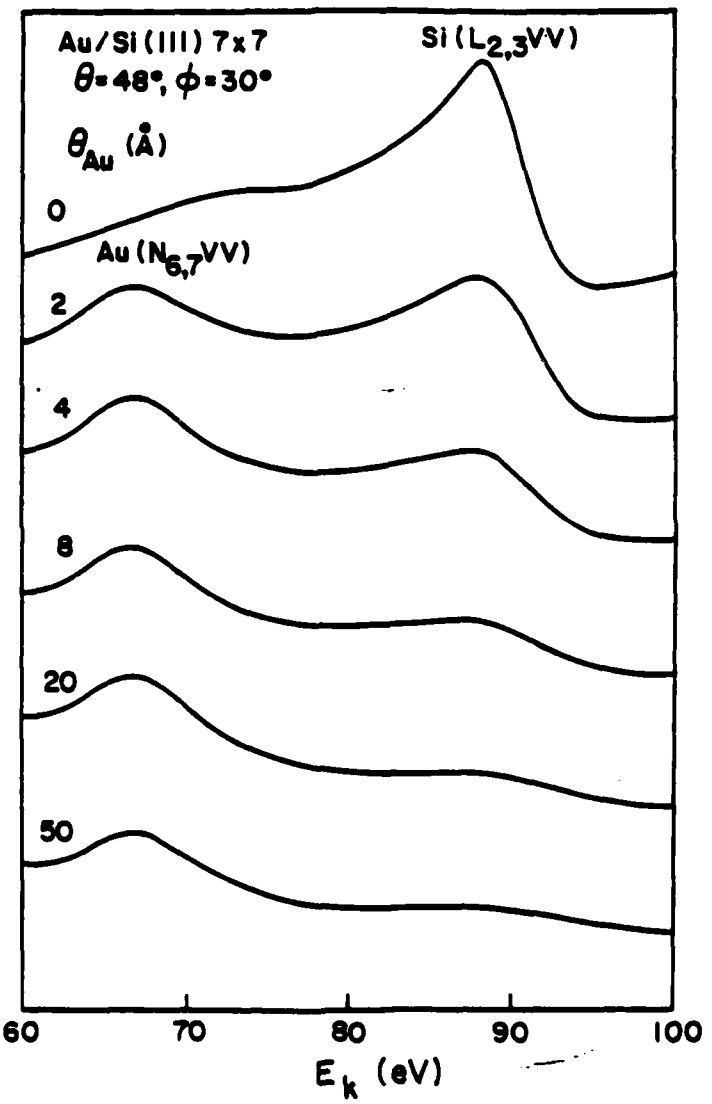
Au/Si(111) 7x7
θ=48°, φ=30°
Si(L2,3VV)
θAu (Å)
0
Au(N6,7VV)
2
4
8
20
50
60
70
80
90
100
Ek (eV)

Fig. 2

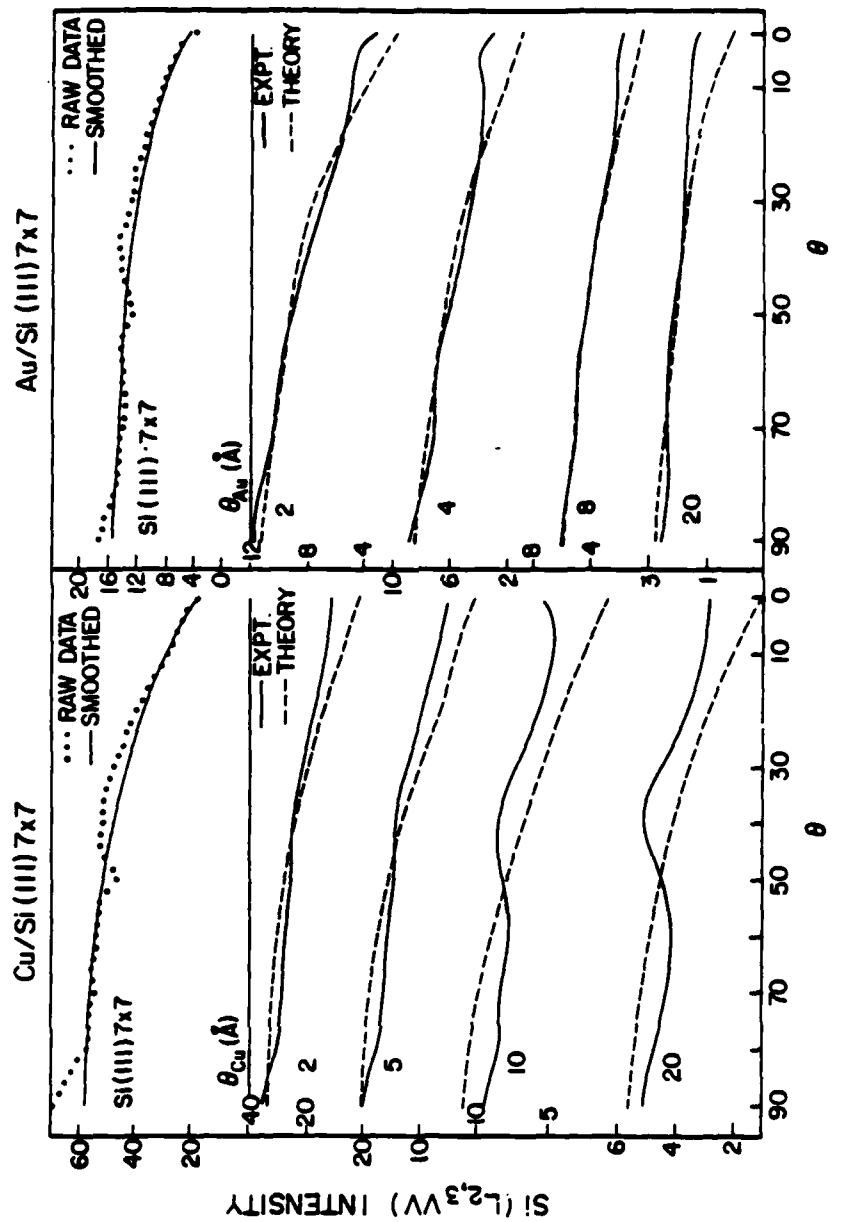
Au/Si (111) 7x7
Cu/Si (111) 7x7
... RAW DATA
— SMOOTHED
Si (111) 7x7
— EXPT.
--- THEORY
θ_{Au} (Å)
θ_{Cu} (Å)
Si ($L_{2,3}VV$) INTENSITY
θ

Fig. 3

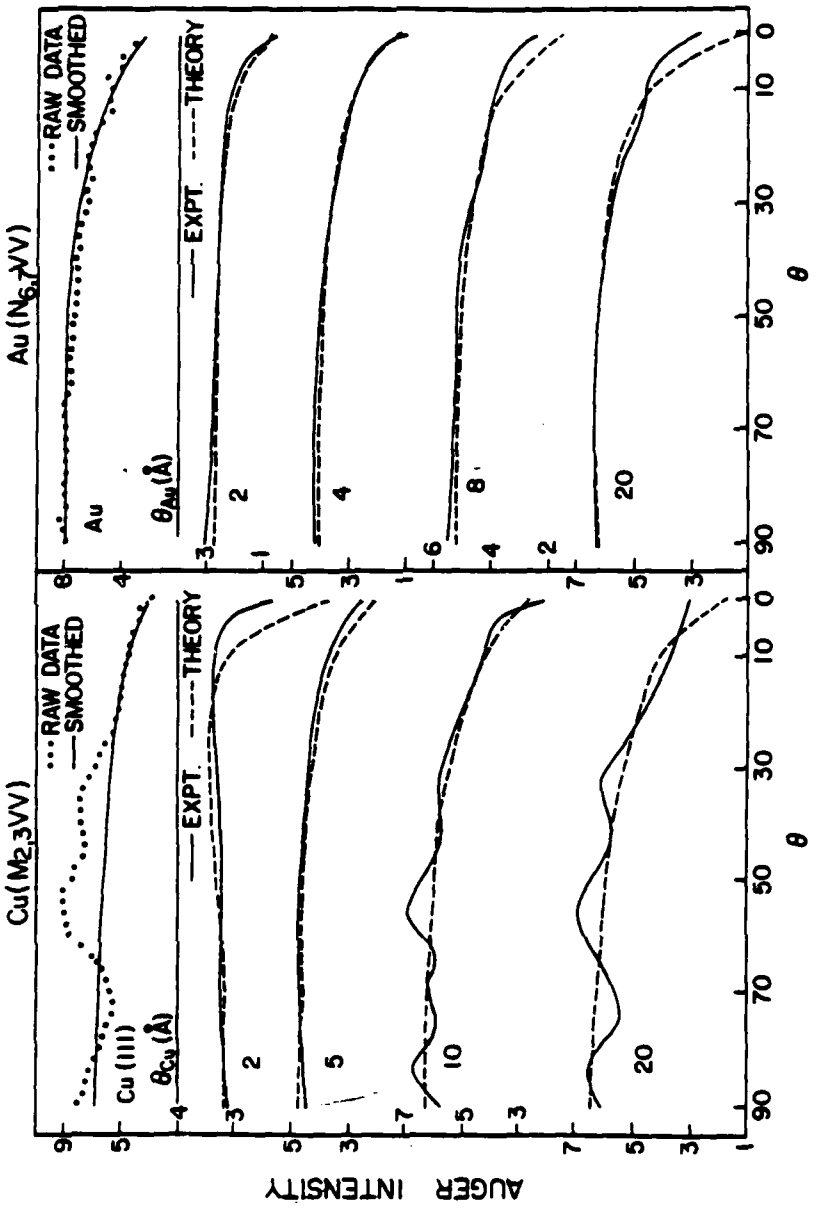
Cu(M2,3VV)
Au(N6,7VV)
RAW DATA
SMOOTHED
EXPT.
THEORY
Cu (111)
Au
θCu (Å)
θAu (Å)
AUGER INTENSITY
θ

Fig. 4

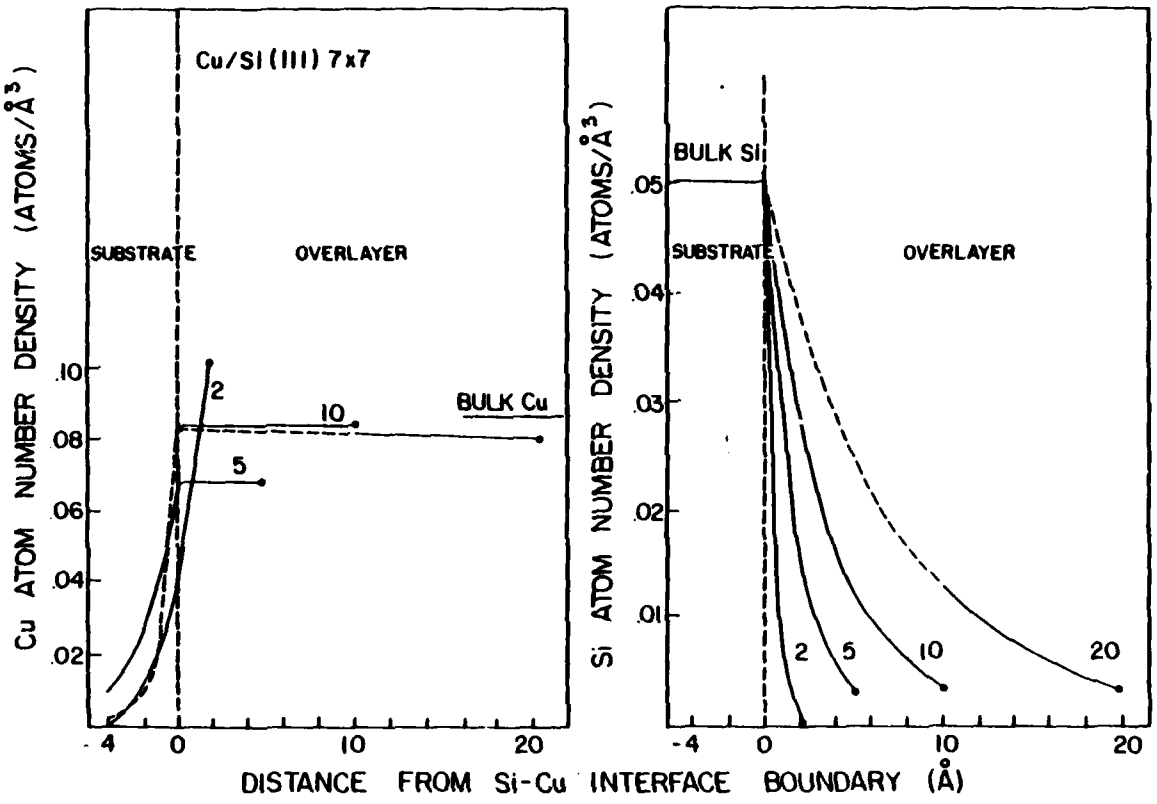
Cu/Si(111) 7x7
SUBSTRATE
OVERLAYER
Cu ATOM NUMBER DENSITY (ATOMS/Å³)
.10
.08
.06
.04
.02
2
5
10
BULK Cu
-4
0
10
20
BULK Si
.05
.04
.03
.02
.01
Si ATOM NUMBER DENSITY (ATOMS/Å³)
2
5
10
20
DISTANCE FROM Si-Cu INTERFACE BOUNDARY (Å)

Fig. 5

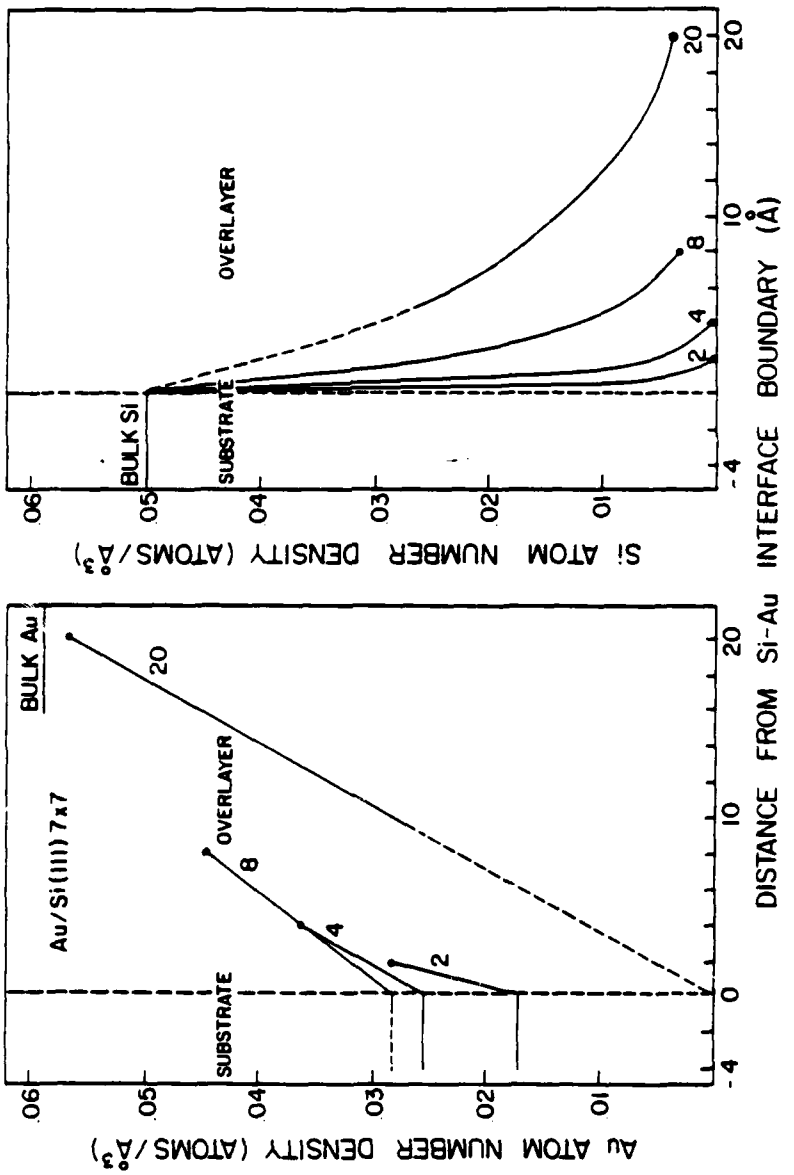
Au ATOM NUMBER DENSITY (ATOMS/Å³)
Si ATOM NUMBER DENSITY (ATOMS/Å³)
DISTANCE FROM Si-Au INTERFACE BOUNDARY (Å)
BULK Au
Au/Si(111) 7x7
OVERLAYER
SUBSTRATE
BULK Si
OVERLAYER
SUBSTRATE
20
8
4
2
20
8
4
2

Fig. 6

Modeling A Heterogeneous Metal/Semiconductor Interface: Ce on Si(111)

M. Grioni, J. Joyce*, M. del Giudice, D.G. O'Neill* and J.H. Weaver

Department of Chemical Engineering and Materials Science
University of Minnesota, Minneapolis, MN 55455

Abstract

High resolution synchrotron radiation photoemission studies of Ce deposited onto cleaved Si(111)-2x1 reveal heterogeneous growth which involves clustering, Ce/Si reaction to form silicide patches, lateral silicide growth, and finally Ce overlayer formation with surface segregated Si. Core level lineshape analysis reveals three distinct Si local bonding configurations. The relative interface concentration of each Si specie has been determined as a function of overlayer thickness, and a model for this interface is presented and discussed.

PACS: 73.40.+y
73.40.-c
73.40.Ns
79.60.Gs

Interface interactions are often modeled by uniform layers of reacted or unreacted material on stable substrates. Although the assumption of a homogenous interface simplifies modeling,[1] it is not correct for many interfaces.[2-16] Indeed, interface reactivity, kinetics, and chemical trapping are difficult to treat within the homogeneous layer model. Further, treatments of Schottky barrier formation based on uniform overlayers fall short of adequately describing the behavior of the barrier at low coverage.[2-3] Unfortunately, while the importance of heterogeneity has long been recognized, few studies have been able to resolve lateral features at an interface.

In this paper, we discuss an interface having a richness of phenomena related to heterogeneous growth: Ce/Si(111). As we will show, results obtained with high resolution core level photoemission make it possible to model even complicated systems by distinguishing the different electronic configurations of the constituents. Such core level studies are complemented by valence band results which emphasize changes in the states near the Fermi level E_F.

In a previous paper,[17] we discussed the submonolayer behavior of the Ce/Si(111) interface, demonstrating cluster formation by combining core level and valence band photoemission, LEED, and angle-resolved Auger spectroscopy. Here, we emphasize the development of the interface subsequent to the ripening of the clusters (reaction), describing the varying environments which evolve with coverage at room temperature.

The photoemission experiments were conducted at the Wisconsin Synchrotron Radiation Center using the Tantalus storage ring and the grasshopper and toroidal grating monochromators. The overall resolution of the measurements ranged from 200 meV at $h\nu$=40 eV to 500 meV at $h\nu$=135 eV.

Ce was deposited onto cleaved Si(111)-2x1 surfaces in an experimental system described in detail elsewhere.[18] During evaporation, the pressure rose from operating pressures of $3x10^{-11}$ to $\sim 1x10^{-10}$ Torr. Evaporation rates of ~1Å/min and the use of a shutter permitted 0.04 ml incremental depositions without difficulty. In this paper, coverages will be defined in monolayers where 1 ml=2.6 Å = $7.8x10^{14}$ atoms-cm^{-2}, the surface density of Si.

In Fig. 1 we show valence band energy distribution curves (EDCs) for Ce coverages 0-16 ml. Although the EDCs have been drawn with approximately the same height, comparison of absolute count rates shows that the Ce-derived features very quickly dominate the Si emission, indicative of the higher photoionization cross section of Ce 5d4f states relative to Si sp^3 states at $h\nu$=40 eV.[19] The difference curve at the bottom of Fig. 1 gives the result of subtraction of normalized EDCs for clean Si and 0.4 ml Ce/Si. For this difference curve, the well-defined doublet 1.2 and 3.2 eV below E_F reveals emission from Ce-induced states and is indicative of weakly interacting Ce clusters, as proven by valence band, LEED and angle-resolved Auger results (Ref. 17). With increasing coverage, the spectral features change as peak "A" near E_F is lost and the valence band becomes relatively structureless. At that point, the interface photoemission spectra can no longer be described as the superposition of unreacted Si and Ce clusters. By Θ=2.4 ml the interface product is metallic with a distinct Fermi level cutoff. At 4 ml coverage, a sharp feature emerges at E_F and grows relative to the deeper structure and the valence band narrows, ultimately converging to Ce. Figure 1 therefore shows that valence band emission can be readily identified at low coverage (clusters) and high coverage (Ce metal overlayer), but continuous evolution at intermediate coverage suggests a broad, intermixed

interface or a heterogeneous interface. Core level studies make it possible to rule out the former.

The results on the left of Fig. 2 show the Si 2p core emission measured with high surface sensitivity ($h\nu$=135 eV, escape depth ~4A[20]). The bottom-most EDC for clean Si(111)-2x1 reveals the characteristic 2p doublet broadened by surface-shifted components.[20] At submonolayer coverage, it shifts rigidly to greater binding energy (band bending without chemical reaction).[17] At $\Theta \simeq 0.6$ml a reacted component appears and grows relative to the original component, as indicated by the tic marks shifted 0.67 eV. For $\Theta \gtrsim 3$ml, a third Si doublet is observed at 1.2 eV lower binding energy than bulk Si. This component persists to very high coverage and the Si 2p lineshape is significantly sharper than for the clean surface, suggesting a more atomic Si bonding configuration.

On the right of Fig. 2, we show the deconvolution of the experimentally observed Si 2p emission into three spin-orbit-split pairs with branching ratios and spin-orbit splittings equal to those of Ref. 20. For each, the experimental full width at half maximum (FWHM) was derived from results at Θ=0.2 ml where the surface shifted component was small and the linewidth was a measure of our resolution. Comparison shows this FWHM to be ~0.1 eV larger than for the clean surface, analogous to what has been observed by Ludeke et al.[5] in detailed examinations of the nonreactive Ag/GaAs(110) interface. Such broadening is physically reasonable for the room temperature reacted phase because of the likely existence of not-quite-identical bonding configurations for Si, i.e. to disorder within the dominant local bonding configuration. The significant conclusion from Fig. 2 is that the experimental lineshapes can be fit very well for all coverages by assuming only three unique Si configurations (three doublets).

The attenuation of the total Si 2p emission is a measure of the rate at which Si is masked by the overlayer. However, for a reacted interface with several components, it is much more informative to consider the attenuation of each component separately. In Fig. 3 we display the attenuation results for the three Si components, $\alpha_i = \ln[I(2p_i(\Theta)/I(2p(\text{initial})]$. As shown, substrate Si-1 attenuation is rapid throughout the coverage range. The reacted Si-2 component grows with coverage from 0.6 ml to about 2.5 ml, but then diminishes sharply. The Si-3 component appears slightly above 3 ml and remains nearly constant with coverage, amounting to about 8% of the original Si intensity at Θ=24 ml (not shown).

An interface with behavior demonstrated by Figs. 1-3 is complex, but the results presented here allow formulation of a model which describes its heterogeneous growth. Although clusters form below 0.6 ml, they interact weakly with the substrate and the Si 2p binding energy does not change. At 0.6 ml, conversion from cluster growth to reactive intermixing occurs. Nonetheless, upon reaction the disrupted surface area is still only a portion of the total surface, having resulted from intermixing beneath and adjacent to the clusters. The emergence of the Si-2 signal reveals Si in these patches and comparison with unreacted Si shows the chemical inequivalence of the two configurations.

At 0.6 ml coverage, where the reacted Si component is first observed, the featureless valence band spectra give no evidence for a metallic Ce layer. However, both the valence bands and the core levels do indicate that a Ce layer forms shortly thereafter. In the valence bands, this can be seen by the reappearance near E_F of peak "A" - which ultimately becomes recognizable as Ce metal at high coverage. In the core levels, the fact that Si-2 reaches a maximum near 2.5 ml and is then rapidly attenuated

indicates a covering-up of the reacted specie for $\Theta \gtrsim 2.5$ ml. Nonetheless, the rate of attenuation of this reacted Si-2 specie is nearly exponential with a characteristic length of ~6Å, i. e. an escape depth larger than expected for a uniform overlayer of an efficient scatterer like Ce.[21] Likewise, the attenuation of the unreacted Si-1 specie suggests the presence of uncovered Si substrate at relatively high coverage.

The results for the intermediate coverage regime can be reconciled by modeling the interface as a patchwork of reacted Si on a matrix of unreacted substrate. Ce deposited onto the clean matrix will have the high mobility of Ce observed at lowest coverage and can diffuse to the edge of the reacted patches. The perimeter of these patches provides active sites for continued reaction due to the disruption of the substrate covalent bonds. As a result, Ce silicide growth (i. e. conversion of Si-1 to Si-2) involves a portion of Ce adatoms in the coverage range 0.6-3 ml and the patches grow laterally. This continues until most of the surface is reacted at about 3 ml nominal coverage.

In the intermediate coverage range, Ce deposition onto the reacted patches must be treated differently from that onto the unreacted Si surface, as indicated by the behavior of the Si-2 specie. The results of Figs. 1-3 indicate that, although the patches grow laterally, they apparently do not grow vertically. Instead, the reacted layer is rapidly covered up by Ce, as shown for example by the onset of the Ce-like valence band features and the decay of the Si-2 reacted specie. The slow Si-2 attenuation can be seen to result from the balance between Si-2 attenuation by the overlayer and Si-2 creation by the laterally-growing patches.

Deconvolution of the core emission demonstrates that the third Si specie appears at nominal coverages of 3 ml and all three Si components are present in about equal strength in the surface region for for $\Theta \simeq 5$ ml (~8% of the original signal). At this coverage, the valence band results show a metallic Ce overlayer, and the Si-2 attenuation reveals a covering-up of the reacted phase. Indeed, the appearance of Si-3 is coincident with the emergence of peak A in the valence bands. This strongly suggests that Si-3 is associated with the Ce film. Its persistence and nearly constant concentration suggests that Si-3 is surface segregated on the Ce film. For coverages greater than 5 ml, this floating Si is the most prevalent specie. By 8-10 ml there is no effectively no unreacted Si-1 or reacted Si-2 near the surface, consistent with the completion of silicide formation and Ce covering-up. Indeed, by this coverage the valence bands are converging on bulk Ce. The almost complete loss of Si-1 and Si-2 signals by 8 ml indicates that the Ce-Si reaction is confined to a thin, well-defined layer. In the inset of Fig. 2 we schematically show our model of the evolving Ce/Si interface, indicating the lateral growth of the silicide phase, its covering-up and the appearance of Si on the Ce overlayer.

Comparison of the present results with other rare-earth/Si interfaces show similarities and intriguing differences. All the systems studied so far (Ce/Si,[17] Sm/Si,[22] Eu/Si,[23] Yb/Si[24]) exhibit a critical coverage for the reaction and large chemical shifts indicative of substantial charge transfer in the reacted phase. On the other hand, while the Ce/Si interface is characterized by a low value of the Schottky barrier, as expected on the basis of recent results for technological samples,[12] no such lowering of the barrier was found for the Sm/Si system.[22] This difference is not understood at present and a systematic study of Schottky barrier formation involving

rare-earth metals and Si is needed. Moreover, the fact that the chemistry of rare-earth/Si systems is dominated by a critical temperature[25] suggests that interesting new effects in their evolution could be expected as a function of temperature. Work in this direction, particularly concerning the possible existence of ordered phases at high temperature, is currently in progress.

Finally, a significant point of this paper has been that high resolution studies of reactive interfaces make it possible to distinguish the chemical environments of the constituents, i. e. that specific bonding configurations form which can be identified even for intermixed interfaces where long range order is absent and the scale of the interface is limited to a few monolayers. Hence, we can conclude that strong local bonding determines the character of the evolving interface species. Comparison to bulk compounds will show how the interface phase fits into the hierarchy of the bulk phase diagram. For Ce/Si, we find no evidence that more than a single silicide phase exists, and whatever stoichiometry gradients might exist between the reacted patches and the unreacted Si are too small for identification. By studying the variation of each component with nominal metal overlayer coverage, even complex interfaces can be modeled. The implications of these conclusions are major because they indicate the limitations of modeling of interface properties based on homogeneous overlayers and they show the importance of microscopic fingerprinting of interface phases.

This work was supported by the Army Research Office under ARO-DAAG-29-83-K-0061. The Wisconsin Synchrotron Radiation Center is supported by the National Science Foundation, and the cheerful support of

its staff is gratefully acknowledged. Stimulating discussions with S. A. Chambers contributed to this work.

REFERENCES

* Materials Science Program, University of Wisconsin, Madison, WI 53706

1. E.H. Rhoderick, Metal-Semiconductor Contacts (Clarendon, Oxford, 1978).
2. For a general overview on metal semiconductor interfaces see L.J. Brillson, Surf. Sci. Rep. 2, 123 (1982) and G. Margaritondo, Solid State Electron. 26, 499 (1983).
3. A. Zunger, Phys. Rev. B 24, 4372 (1981).
4. R.R. Daniels, A.D. Katnani, Te-Xiu Zhao, G. Margaritondo, and A. Zunger, Phys. Rev. Lett. 49, 895 (1982).
5. R. Ludeke, T.C. Chiang, and T.M. Miller, J. Vac. Sci. Technol. B1, 581 (1983).
6. P. Skeath, I. Lindau, C.Y. Su, and W.E. Spicer, Phys. Rev. B 28, 7051 (1983).
7. J.H. Weaver, M. Grioni, and J. Joyce, submitted Phys. Rev. B.
8. P. Oelhafen, J.L. Freeouf, T.S. Kuan, T.N. Jackson, and P.E. Batson, J. Vac. Sci. Technol. B1, 588 (1983).
9. J. Freeouf and J.M. Woodall, Appl. Phys. Lett. 36, 690 (1981).
10. P. McKinley, G.J. Hughes, R.M. Williams, J. Phys. C 15, 7049 (1982).
11. L.J. Brillson, Phys. Rev. B 18, 2431 (1978).
12. R.D. Thompson, B.Y. Tsaur, K.N. Tu, Appl. Phys. Lett. 38, 535 (1981).
13. M. Saitoh, F. Shoji, K. Oura, and T. Hanawa, Japan. J. Appl. Phys. 19, L421 (1980).
14. G. Le Lay and J.P. Faurie, Surf. Sci. 69, 295 (1977).
15. F. Ringeisen, J. Derrien, E. Daugy, J.M. Layet, P. Mathiez, and F. Salvan, J. Vac. Sci. Technol. B1, 546 (1983).
16. J.D. McCaldin, J. Vac. Sci. Technol. 11, 990 (1974).

17. M. Grioni, J. Joyce, S.A. Chambers, D.G. O'Neill, M. del Giudice, and J.H. Weaver, submitted to Phys. Rev. Lett.

18. G. Margaritondo, J.H. Weaver, and N.G. Stoffel, J. Phys. E 12, 662 (1979).

19. D.M. Wieliczka, C.G. Olson, and D.W. Lynch, Phys. Rev. Lett. 29, 3028 (1984); D.M. Wieliczka, J.H. Weaver, D.W. Lynch, and C.G. Olson, Phys. Rev. B 26, 7056 (1982).

20. F.J. Himpsel, P. Heimann, T.-C. Chiang, and D.E. Eastman, Phys. Rev. Lett. 45, 1112 (1980); S. Brennan, J. Stohr, R. Jaeger, and J.E. Rowe, Phys. Rev. Lett. 45, 1414 (1980).

21. M. Fink and A.C. Yates, Atomic Data 1, 385 (1970).

22. A. Franciosi, P. Perfetti, A.D. Katnani, J.H. Weaver, and G. Margaritondo, Phys. Rev. B 29, 5611 (1984).

23. C. Carbone, (private communication).

24. E. Rossi, J. Nogami, I. Lindau, L. Braicovich, I. Abbati, U. del Pennino, and S. Nannarone, J. Vac. Sci. Technol. A1, 781 (1983).

25. J.E. Baglin, F.M. d'Heurle, and C.S. Peterson, Appl. Phys. Lett. 30, 594 (1980).

Figure Captions

FIG. 1. Energy distribution curves for Ce/Si showing valence band evolution. The bottom-most curve represents the normalized difference between clean Si(111)-2x1 and the interface with 0.4 ml coverage. At low coverage the spectra are superpositions of Ce and Si, at high coverage they converge to bulk Ce, but in the intermediate range, they reveal a heterogeneous interface.

FIG. 2. EDCs on the left show the evolution of the Si 2p core emission. On the right, lineshape deconvolutions are shown for representative coverages. At any coverage, the results can be fit with components representing clean Si (Si-1), a reacted phase (Si-2), and surface segregated Si (Si-3). Our model for the interface is shown pictorally in the inset.

FIG. 3. Attenuation of the total Si 2p emission (solid line at top) and the attenuation of each of its three components. Although the substrate attenuation is rapid and monotonic, the reacted component grows to a maximum near 2.5 ml and is then attenuated. The surface-segregated component appears only after the reacted component is covered-up by Ce and is nearly constant in magnitude to high coverage.

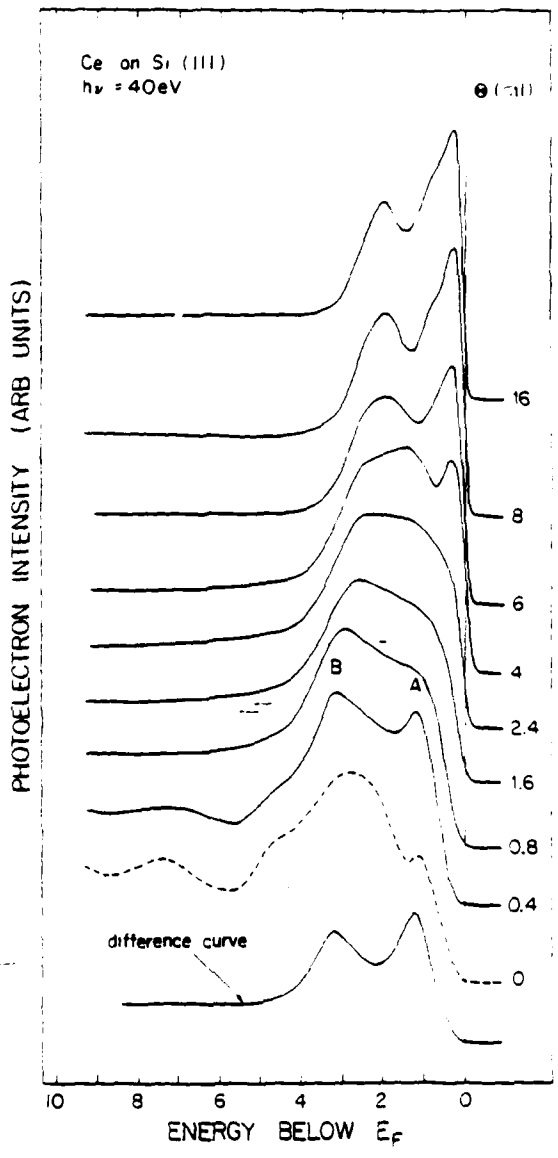
Ce on Si (111)
hν = 40eV
PHOTOELECTRON INTENSITY (ARB UNITS)
16
8
6
4
2.4
1.6
0.8
0.4
0
B
A
difference curve
10
8
6
4
2
0
ENERGY BELOW E_F

Fig. 1

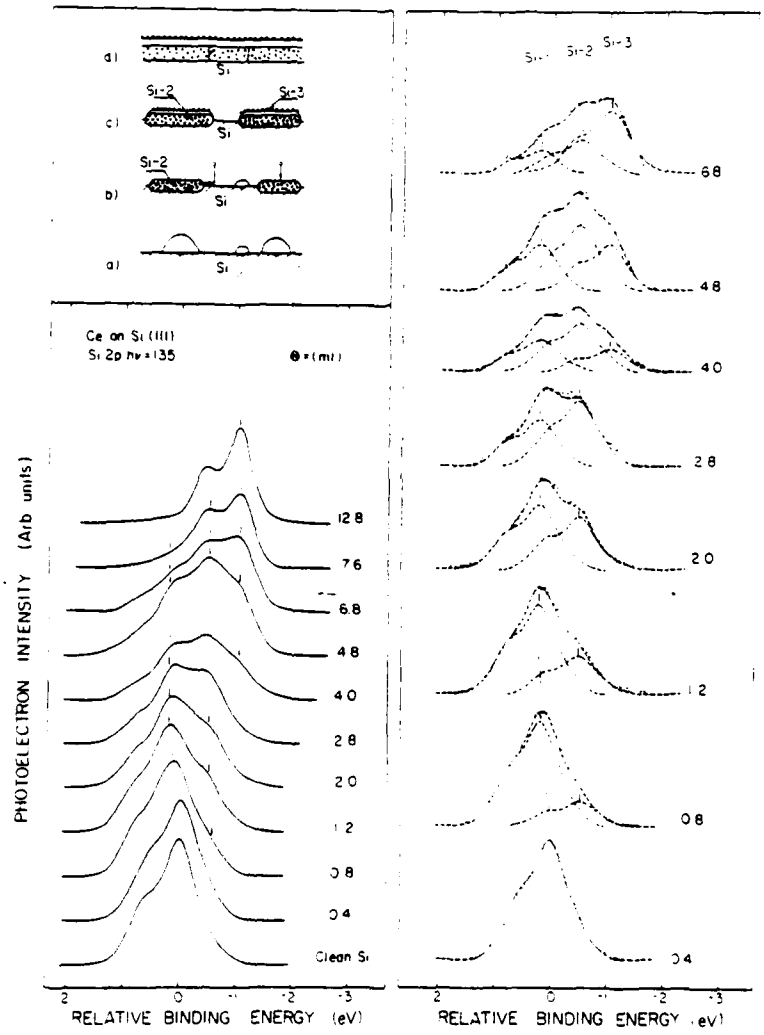
a)
Si
Si-2
Si-3
c)
Si
Si-2
b)
Si
a)
Si
Ce on Si (111)
Si 2p hν = 135
Θ = (ML)
PHOTOELECTRON INTENSITY (Arb units)
12.8
7.6
6.8
4.8
4.0
2.8
2.0
1.2
0.8
0.4
Clean Si
2
0
-1
-2
-3
RELATIVE BINDING ENERGY (eV)
Si-2
Si-3
6.8
4.8
4.0
2.8
2.0
1.2
0.8
0.4
2
0
-1
-2
-3
RELATIVE BINDING ENERGY (eV)

Fig. 2

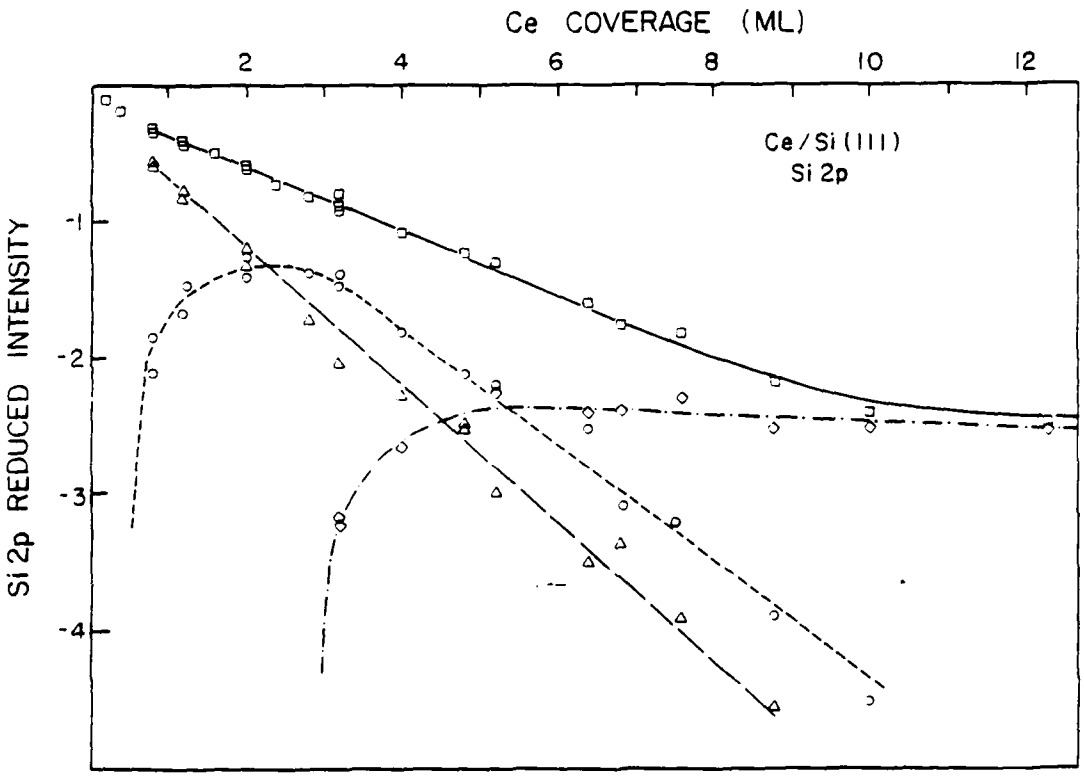
Ce COVERAGE (ML)
2
4
6
8
10
12
Ce/Si(111)
Si 2p
Si 2p REDUCED INTENSITY
-1
-2
-3
-4

Fig. 3

CHARACTERIZATION OF INTERMIXING AT METAL-SEMICONDUCTOR INTERFACES BY ANGLE-RESOLVED AUGER ELECTRON EMISSION: Cu/Si(111)-7x7

S.A. Chambers, T.R. Greenlee, G.A. Howell

Departments of Chemistry and Physics
Bethel College, St. Paul, MN 55112

and

J.H. Weaver

Department of Chemical Engineering and Materials Science
University of Minnesota, Minneapolis, MN 55455

ABSTRACT

Si($L_{2,3}VV$) and Cu($M_{2,3}VV$) Auger intensities from the Cu/Si(111)-7x7 interface have been measured in a polar-angle resolved fashion for various Cu thicknesses. A simple theory of polar-angle resolved Auger emission has been developed and used to extract atom number densities for both Si and Cu as a function of depth. It is found that significant Si outdiffusion is triggered at 300K by Cu coverage in excess of 2Å. Cu diffuses into the substrate with a characteristic penetration depth of 1 to 2Å at all coverages and, above a coverage of 2Å, Si diffuses into the overlayer with a characteristic depth of ~35% of the overlayer thickness. The Cu density appears to be constant throughout the intermixed region.

PACS: 64.75.+g
66.30.Ny
73.40.-c
79.60.Gs

I. INTRODUCTION

Condensation of metal atoms on single-crystal semiconductor surfaces leads to a wide variety of interesting physical and chemical phenomena.[1] Ordered layer-by-layer growth, cluster formation,[2] interdiffusion,[3,4] and chemical reaction[5] have been observed for different systems. Successful observation of these phenomena requires a wide repertoire of experimental probes; no one technique can provide all the necessary information to unambiguously model the microscopic development of the interface.

In this paper we address the issue of interdiffusion at a metal-semiconductor interface. This research was undertaken because knowledge of the atomic densities of the substrate and adsorbed material as a function of depth in the interface region is critical for characterizing interface properties. Most attempts to obtain such information have utilized argon ion sputter profiling.[6-11] As discussed by some of these authors,[6-8] ion-induced surface damage, preferential sputter rates, implantation of sputtered species, depth calibration problems, and poor depth resolution render the quantitative reliability of this technique dubious, particularly when applied to ultra-thin overlayers (a few angstroms). In order to overcome these difficulties, attempts have been made to obtain a better understanding of the sputtering process[9,11] and to quantitatively account for the phenomenon of sputter broadening.[9]

A nondestructive alternative to sputter profiling which eliminates many of the above problems utilizes the polar angle dependence of Auger and photoelectrons emitted from both the substrate and overlayer. As originally demonstrated by Fadley and Bergstrom,[12] varying the collection angle relative to the plane of the surface leads to selective enhancement of bulk and surface signals. Most such studies to date have utilized core-level

photoelectrons excited by either conventional x-ray sources[13] or synchrotron radiation.[14] One disadvantage of polar-angle resolved photoemission is that of data acquisition time. In order to obtain a complete polar intensity profile, a large number of spectra must be taken over the collection angle range 0 to 90°. A minimum of nine or ten spectra would allow a rough polar profile to be constructed, but 20 to 40 spectra would be desirable. Active metal overlayers will contaminate in the several-hour time span required to acquire such detailed data by means of photoemission.

A closely related yet much faster approach to the problem involves utilizing the polar angle dependence of low-energy core-valence-valence (CVV) Auger electron intensity. An excellent spectrum can be obtained in the pulse-counting N(E) mode in just a few minutes. Moreover, low incident beam currents (a fraction of a μA) can be used to minimize surface damage and one still obtains very high count rates. In this article we describe the first use of polar-angle resolved Auger emission to quantitatively study interdiffusion phenomena at a metal-semiconductor interface. The Cu/Si(111)-7x7 system was chosen because interdiffusion of Si into the overlayer has been observed and qualitatively studied with other surface analysis techniques,[3,4] including XPS, UPS, AES, and LEED.

This article is organized as follows: Section II describes the theory of polar-angle resolved Auger emission as developed for this particular application, Section III provides experimental details, Section IV presents experimental and theoretical results, Section V consists of a discussion of the work, and conclusions are drawn in Section VI.

II. THEORY OF POLAR-ANGLE RESOLVED AUGER EMISSION FROM INTERMIXED OVERLAYERS

After an Auger electron has been ejected from an atom in a solid, it can be: (1) inelastically scattered, leading to signal attenuation, (2) elastically scattered, leading to diffraction effects if the sample is a single crystal, and (3) refracted at the surface-vacuum interface. In this model we treat the overlayer as a uniform slab with a constant attenuation coefficient and ignore any single-crystal effects.

Figure 1 shows the relevant geometry of our sample-analyzer arrangement. Auger electrons originating a perpendicular distance y from the surface propagate with internal angle θ' to refract at the surface and travel toward the analyzer aperture with external angle θ. The principal factor which governs intensity variations with depth is inelastic attenuation. Thus, the intensity at a given depth y will be proportional to $\exp(-y/\Lambda\sin\theta')$, where Λ is the electron mean free path. In addition, surface refraction will bring about changes in intensity due to internal reflection and what is effectively an increase in Auger electron flux caused by a reduction in the cross sectional area of the Auger electron beam upon refraction. These effects add factors of (1-R) and $\sin\theta'/\sin\theta$, respectively, where R is a reflection coefficient for Auger electrons within the sample incident on the surface.[15] Additional factors governing the observed intensity are incident electron beam flux (I_0), Auger cross section (σ), sample area irradiated ($A/\sin\alpha$), solid angle of acceptance (Ω), detector efficiency (D), and emitting atom number density at depth y ($\rho(y)$). Combining these factors, the differential intensity brought about by a volume element a perpendicular distance y from the surface is given by

$$dI(\theta,y) = [\frac{I_o \sigma A \Omega D}{\sin^2\alpha}][(1-R)(\frac{\sin\theta'}{\sin\theta})]\rho(y)\exp(-y/\Lambda\sin\theta')dy. \quad (1)$$

The propagation angle within the material (θ') is related to that outside by the conservation of $k_{\parallel}$ rule which yields,

$$\theta' = \cos^{-1}[(\frac{E_k - V_o}{E_k})^{1/2}\cos\theta]. \quad (2)$$

E_k is the electron kinetic energy inside the material and V_o is the inner potential. These refraction effects are very important at the kinetic energies of the CVV Auger transitions used here (~100 eV), particularly at low emission angles. As shown by Fadley,[15] the electron reflection coefficient can be estimated by treating the interaction of the electron with the surface as analogous to a particle penetrating a square well potential of height V_o, the inner potential of the material. From this model we get

$$R = [(1-(1-V_o/E_k\sin^2\theta')^{1/2})/(1+(1-V_o/E_k\sin^2\theta')^{1/2})]^2. \quad (3)$$

With the exception of the cross section, the factors within the first set of brackets in Eq. 1 depend only on the spectrometer. The factors in the second set of brackets, which account for the change in Auger electron flux brought about by surface refraction, can be combined with the instrument factors and cross section to yield a function $F(\theta)$, defined as:

$$F(\theta) = (\frac{I_o \sigma A \Omega D}{\sin^2\alpha})(1-R)(\frac{\sin\theta'}{\sin\theta}). \quad (4)$$

This function accounts for everything except the emitting atom number density in the material and electron attenuation, and should be approximately constant as coverage proceeds, provided the inner potential and cross section do not change substantially. Thus, if $F(\theta)$ is evaluated for each component in the interface, it could be used to deduce atomic densities in the intermixed phase. For single-crystals of Cu and Si, the inner potentials are 14 eV and 17 eV, respectively.[16,17] Therefore, we take 15 eV as an approximate value for the Cu-Si interface at all stages of development. In practice, we find that the calculated intensities are not particularly sensitive to the choice of V_o over the range 14 to 17 eV. Changes in CVV Auger cross section for either Cu or Si would result from valence band modification upon intermixing and are revealed by lineshape changes. No such changes have been observed for the Cu($M_{2,3}VV$) line. The Si($L_{2,3}VV$) line does split and broaden at higher Cu coverages and such effects are not incorporated into the model.

For pure samples of either substrate or overlayer material, $\rho(y)$ is simply equal to ρ, the bulk atom number density for each material. In this case, Eq. (1) is easily integrated over y and $F(\theta)$ can be directly evaluated. The result is

$$F(\theta) = \frac{I(\theta)}{\rho\Lambda\sin\theta}. \qquad (5)$$

Once determined for pure substrate (s) and overlayer (o) materials, $F_s(\theta)$ and $F_o(\theta)$ will be inserted into integrated forms of Eq. 1 appropriate to the interface.

$I(\theta)$, and hence $F(\theta)$, as used in Eq. 5 represent an average over the 8° polar angle resolution of our analyzer. For later use it is desirable to express $F(\theta)$ in units of per degree of polar angle. In order to make this adjustment, it is assumed that for all polar angles except 88°-90° and 0-2°, $I(\theta)$ increases linearly with θ over all 8° polar angle intervals. This approximation is reasonable in light of the observed behavior of $I(\theta)$ for both substrate and overlayer materials (to be discussed in more detail in Section IV A). It then suffices simply to divide $I(\theta)$ by 8° for each value of θ prior to evaluating Eq. 5. The fact that $I(\theta)$ is observed to go through a maximum at θ=90° and go to zero for θ<0° is used to perform a suitable adjustment to obtain an $I(\theta)$ per degree of polar angle for θ=88-90° and 0-2°.

In order to extract concentration information from the interface polar profiles, a particular form of $\rho(y)$ for both substrate and overlayer material is assumed. Equation (1) can then be integrated to yield expressions for $I_s(\theta)$ and $I_o(\theta)$. For the substrate material,

$$I_s(\theta) = F_s(\theta)\int_o^\infty \rho_s(y)\exp(-y/\Lambda_s \sin\theta'_s)dy \qquad (6)$$

and similarly for the overlayer. The function $\rho(y)$ contains one to three undetermined parameters which are chosen to generate the best fit with experiment. The fitting algorithm used is a combination of gradient search and linearization of the fitting function methods developed by Marquart.[18] Further details on the exact choice of $\rho(y)$ are given in Section IV A.

Finally, comparison of theoretical results with experimental polar profiles requires that the former, which come out per degree of polar angle, be integrated over the finite aperture size of 8°. This task is readily

accomplished using Simpson's and trapezoidal rules in the calculation of $I(\theta)$.

III. EXPERIMENTAL DETAILS

The system used to perform angle-resolved Auger spectroscopy is described in detail elsewhere.[19] The single-pass CMA with angle-resolving capability is also used as a LEED I-V detector, employing a modification first described by McDavid and Fain.[20] Single-crystal wafers of (111) oriented p-type Si were cleaned by cycles of Ar ion sputtering and heating to 800°C. This procedure produced a clean 7x7 surface; no impurities were present as judged by Auger spectra taken at a surface-enhancing polar angle of 10°.

Evaporation of high-purity Cu was monitored by a quartz crystal oscillator. Pressures during evaporation never exceeded 2×10^{-10} Torr and during polar scans were typically $7\text{-}9\times10^{-11}$ Torr. Complete polar scans from normal emission to grazing emission were obtained by taking spectra every 2°. Replicate measurements at fixed angles indicated a standard deviation of 3-4% of the value of the mean. The total time required to complete a full polar scan was about two hours and grazing emission Auger spectra taken at the end of each run showed that the surface was free of contaminants. Polar profiles were obtained in the $(\bar{1}10)$ azimuthal plane perpendicular to the surface and in a plane rotated 30° from $(\bar{1}10)$. These were then averaged to remove as much diffraction modulation as possible, since our theoretical model ignores single-crystal effects. For future reference, we define the zero in ϕ as lying in the $(\bar{1}10)$ plane perpendicular to the surface.

4 KeV electrons were used to excite the Auger transitions and incident beam currents were typically 0.1-0.5μA. There was no evidence of electron-induced surface damage at any point, as judged by reproducible Auger intensities and LEED patterns over several hours of beam irradiation. Peak intensities were determined by smoothing the spectra, substracting a linear background, and integrating. Spectra were then normalized to one another by dividing by the average number of background counts on the flat high-energy side of the Si($L_{2,3}VV$) peak, thus removing intensity variations brought about by drifts in the incident beam current.

IV. RESULTS

Figure 2 demonstrates how the Auger spectrum develops as a function of Cu coverage. Coverages are expressed in Angstroms, and one Angstrom of Cu equals 1.1ML on the Si(111) surface. From 0-2Å there is no significant change in the Si($L_{2,3}VV$) lineshape. However, above 5Å a triplet develops, indicating substantial modification of the valence states of Si as the normal sp^3 hybrid bonds are broken and Si diffuses into the Cu layer. Similar lineshape changes have been observed as a function of coverage for Pt/Si(111),[21] Pd/Si(111),[22] and Cu/Si(111).[4] Using spectra taken at normal emission, one can construct a Si($L_{2,3}VV$) attenuation curve to determine the extent to which interdiffusion occurs.

Figure 3 shows a plot of $\ln(I(d)/I(0))$ vs d where d, I(0), and I(d) are the overlayer thickness, clean surface Si($L_{2,3}VV$) intensity, and Si($L_{2,3}VV$) intensity with overlayer thickness d present, respectively. Each point is an average of four spectra taken at normal emission and the standard deviation of each data set is less than 4% of the mean for that set. Linear behavior with slope $-1/\Lambda$ is expected if the interface is sharp, and the

observed positive deviation from linearity indicates outdiffusion of Si. The initial slope provides a good estimate of the mean free path for the Si($L_{2,3}VV$) electron moving through the overlayer. In this case, we get 2.8±.5A. In the evaluation of Eq. 5, we use a value of 3A. Also shown for reference is a growth curve for the Cu($M_{2,3}VV$) line.

Corresponding LEED data indicate relaxation of Si(111)-7x7 to a rapidly weakening Si(111)-1x1 pattern for 2 and 5 A coverages, followed by the appearance at 10A of a Cu(111)-1x1 pattern rotated 30° with respect to the Si surface mesh. These results are in good agreement with those obtained by Ringeisen et al.[3]

In Figs. 4 and 5 we present polar angle intensity profiles for the Si($L_{2,3}VV$) and Cu($M_{2,3}VV$) Auger intensities in two symmetry-inequivalent azimuthal planes. The top profiles in each panel correspond to pure Si (Fig. 4) or Cu (Fig. 5) and contain the information from which $F_s(\theta)$ and $F_o(\theta)$ are evaluated (Eq. 5). At a coverage of 60A, no Si($L_{2,3}VV$) signal was present and the LEED I-V curves were those expected for a Cu(111) single-crystal surface film. Thus we take this surface as our reference surface for pure Cu(111).

The diffraction modulation observed in each case is a sensitive probe of the local structure of the emitting atom and can be used as a structural fingerprint at other coverages. At 2A coverage, the diffraction modulation observed for the clean Si(111)-7x7 suface is weakened but still present and the Cu profile is essentially featureless. Coupled with the weak Si(111)1x1 LEED pattern and the attenuation curve in Fig. 3, these data suggest that the Cu layer grows in a weakly ordered layer-by-layer fashion, up to 2A. This mode of growth diminishes and gives rise to reaction and outdiffusion at 5A, as evidenced by the Si lineshape change and deviations from linearity

of the Si($L_{2,3}VV$) attenuation curve (Fig. 3). By 10A, the Cu polar profiles show clear similarities to those of the 60A film (pure Cu(111)). However, a significant amount of Si remains dispersed throughout the overlayer and the increased Si($L_{2,3}VV$) splitting indicates a more substantial chemical interaction with the Cu. There are no substantive changes between 10A and 20A, except that the overlayer is only slightly richer in Cu but poorer in Si by a factor of 2. At 60A, the evolution of the overlayer to a pure Cu(111) film is complete and no Si is present on the surface.

In the top panels of Figs. 6 and 7, we present average polar profiles for clean Si(111)-7x7 and a 60A Cu overlayer (essentially a pure Cu(111) surface). Each profile is an average over two symmetry inequivalent azimuthal planes (ϕ=o° and ϕ=30°). As can be seen, such averaging is not sufficient to remove all the diffraction features. Therefore, for the purpose of evaluating $F_s(\theta)$ and $F_o(\theta)$, we effectively smooth out the remaining diffraction modulation. Then, after adjusting the intensities for 8° angular resolution as discussed in Section II, these curves are used to evaluate $F(\theta)$ for Si($L_{2,3}VV$) and Cu($M_{2,3}VV$) Auger emission through the use of Eq. 5.

Also shown in Figs. 6 and 7 are the experimental polar profiles averaged over azimuthal planes at ϕ=o° and ϕ=30° compared to those predicted by Eq. 6 for the best choice of density function. For both Si($L_{2,3}VV$) and Cu($M_{2,3}VV$) emission calculations, physically plausible atom number density functions of various forms with one, two, or three undetermined parameters were tried. For each function, the fitting routine determined the choice of parameters which yielded a minimum value of χ^2. Turning first to the distribution of Si in the interface, a linear function and an exponential function were modeled. The linear function was of the form

$$\rho(y) = \begin{cases} \rho_0 - a(d-y) \text{ for } y<d & (7a) \\ \rho_0 \text{ for } y>d & (7b) \end{cases}$$

and the exponential function was of the form

$$\rho(y) = \begin{cases} \rho_0 \exp[-a(d-y)] \text{ for } y<d & (8a) \\ \rho_0 \text{ for } y>d. & (8b) \end{cases}$$

Here ρ_0 is the bulk atom number density of Si(5.018×10^{-2} atoms/A^3), d is the overlayer thickness, a is the undetermined parameter, and y is the perpendicular distance measured from the surface. It is found that the exponential function gives a much better fit to the experimental data than does the linear function; χ^2 for the exponential function was 1.5 times lower at 2A coverage and 3 times lower at 20A coverage than that for the linear function. For both functions, a mean free path of 3A was used, as discussed earlier. The optimal values of a and the predicted Si atom number densities on the surface are given in Table I.

Clearly, the calculated surface Si density is an order of magnitude lower at 2A than that for the 5, 10, and 20A overlayers, indicating a substantial increase in outdiffusion above 2A. Moreover, for all coverages above 2A, the characteristic penetration depth (distance into the overlayer by which the Si density has decayed to 1/e of its bulk value) is approximately 35% of the overlayer thickness, whereas for 2A it is only about 20% of the overlayer thickness. These results are supported by the observed change in Si($L_{2,3}VV$) lineshape above 2A.

For the Cu distribution calculation, we have used a linear function which terminates discontinuously at the Cu-Si interface and a linear function with an exponential tail into the substrate. In analytical form, the functions are

$$\rho(y) = \begin{cases} \rho_s + a_1 y & \text{for } y<d \quad (9a) \\ 0 & \text{for } y>d \quad (9b) \end{cases}$$

and

$$\rho(y) = \begin{cases} \rho_s + a_1 y & \text{for } y<d \quad (10a) \\ (\rho_s + a_1 d)\exp[-a_2(y-d)] & \text{for } y>d. \quad (10b) \end{cases}$$

Here, ρ_s is the Cu number density at the surface (a free parameter), d and y are as defined previously, and a_1 and a_2 are undetermined parameters. The Cu($M_{2,3}VV$) mean free path was determined by performing a two-parameter fit on the 20Å coverage and employing a linear density function of the form $\rho(y)=.078+a_1 y$, where a_1 and Λ were allowed to vary. The value .078 was chosen because values of .078 to .079 routinely result from two-parameter fits using the form $\rho(y)=\rho_s+a_1 y$ with a fixed value of Λ taken from the universal mean free path curve.[23] This calculation generates a value of 3.6Å for Λ, which is used in all subsequent calculations. In general, the χ^2 values are slightly lower for the linear functions (9a&b) than for the linear-exponential functions (10a&b) for all coverages. However, from the point of view of using physically reasonable results, we judge the linear-exponential functions (10a&b) to be most appropriate for the 2, 5, and 10Å coverages and the linear functions (9a&b) to be best for the 20Å coverage.

Qualitative considerations of the 2 and 5Å polar profiles suggest that if Cu grows epitaxially with no indiffusion, the Cu($M_{2,3}VV$) intensity should be larger at shallow exit angles, by virtue of surface enhancement. However, the intensity is essentially constant from ~30° to 90° for both coverages. This effect could be brought about by a substantial increase in Cu density at the interface boundary relative to the surface, or by Cu diffusion into the substrate. Either phenomenon will bolster the

intensities at large polar angles. These two situations are predicted to occur with the use of Eqs. 9a&b and 10a&b, respectively. If the system is constrained to produce the observed polar profile without the aid of metal indiffusion, a large increase in Cu density at the interface relative to the surface must result. Equations 9a&b predict increases from .0542 and .0528 (at the surface) to .1342 and .1161 atoms/A^3 (at the interface) for 2A and 5A coverages, respectively. However, the weak 1x1 LEED patterns at 2 and 5A suggest that within the first few monolayers the Cu density should be close to that of Si (.0502 atoms/A^3). Moreover, given that the Si number density increases from surface to interface boundary, it is most likely that the Cu number density decreases or remains constant. Therefore, we judge Eqs. 9a&b to be physically untenable representations of the Cu density function. In contrast, Eqs. 10a&b predict for 2A a sharp decrease in Cu density from .101 at the surface to .0424 atoms/A^3 at the interface. Using Eqs. 10a&b for the 5A coverage, it was necessary to constrain a_1 to be negative and less than or equal to ρ_s/d in magnitude. Without this constraint, a_1 tended to be positive, as it was when Eqs. 9a&b were used. With the constraint, however, a_1 converages to zero, resulting in a constant Cu density of .0687 atoms/A^3 throughout the interfacial region. For both coverages, the extent of Cu indiffusion is predicted to be about the same; characteristic penetration depths of 1 to 2A result from the fits.

In principle, Eqs. 10a&b can be used for the 10A coverage as well. Since 95% of a given Auger signal originates within a depth of 3A (11A for the Cu($M_{2,3}VV$) electron), we can probe the interface boundary when d is ~10A or less. As in the 5A case, a_1 must be bracketed between zero and $-\rho_s/d$, lest it converge to a positive number. The result is a constant Cu density of .0817 atoms/A^3 within the overlayer and a characteristic penetration

depth of 1A in the substrate. The use of Eqs. 9a&b without constraints on a_1 results in an unreasonably large and positive value of a_1 (2.067×10^{-3}). Since we have no sensitivity to the interface boundary when d is 20A, we use Eqs. 9a&b to calculate Cu densities in the top 10 to 11 A of the overlayer. Here, we do not constrain a_1 and a slight Cu density increase is predicted from surface to interface boundary. Moreover, the Cu density converges to a value quite close to the bulk Cu value at the surface, in good agreement with the LEED results which showed the ordered Cu(111) pattern.

The overall results are best summarized by plotting the calculated Si and Cu atom number densities as a function of distance from the interface boundary, as shown in Fig. 8. One striking observation is that the Si surface density is an order of magnitude smaller and the Cu surface density is 20 to 30% larger at 2A than at higher coverages. This result indicates that Cu builds up on the surface prior to the strong Si-Cu interaction, the surface disruption, and the onset of Si outdiffusion. This interface therefore exhibits a reaction triggered by Cu coverage in excess of 2A but not at lower coverage. A second important observation is that for the 10 and 20A coverages, the total atom number density within the first few Angstroms of the interfacial region exceeds that of either pure Si or pure Cu but rapidly approaches the bulk Cu value with increasing distance from the interface boundary. This result suggests that the interface is an intermixed Cu-Si phase. with Cu being the predominant element and Si being dissolved in the matrix to a decreasing extent as the surface is approached.

V. DISCUSSION

A. Comparison with Other Techniques

Interdiffusion at metal-semiconductor interfaces has been qualitatively studied recently by both angle-resolved and angle-integrated photoemission[1,3-5,24,25]. While outdiffusion of Si is relatively easy to observe by constructing attenuation curves similar to those in Fig. 3, diffusion of the metal into the substrate has been observed by comparing the rate of growth of the metal photoemission intensity with coverage to that expected for a sharp interface[24] and by performing marker experiments.[25] In the latter, a thin layer of an inert metal is deposited onto the substrate prior to evaporation of the metal of interest. Assuming the marker layer does not interfere with interdiffusion, the behavior of the substrate to marker intensity ratio with coverage indicates qualitatively whether or not indiffusion of the metal is occurring. The advantages of the method described here is that no marker layer (which may indeed perturb the interdiffusion process[26]) is needed and the quantitative extent of indiffusion can be obtained.

Other quantative methods involving polar angle-resolved x-ray photoemission have been proposed recently. Specifically, Pijolet and Hollinger have attempted to extract density information directly from the polar profiles via a simplex method which minimizes the difference between theoretical and experimental intensity ratios.[27] However, this approach has proved to possess some serious difficulties. First, the extracted concentrations are extremely sensitive to the details of the polar profile. Intensity ratio changes on the order of 0.001% make substantial changes in the extracted concentrations. In order to remedy the situation, they found that it was necessary to introduce two physically reasonable contraints on

the concentrations. These consisted of: (1) bracketing the concentration of each specie between zero and the bulk concentration for the pure material and (2) assuming a particular shape or trend in the density profile. Clearly, once such constraints are introduced, the method becomes quite analogous to what we present here. However, this "direct extraction" method requires a number of involved numerical techniques which necessitate considerable computer time on a large mainframe computer. The method we introduce is relatively simple and can be run on any of the powerful microcomputers currently available.

B. The Chemical Nature of the Interface Region

The substantial lineshape changes in the Si($L_{2,3}VV$) peak clearly demonstrate that, upon interdiffusion, a strong electronic interaction occurs between Si and Cu. As the normal sp^3 hybrid bonds are broken in the Si lattice and outdiffusion occurs, the valence states are modified and new channels for Auger de-excitation are opened, thus modifying the Si($L_{2,3}VV$) spectrum.[22] Although the details of chemical environment are very difficult to extract from Auger lineshape analysis, the results presented here enable us to comment on the stoichiometry of the intermixed phase. Above a coverage of 2Å, the Cu density in the overlayer is constant. However, the Si density drops very rapidly from interface to surface for all coverages. These results suggest that a copper silicide of fixed stoichiometry does not form in the intermixed region, as proposed earlier.[4] Rather, a Cu lattice which is rich in Si only near the interface appears to be a better description (see Fig. 8). This conclusion is consistent with valence band photoemission results which show a dominant Cu-derived 3d feature that shifts from 3.5 eV below the Fermi level at submonolayer coverages to

~2.8 eV at 45 monolayers, indicative of a transition from isolated Cu atoms to a pure cu metallic phase.[3] Cu diffuses into the substrate with a characteristic penetration depth of 1-2A and, in all likelihood, occupies defect and interstitial sites. This description of the interface is consistent with the bulk Cu-Si phase diagram which shows ~2% solubility of Si in Cu at room temperature and no compound formation at room temperature and Si percent by weight less than ~8%.[28,29] The lack of solubility of Cu in Si, however, indicates that the slight indiffusion of Cu observed here is the result of microscopic localized phenomena.

Although similar agreement between interface interdiffusion results and bulk phase information has been noted by Brillson et al.[25] for Al/Si(111)-7x7, agreement for Au/Si(111)-7x7 is lacking. The former is a weakly interacting chemisorption system, consistent with phase data. The latter, however, strongly interacts with considerable intermixing at room temperature, despite the inertness predicted by the phase diagram. Thus, it appears that bulk thermodynamic data are not of universal utility in predicting interface phenomena for noble metals adsorbed on Si single crystals.

VI. CONCLUSIONS

Angle-resolved Auger electron emission has been shown to be a powerful technique for the study of interdiffusion at a metal-semiconductor interface. Detailed antitative information on the composition of the interfacial region can be extracted from the polar-angle intensity profiles by means of a relatively simple theoretical model. It has been shown that intermixing for Cu/Si(111)-7x7 leads to an interface which is constant in Cu density throughout but which exhibits a Si density that decreases

exponentially from interface boundary to surface. Furthermore, it has been demonstrated that the bulk phase diagram for the noble metal-semiconductor system is useful in predicting interdiffusion properties of the interface, although not universally so.

ACKNOWLEDGEMENTS

This work was supported by a Northwest Area Foundation Grant of Research Corporation (Chambers, Greenlee and Howell) and the Army Research Office, ARO-DAAG-29-83-K-0061 and ARO-DAAG29-84-K-0169 (Weaver). Stimulating discussions with Dr. M. Grioni are gratefully acknowledged.

REFERENCES

1. For an extensive review of metal/semiconductor interfaces, see L.J. Brillson, Surf. Sci. Rep. 2, 123 (1982).
2. M. Grioni, J. Joyce, S.A. Chambers, D.G. O'Neill, M. del Giudice, and J.H. Weaver, submitted to Phys. Rev. Lett.
3. F. Ringeisen, J. Derrien, E. Daugy, J.M. Layet, P. Mathiez, and F. Salvan, J. Vac. Sci. Technol. B1, 546 (1983).
4. G. Rossi, T. Kendelewicz, I. Lindau, and W.E. Spicer, J. Vac. Sci. Technol. A1, 987 (1983).
5. Thin Films - Interdiffusion and Reactions, J.M. Poate, K.N. Tu, and J.W. Mayer, eds., John Wiley and Sons, New York (1978).
6. J.W. Coburn, J. Vac. Sci. Technol. 13, 1037 (1976).
7. T. Ishitani and R. Shimizu, Appl. Phys. 6, 241 (1975).
8. H.H. Andersen, Appl. Phys. 18, 131 (1979).
9. P.S. Ho and J.E. Lewis, Surf. Sci. 55, 335 (1976).
10. J.M. Guglielmacci and M. Gillet, Surf. Sci. 94, 424 (1980).
11. N.J. Chou and M.W. Shafer, Surf. Sci. 92, 601 (1980).
12. C.S. Fadley and S.A.L. Bergstrom, Phys. Lett. 35A, 375 (1971).
13. C.S. Fadley in Electron Spectroscopy: Theory, Techniques, and Applications, C.R. Brundle and A.D. Baker, eds., Academic Press, London (1978), Vol. 2, Chap. 1.
14. N.G. Stoffel, M. Turowski, and G. Margaritondo, Phys. Rev. B 30, 3294 (1984).
15. C.S. Fadley in Progress in Solid State Chemistry, G.A. Somorjai and J.O. McCaldin, eds., Pergamon Press, New York (1976), Vol. 11, pp. 275-284.

16. S. Kono, S.M. Goldberg, N.F.T. Hall and C.S. Fadley, Phys. Rev. B 22, 6085 (1980).

17. J.E. Rowe and H. Ibach, Phys. Rev. Lett. 32, 421 (1974).

18. D.W. Marquardt, J. Soc. Ind. Appl. Math. 11, 431 (1963).

19. S.A. Chambers and L.W. Swanson, Surf. Sci. 131, 385 (1983).

20. J.M. McDavid and S.C. Fain, Surf. Sci. 52, 670 (1975).

21. R. Matz, R.J. Purtell, Y. Yokota, G.W. Rubloff, and P.S. Ho, J. Vac. Sci. Technol. A2, 253 (1984).

22. P.S. Ho, G.W. Rubloff, J.E. Lewis, V.L. Moruzzi, and A.R. Williams, Phys. Rev. B 22, 4784 (1980).

23. I. Lindau and W.E. Spicer, J. Elec. Spect. Rel. Phen. 3, 409 (1974).

24. L. Braicovich, C.M. Garner, P.R. Skeath, C.Y. Su, P.W. Chye, I. Lindau, and W.E. Spicer, Phys. Rev. B 20, 5131 (1979)

25. L.J. Brillson, A.D. Katnani, M. Kelly, and G. Margaritondo, J. Vac. Sci. Technol. A2, 551 (1984).

26. A Franciosi, J.H. Weaver, and D.G. O'Neill, Phys. Rev. B 28, 4889 (1983).

27. M. Pijolat and G. Hollinger, Surf. Sci. 105, 114 (1981).

28. M. Hansen, Constitution of Binary Alloys, 2nd Ed., McGraw-Hill, 1958.

29. R.P. Elliot, Constitution of Binary Alloys, First Supplement, McGraw-Hill, 1965.

TABLE 1

Model predictions for surface silicon number densities

$$\rho_{Si}(y) = \rho_0 \exp[-a(d-y)]$$

d (A)	a	surface atom number density (atoms/A^3)
2	2.51	3.34×10^{-4}
5	.602	2.47×10^{-3}
10	.282	3.00×10^{-3}
20	.143	2.85×10^{-3}

Table 2

Model predictions for Cu atom number densities

$$\rho_{Cu}(y) = \begin{cases} \rho_2 + a_1 y & \text{for } y<d \text{ at all coverages} \\ 0 & \text{for } y>d \text{ and } d=2,5 \text{ and } 10A \\ (\rho_s + a_1 d)\exp[-a_2(y-d)] & \text{for } y>d \text{ and } d=20A \end{cases}$$

d(A)	ρ_s (surface atom number density in atoms/A^3)	$a_1 (\times 10^2)$	a_2
2	.101	-2.93	.667
5	.0687	0	.452
10	.0817	0	.923
20	.0793	.0127	-

FIGURE CAPTIONS

Fig. 1 Orientation of the sample with respect to the incident electron beam and analyzer aperture.

Fig. 2 Si($L_{2,3}VV$) and Cu($M_{2,3}VV$) Auger spectra as a function of Cu coverage in A. 1A of Cu equals 1.1 monolayers on Si(111).

Fig. 3 Attenuation-growth curve for the unannealed Si-Cu interface. d is the overlayer thickness.

Fig. 4 Si($L_{2,3}VV$) polar intensity profile taken in two symmetry-inequivalent azimuthal planes perpendicular to the surface. No annealing.

Fig. 5 Cu($M_{2,3}VV$) polar intensity profile taken in two symmetry-inequivalent azimuthal planes perpendicular to the surface. No annealing.

Fig. 6a Clean surface Si($L_{2,3}VV$) polar profile averaged over two azimuthal planes, raw data and smoothed to remove diffraction-induced fine structure.

Fig. 6b Two-azimuth averaged experimental and calculated Si($L_{2,3}VV$) polar profiles using Eqs. 8a&b as a Si atom number density function.

Fig. 7a Cu($M_{2,3}VV$) polar profiles for a 60A Cu film (pure Cu(111)) averaged over two azimuthal planes, raw data and smoothed to remove diffraction-induced fine structure.

Fig. 7b Two-azimuth averaged experimental and calculated Cu($M_{2,3}VV$) polar profiles using Eqs. 10a&b for 2, 5 and 10 A coverages and Eqs. 9a and 9b for the 20 A coverage.

Fig. 8 Calculated Cu and Si atom number densities vs. distance from the interface boundary. A dashed line signifies an extrapolation, since our maximum depth sensitivity is 3λ (10 to 11 A).

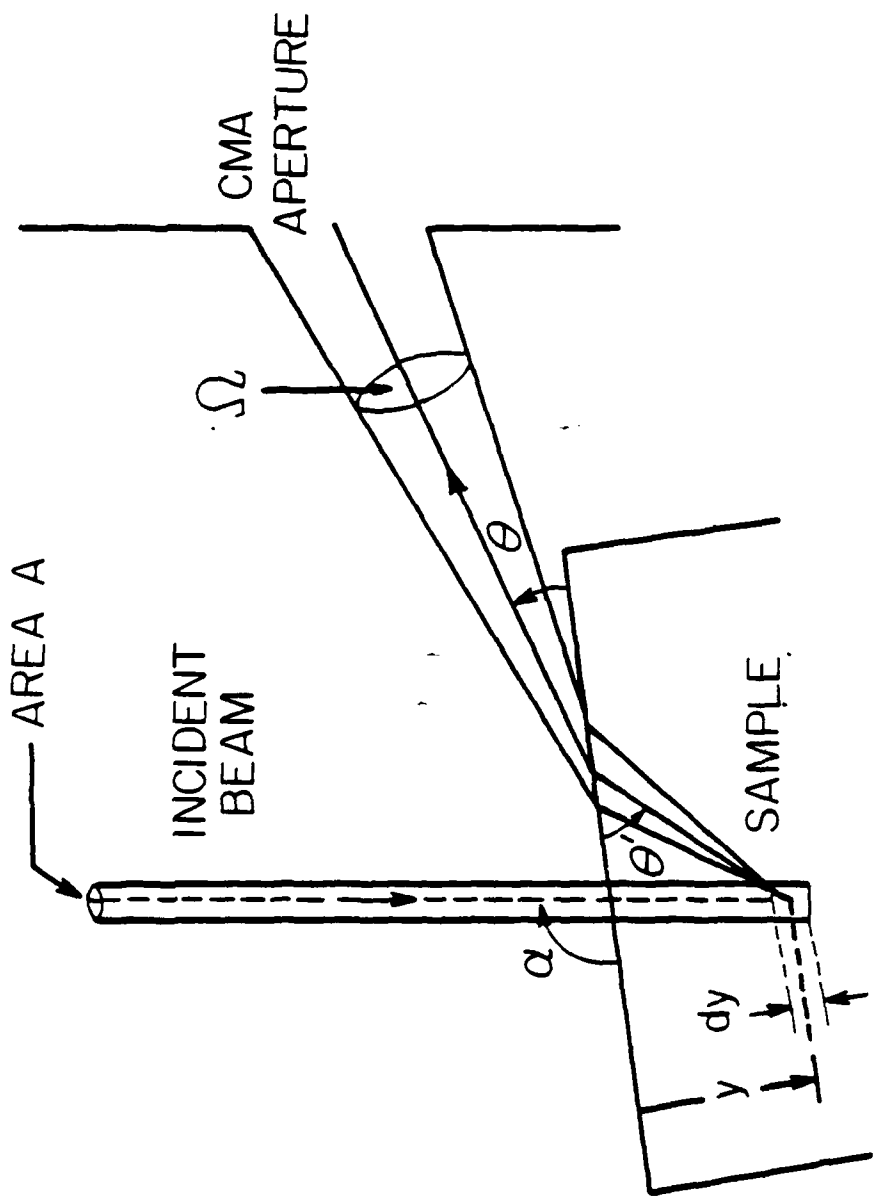

Fig. 1

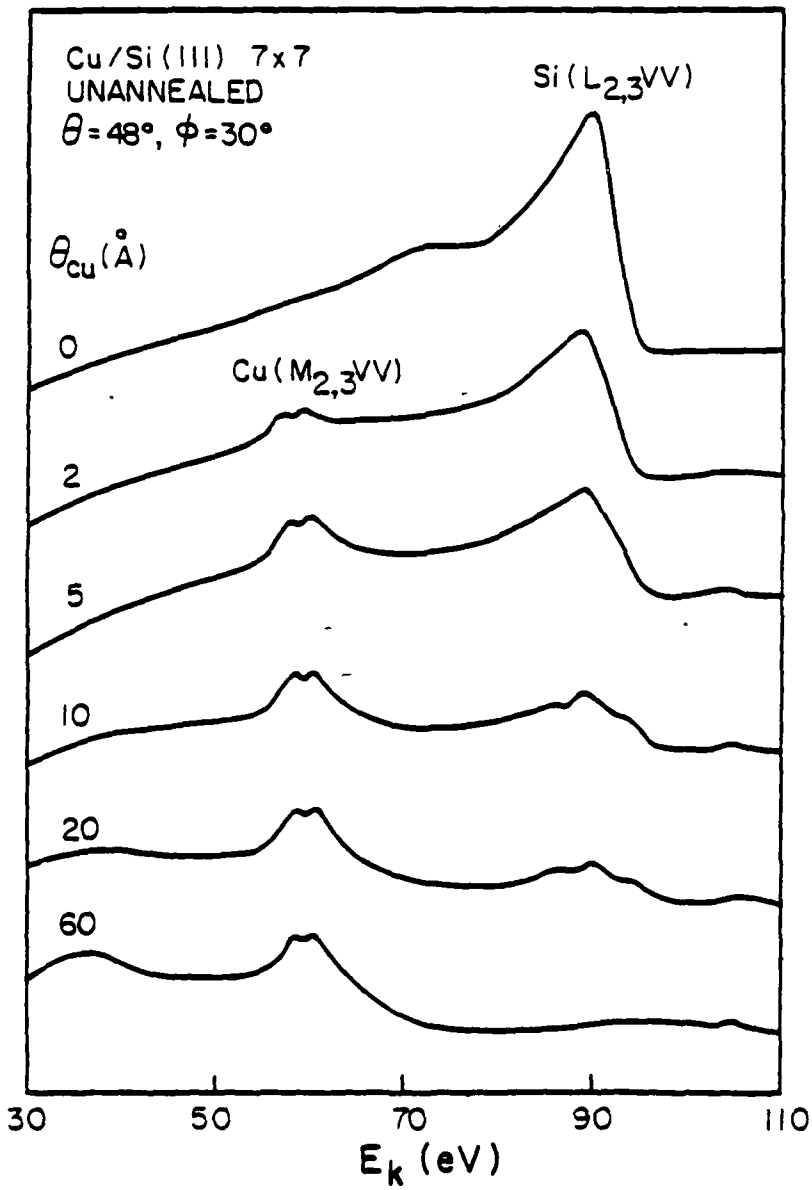
Cu/Si(111) 7x7
UNANNEALED
θ=48°, Φ=30°
Si(L2,3VV)
θCu(Å)
0
Cu(M2,3VV)
2
5
10
20
60
30
50
70
90
110
Ek (eV)

Fig. 2

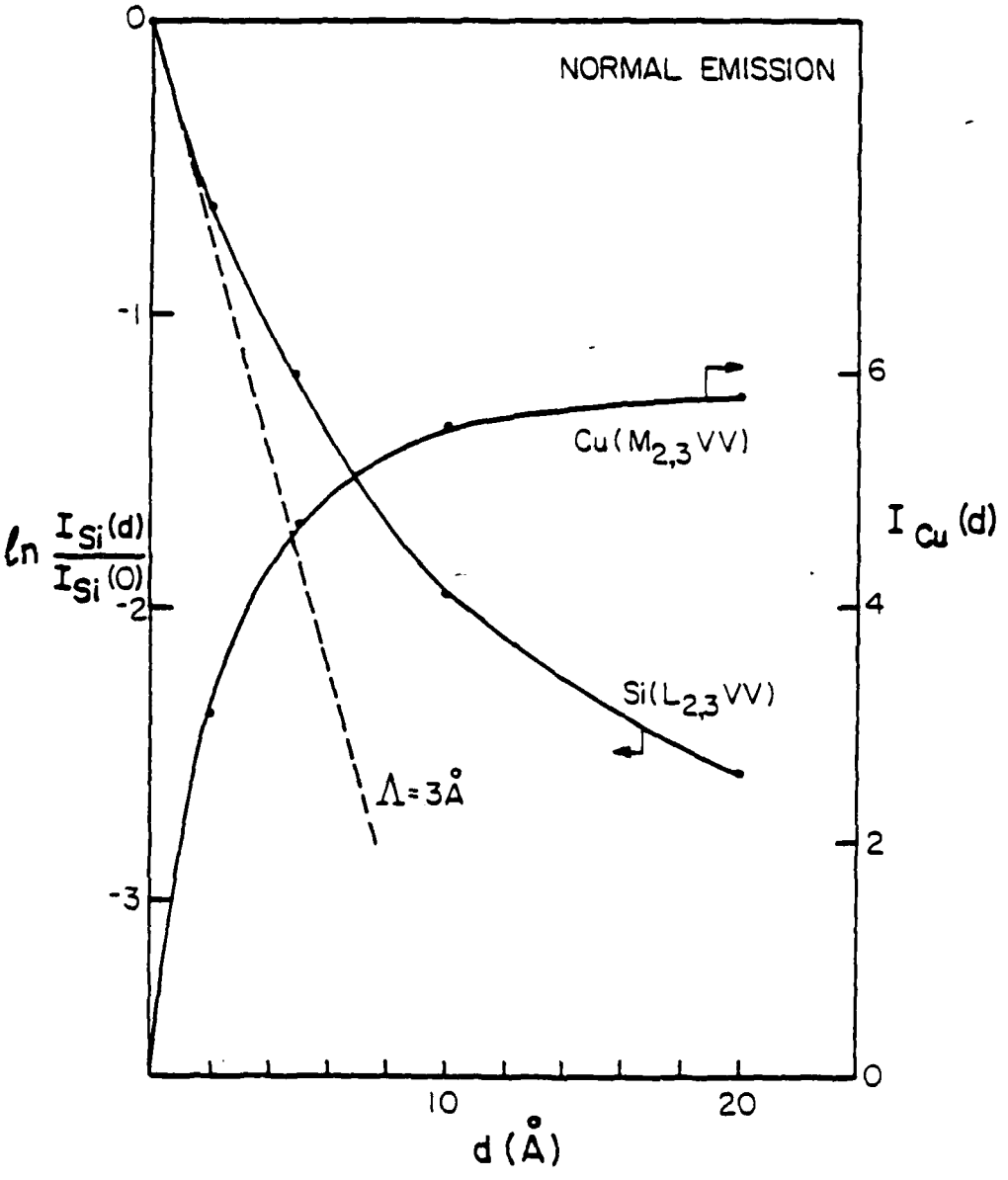
NORMAL EMISSION
Cu(M2,3VV)
Si(L2,3VV)
Λ=3Å
ln ISi(d)/ISi(0)
ICu(d)
d (Å)
0
-1
-2
-3
6
4
2
0
10
20

Fig. 3

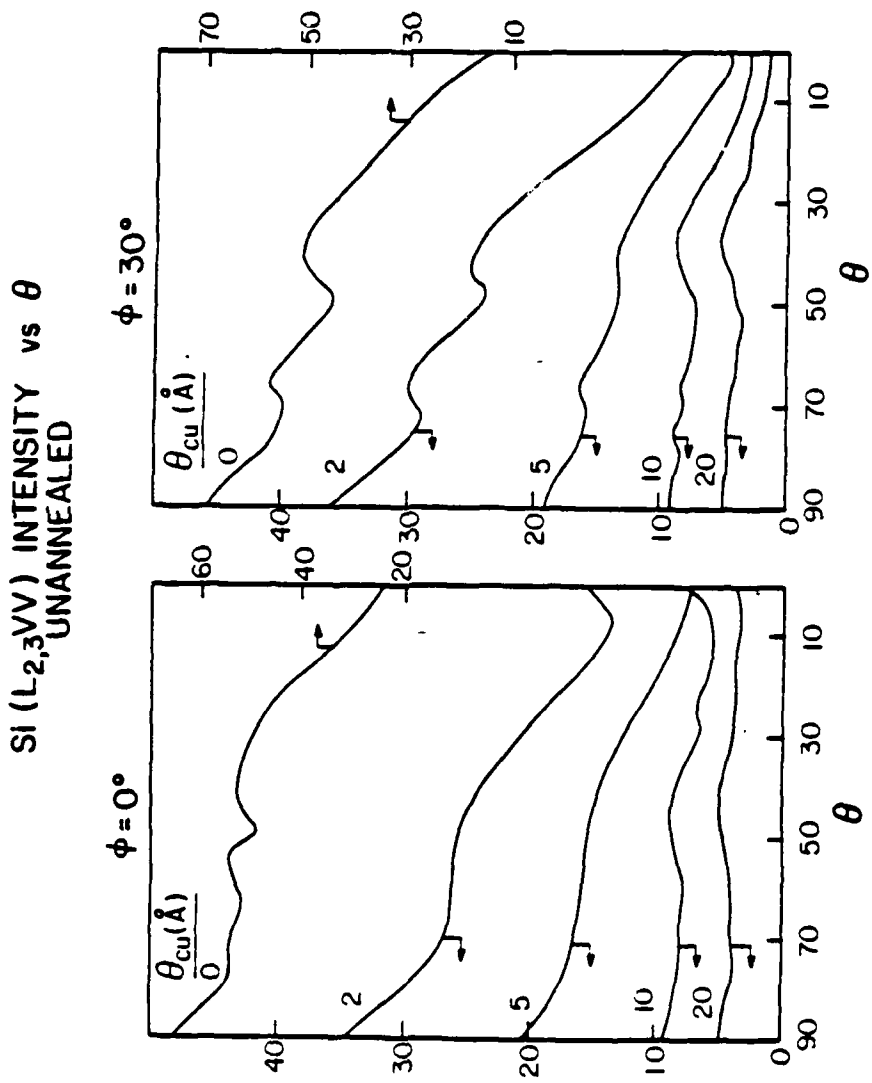
Si ($L_{2,3}VV$) INTENSITY vs θ
UNANNEALED
Φ = 0°
Φ = 30°
θ_{Cu} (Å)
0
2
5
10
20
θ

Fig. 4

AD-A150 075 STUDIES OFSSILICON-REFRACTORY METAL INTERFACES: 2/2
PHOTOEMISSION STUDY OF IN..(U) MINNESOTAUUIIV
MINNEPPOLIS DEPT OF CHEMICAL ENGINEERING AND M..
UNCLASSIFIED J H WEAVER 29 OCT 84 ARO-20577.5-PH F/G 11/2 NL

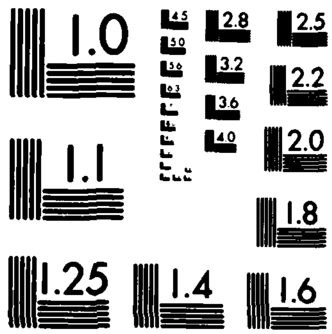

MICROCOPY RESOLUTION TEST CHART
NATIONAL BUREAU OF STANDARDS-1963-A

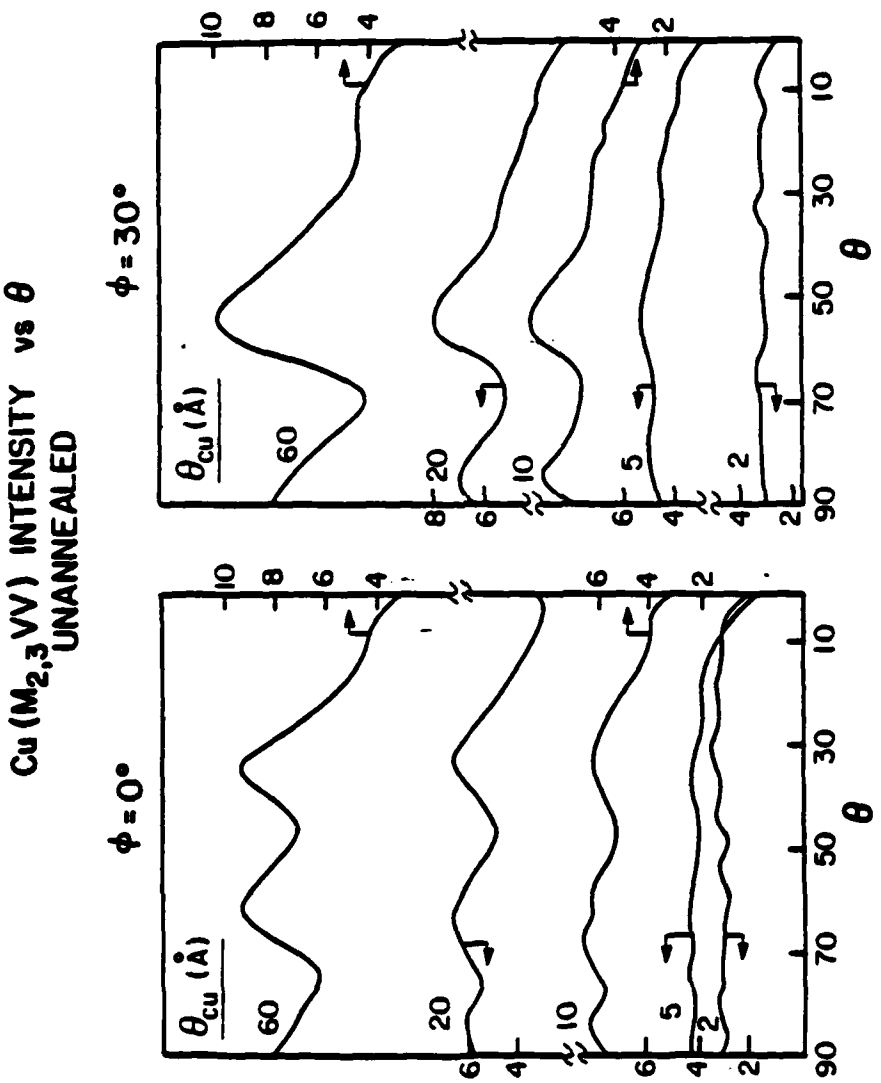
Cu ($M_{2,3}$VV) INTENSITY vs θ
UNANNEALED
φ = 0°
φ = 30°
θ
θ
θ_{Cu} (Å)
60
20
10
5
2

Fig. 5

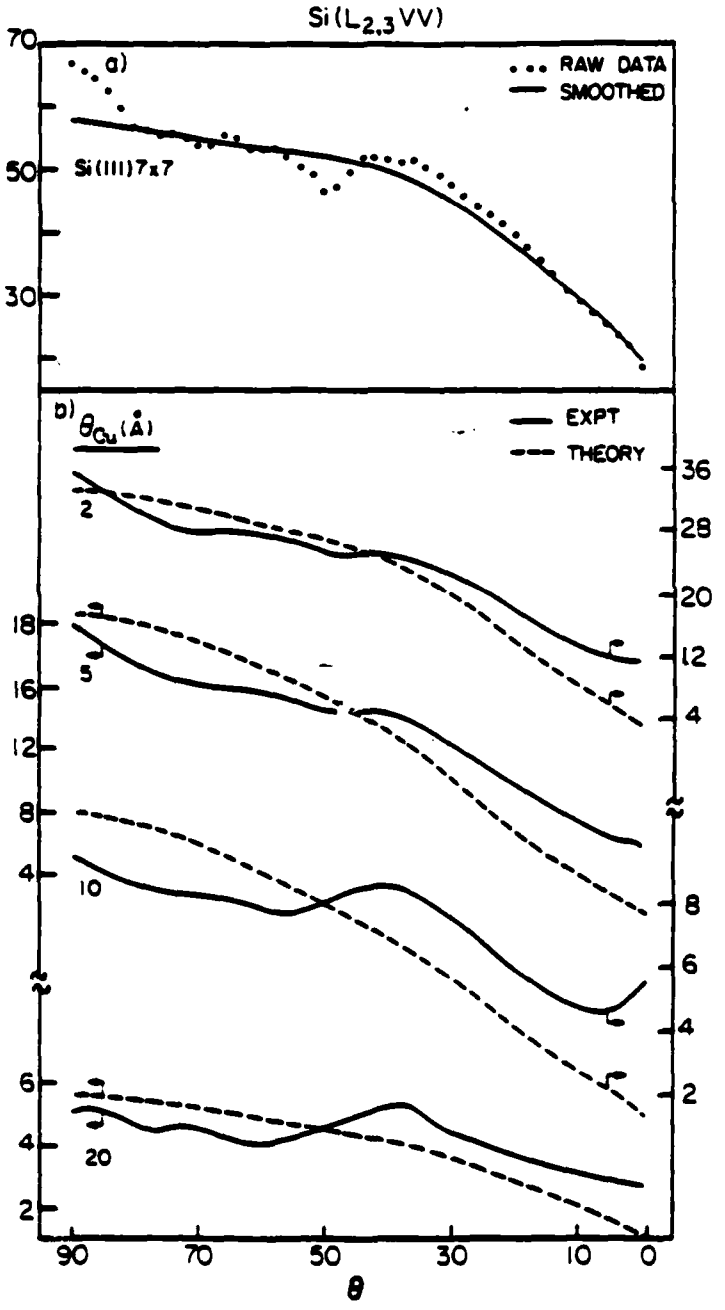
Si(L2,3VV)
a)
... RAW DATA
— SMOOTHED
Si(111)7x7
70
50
30
b) θCu(Å)
— EXPT
--- THEORY
2
5
10
20
36
28
20
12
4
18
16
12
8
4
8
6
4
2
6
4
2
90
70
50
30
10
0
θ

Fig. 6

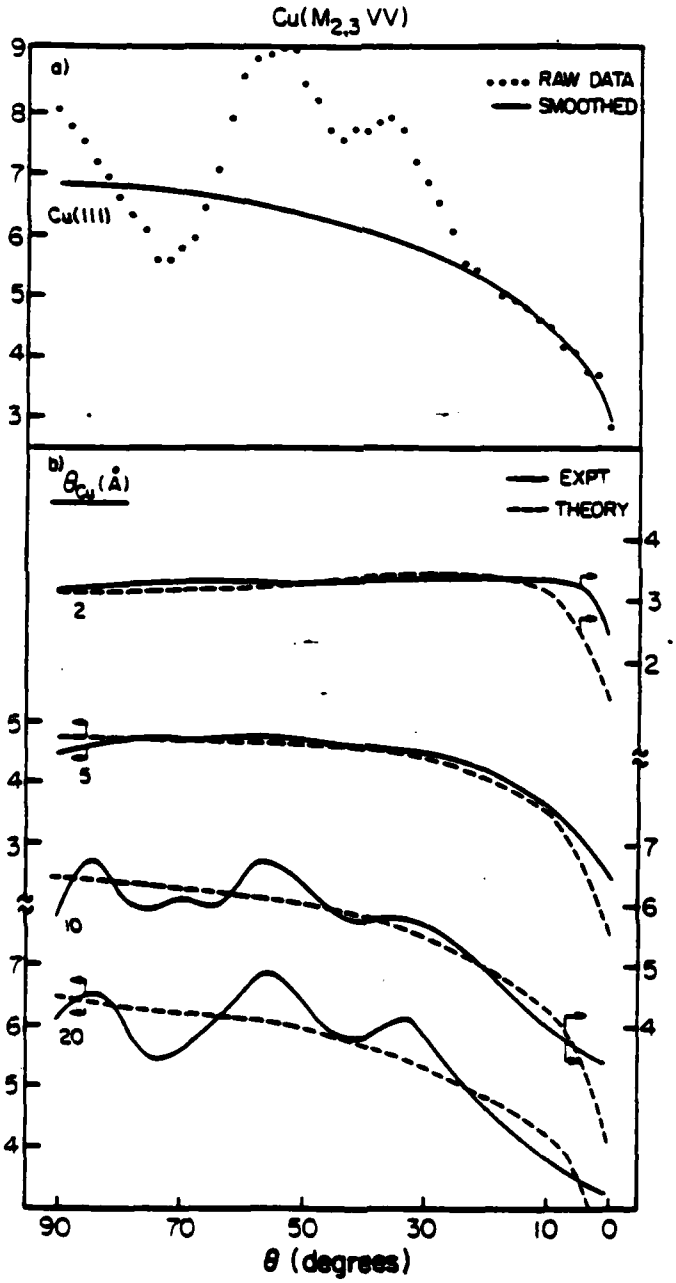
Cu($M_{2,3}$VV)
a)
.... RAW DATA
— SMOOTHED
Cu(111)
b)
θ_{Cu}(Å)
— EXPT
— THEORY
2
5
10
20
θ (degrees)

Fig. 7

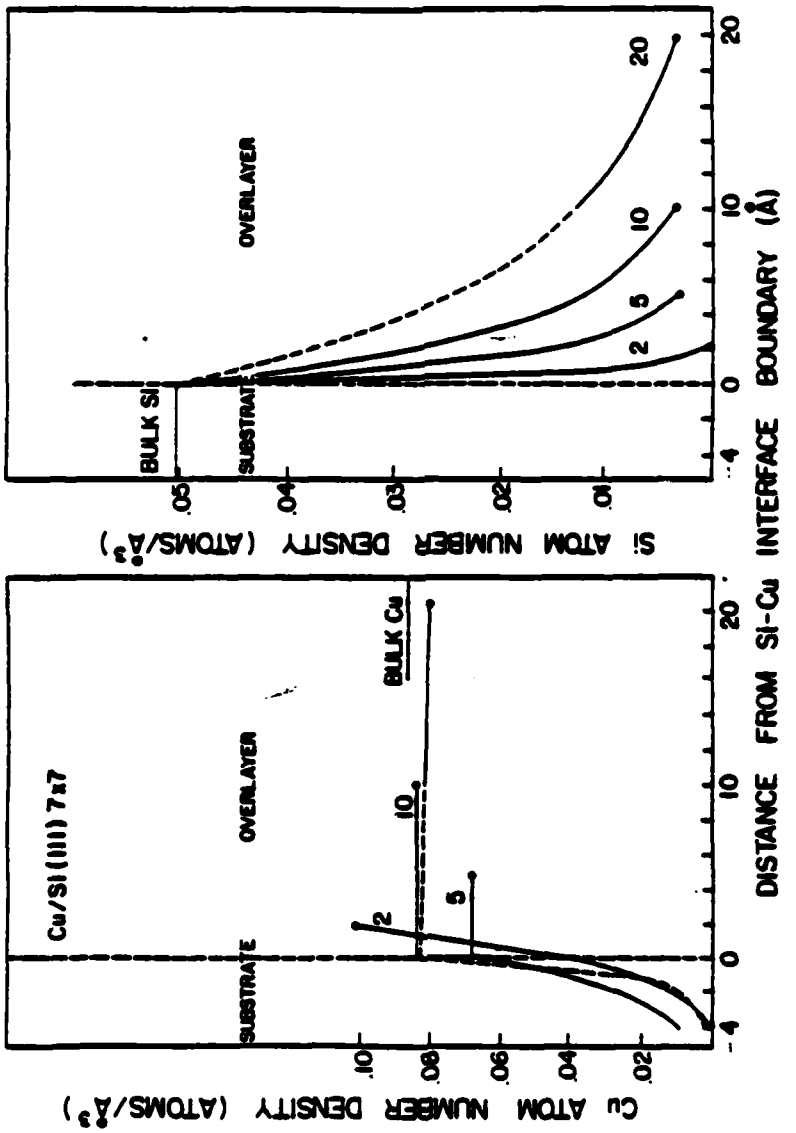
Si ATOM NUMBER DENSITY (ATOMS/Å³)
.05
.04
.03
.02
.01
BULK Si
SUBSTRATE
OVERLAYER
20
10
5
2
0
-4
10
20
DISTANCE FROM Si-Cu INTERFACE BOUNDARY (Å)
Cu ATOM NUMBER DENSITY (ATOMS/Å³)
.10
.08
.06
.04
.02
Cu/Si(111) 7x7
SUBSTRATE
OVERLAYER
BULK Cu
10
5
2
-4
0
10
20

Fig. 8

END

FILMED

3-85

DTIC